Exergy Methods for the Generic Analysis and Optimization of Hypersonic Vehicle Concepts

Kyle Charles Markell

Thesis submitted to the Faculty of the
Virginia Polytechnic Institute and State University
in partial fulfillments of the requirement for the degree of

Master of Science
In
Mechanical Engineering

Dr. Michael von Spakovsky, Chair
Dr. Walter O'Brien
Dr. Michael Ellis
Dr. David Moorhouse

February 7, 2005
Blacksburg, Virginia

Keywords: hypersonics, scramjet, exergy, optimization
Copyright 2005, Kyle Charles Markell

Exergy Methods for the Generic Analysis and Optimization of Hypersonic Vehicle Concepts.

by Kyle Charles Markell

Abstract

This thesis work presents detailed results of the application of exergy-based methods to highly dynamic, integrated aerospace systems such as hypersonic vehicle concepts. In particular, an exergy-based methodology is compared to a more traditional based measure by applying both to the synthesis/design and operational optimization of a hypersonic vehicle configuration comprised of an airframe sub-system and a propulsion sub-system consisting of inlet, combustor, and nozzle components. A number of key design and operational decision variables are identified as those which govern the hypersonic vehicle flow physics and thermodynamics and detailed one-dimensional models of each component and sub-system are developed. Rates of exergy loss as well as exergy destruction resulting from irreversible loss mechanisms are determined in each of the hypersonic vehicle sub-systems and their respective components.

Multiple optimizations are performed for both the propulsion sub-system only and for the entire hypersonic vehicle system for single mission segments and for a partial, three-segment mission. Three different objective functions are utilized in these optimizations with the specific goal of comparing exergy methods to a standard vehicle performance measure, namely, the vehicle overall efficiency. Results of these optimizations show that the exergy method presented here performs well when compared to the standard performance measure and, in a number of cases, leads to more optimal syntheses/designs in terms of the fuel mass flow rate required for a given task (e.g., for a fixed-thrust requirement or a given mission).

In addition to the various vehicle design optimizations, operational optimizations are conducted to examine the advantage if any of energy exchange to maintain shock-on-lip for both design and off-design conditions. Parametric studies of the hypersonic vehicle sub-systems and components are also conducted and provide further insights into the impacts that the design and operational decision variables and flow properties have on the rates of exergy destruction.

Acknowledgements

This thesis is the product of a great deal of hard work and dedication by many persons. I would first like to thank my advisor Dr. Michael von Spakovsky for giving me the opportunity to perform this research, for his faith in my abilities, and for his understanding of the decisions that were made regarding this thesis. Secondly, I would like to thank my partner in crime for the past year and a half, Keith Brewer. Keith's assistance and collaboration on model development and results generation was invaluable and genuinely appreciated.

Many thanks to Dr. Walter O'Brien, Dr. Michael Ellis, and Dr. David Moorhouse for serving on my committee, for any input they may have provided throughout the duration of this work, and for taking time to make draft corrections.

Special thanks to Dr. David Riggins at the University of Missouri-Rolla for his expertise in hypersonic propulsion and providing many valuable modeling suggestions. Dr. Riggins prompt responses to the plethora of emails and his willingness to help were greatly appreciated.

This work was conducted under the sponsorship of the U.S. Air Force Office of Scientific Research. I would like to thank Dr. David Moorhouse, Dr. Jose Camberos, and others at the Air Force Research Laboratory (AFRL) for their help and guidance on this project and for ultimately giving me experience through the summer research program at AFRL.

The MooLENI optimization software was provided by the Laboratory of Industrial Energy Systems (LENI) at Ecole Polytechnique Federale de Lausanne (EPFL) and for that I am grateful.

I would briefly like to show my appreciation for all my friends from home and to new friends made in Blacksburg. Even when times were tough, you all manage to keep things enjoyable and interesting (albeit sometimes too interesting!!). Many thanks to my girlfriend Lauren for her understanding and generosity and for keeping me focused on my work (and for those amazing colored drawings!!).

Finally, I would thank my parents for encouraging my decision to further my education, for their constant support, and of course let's not forget their financial support at times.

Kyle Charles Markell

Table of Contents

List of Figures

List of Tables

Nomenclature

A	Area, fit parameter	F	Force, streamthrust
B	Fit paramter	f_{st}	Stoichiometric fuel-to-air ratio
C_D	Drag coefficient	GHz	Gigahertz
C_L	Lift coefficient	g	Acceleration of gravity
C_p	Pressure coefficient	H, h	Height, enthalpy
C_m	Mixing constant	H_2	Hydrogen
C_f	Skin friction coefficient	H_2O	Water
CR	Contraction ratio	h_{pr}	Fuel lower heating value (LHV)
c_p	Constant pressure specific heat	I_{sp}	Specific impulse
c_v	Constant volume specific heat	ICR	Internal contraction ratio
$c.s.$	Control surface	L	Lift, length
D	Drag	L_m	Length for minor mixant to be depleted
D_h	Hydraulic diameter	M	Mach number
E	Energy	MHD	Magnetohydrodynamics
Ex, ex	Exergy	MB	Megabytes
$\dot{\boldsymbol{m}}$	Mass flow rate	S, s	Entropy, planform area

m	Mass	T	Thrust, static temperature
N_2	Nitrogen	t	Time, thickness
n	Load factor	U, u	Velocity
nm	Nautical miles	V	Velocity
$\dot{\boldsymbol{n}}$	Molar flow rate	$\forall$	Volume
O_2	Oxygen	W, w	Weight, work
P	Static pressure, power	X	Length, distance
Pr	Prandtl number	x_{cg}	Axial location of the center of gravity
Q , q	Heat	y_{cg}	Vertical location of the center of gravity
q_0	Dynamic pressure	y	Fuel-to-air axial velocity ratio, mole fraction
R	Specific gas constant, range	z	Elevation
RAM	Random Access Memory		
Re_x	Reynolds number		
r	Recovery factor		

Greek

α	Angle-of-attack	τ_{wall}	Wall shear force
β	Oblique shock angle	φ	Equivalence ratio
γ	Specific heat ratio	ψ	Inlet static temperature ratio
δ	Reference angle, differential amount	ω	Elevon deflection angle
ε	Reaction coordinate, thermo-dynamic effectiveness		
η_o	Overall efficiency	***Subsrcipts***	
η_{ee}	Engine effectiveness	*0*	Atmospheric conditions, freestream
η_{KE}	Kinetic energy efficiency	*1*	Inlet entrance
η_c	Compression efficiency	*4*	Inlet exit
η_p	Propulsive efficiency	*5*	Combustor entrance
η_{th}	Thermal efficiency	*6*	Combustor exit/nozzle entrance
θ	Deflection angle, flight angle	*7*	Nozzle exit
μ	Kinematic viscosity	*aero*	Aerodynamic
ν	Prandtl-Meyer function, stoichiometric coefficient	*aw*	Adiabatic wall
π_c	Total pressure ratio	*b*	Combustion
π_f	Fuel mass fraction	*c*	Cowl, chord
ρ	Density	*cowl*	Cowl lip

comb	Combustor
c.v.	Control volume
des	Destruction
elev	Elevon
fb	Forebody
f	Friction, fuel
fric	Friction
g	Gas
ht	Heat transfer
inc. comb.	Incomplete combustion
irr	Irreversibility
ic	Internal compression
M	Mixing
mix	Mixing, mixture
need	Required amount
nozz	Nozzle
opt	Optimal
p	Pressure
ramp1 (r1)	First inlet ramp
ramp2 (r2)	Second inlet ramp
s	Surface, shaft
surf	Surface
t	Total
vap	Vaporization
veh	Vehicle
w	wall

Superscripts

*	Reference conditions

Chapter 1

Introduction

The topic of and research in airbreathing propulsion via ramjet and scramjet engines is far from novel, dating back many decades[1]. These engines are attractive as propulsive devices because of their ability to sustain high speed atmospheric flight. Fluctuations in interest in and research on ramjet and scramjet engines have occurred over the past half century. However a rebirth of activity in recent year has occurred because the significant performance improvements promised by airbreathing propulsion have become attainable through the advancement of the underlying technologies. Therefore, this introductory chapter is dedicated to the explanation and importance of hypersonic flight and ramjet and scramjet engines as well as the presentation of some hypersonic flight milestones. This chapter also presents some of the design challenges associated with hypersonic vehicles and, finally, the objectives of this thesis are given.

1.1 General Background/History of Hypersonic Vehicles

It is important to understand what is really meant by the term *hypersonic* and what the significance of hypersonic flight truly is. A clear depiction of what a hypersonic vehicle may look like is essential to the comprehension of the material presented in this thesis and, therefore, a few hypersonic vehicle concepts are presented in this section. Furthermore, it is interesting to see and serves the purpose of describing the advancements and milestones in hypersonic flight in order to establish a mental picture progression of the field and possibly some of the lessons learned.

[1] In fact, the notion of using a ramjet engine as a propulsive device dates back to the early 1900's [1].

1.1.1 Hypersonic Flight – What is it? and Why is it important?

Hypersonic flow or flight is defined based on a conventional rule of thumb by flows where the Mach number is greater than 5 or 6. Unlike the progression from subsonic to supersonic flow, the acceleration of flow from supersonic to hypersonic velocities does not result in a 'thunderous clash'. Moreover, hypersonic flow is best defined as the regime where certain physical flow phenomena become progressively more important as the Mach number is increased to higher values [2]. Some of these flow phenomena may become more important at Mach numbers less than or greater than the aforementioned Mach numbers and, therefore, the definition of where the onset of hypersonic flow begins is truly an approximation.

One prominent phenomena of hypersonic flow is the occurrence of thin shock layers[2] over a body as predicted by oblique shock theory. Thin shock layers can create some physical complications, such as the merging of the shock wave itself with the boundary layer which in turn may lead to, for example, boundary layer separation. This phenomenon becomes increasingly important at low Reynolds numbers, i.e. high flight altitudes.

Another hypersonic flow phenomenon is that of an entropy layer which, for example, occurs in the region of a shock detachment point[3] and then continues to flow downstream and affect the boundary layer. The entropy layer is also a region of strong vorticity that tends to cause analytical problems when performing a standard boundary layer calculation on the surface [2].

A third phenomenon is attributed to viscous interaction which arises from the large boundary layer thicknesses needed to pass the required mass flow through the boundary layer at reduced density. Hypersonic boundary layers grow more rapidly than at slower speeds and, consequently, exert a major displacement effect on the inviscid flow outside the boundary layer, causing a given body shape to appear much thicker than it really is [2, 3]. Viscous interactions can have significant impacts of the surface pressure distribution which ultimately affect the lift, drag, and stability of the hypersonic vehicle [2]. Also, as already noted, the thick boundary layer can merge with the shock wave, resulting in complications with conventional boundary layer analysis.

[2] The shock layer is defined as the flowfield between the shock wave and the body.
[3] This is the region where the greatest entropy increase occurs across the shock wave.

The most significant aspect of hypersonic flow is the very high temperatures that can occur within the hypersonic boundary layers and in the nose region of blunt bodies. Extreme temperatures tend to cause dissociation of the gas molecules and possibly ionization within the gas and, therefore, the proper inclusion of chemically reacting effects is vital to the calculation of an accurate shock layer temperature [2, 3]. In some instances, temperatures as high as 10,000 K or more[4] occur in the shock layer or nose region of a hypersonic vehicle, especially during atmospheric reentry. Like viscous interaction, high temperature chemically reacting flows can have an influence on lift, drag, and moments on a hypersonic vehicle [2]. The most dominant aspect of high temperature hypersonic flows is the large convective heat transfer rates to the surface and possibly rather large radiative heating, both of which have a substantial influence on material selection.

A final characteristic of hypersonic aerodynamics is low-density flows that occur at extreme altitudes. Under these conditions, the aerodynamic concepts, equations, and results based on the assumption of a continuous medium (i.e. continuum) begin to break down and, consequently, methods from kinetic theory must be used to predict the aerodynamic behavior [2]. Additionally, an altitude can be reached where the conventional 'no-slip' condition begins to fail and the gas temperature at the surface of the vehicle does not equal the surface temperature of the material.

The development of aviation and aircraft has been continuously driven by the urge to fly faster and at higher elevations and attain greater flight ranges. To continue this trend, the development of hypersonic vehicles and the employment of ramjet and scramjet engines becomes ever more important. These vehicles and engines offer the potential to reduce the cost and increase the dependability of transporting payloads[5] to Earth orbits [1].

For example, consider the case of a rocket where, typically, greater than 60% of the takeoff weight is oxidizer (oxygen) and less than 5% of the takeoff weight is payload. This large fraction of oxygen reduces the weight fraction available for empty weight (including structures, propulsion, controls, etc.) which compromises ruggedness and flexibility [1]. If ramjet or scramjet engines are substituted for rockets, the oxidizer no longer needs to be carried along (i.e. these engines are air breathers) and is beneficial because

[4] These temperatures are about twice the surface temperature of the sun.
[5] In general terms, a payload could be a radar antenna, satellite, weapons for delivery, etc.

1. The takeoff weight fraction of the payload can be increased substantially.
2. The weight saved by leaving the oxygen behind could be used to make the vehicle (rocket) smaller while increasing the empty weight fraction and thereby improving the ruggedness and flexibility.
3. More fuel can be used to attain a greater range for payload delivery.
4. The reduced vehicle size and weight and the increased payload-to-takeoff weight ratio can help reduce payload delivery costs significantly.

Additionally, ramjet and scramjet offer the potential for higher sustainable velocities and ultimately faster delivery of the payload.

A few scramjet powered hypersonic vehicle concepts are depicted in Figure 1-1, including a strike/reconnaissance vehicle and space access vehicle. The strike/reconnaissance vehicle could be manned or unmanned and would have the ability to complete a mission much faster and more efficiently then presently possible. This concept of vehicle may be likened to the SR-71 Blackbird, which was a fairly high supersonic reconnaissance aircraft (attained flight speeds of Mach 3) that flew a few thousand successful missions without being shot down. The space vehicle concept is similar to that proposed by the United States National Aero-Space Program (NASP) which was a joint program between the Department of Defense and NASA. The goal of the NASP program was to develop and demonstrate the feasibility of a piloted, horizontal takeoff and landing aircraft that utilized conventional airfields, accelerated to hypersonic speeds, achieved orbit in a single stage, delivered useful payloads to space, returned to Earth with propulsive capability, and had the operability, flexibility, supportability, and economic potential of airplanes [1]. Another capability of hypersonic vehicles is hypersonic transport. These are contemporary ideas for hypersonic vehicles to cruise at Mach 7 to 12 and carry people from New York to Tokyo in less than two hours [2].

1.1.2 Advancements and Milestones in Hypersonic Flight

The notion of using ramjet engines as propulsive devices, as already mentioned, has been recognized since the early 1900s. However, it wasn't until 1946 when the first pure ramjet propulsion of a piloted aircraft took place; two ramjet engines were mounted on the wingtips of a Lockheed F-80. Then in 1949 the first piloted ramjet engine and airframe integrated aircraft, the Leduc 010, achieved successful ramjet propulsion and reached a Mach number of 0.84.

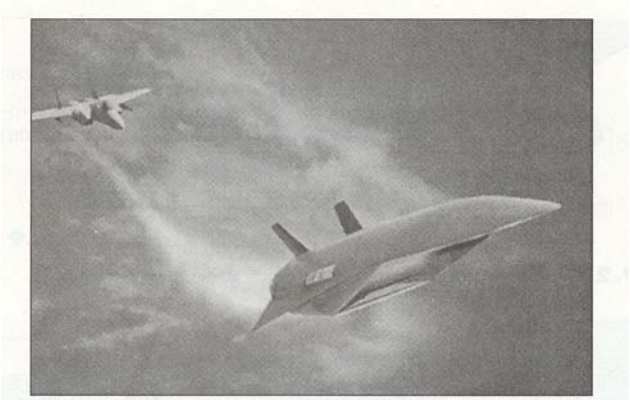

(*a*) Scramjet powered air-to-surface-missile concept

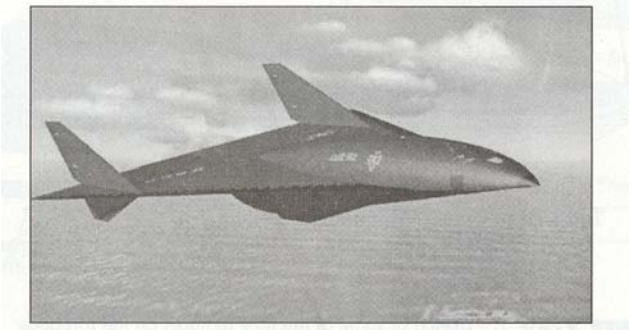

(*b*) Scramjet powered strike/reconnaissance vehicle concept

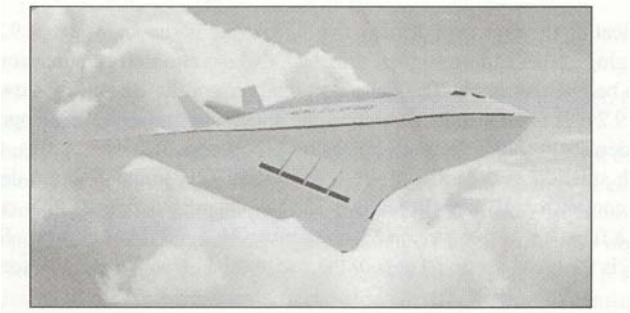

(*c*) Scramjet powered space access vehicle concept

Figure 1-1. Conceptual scramjet powered hypersonic vehicles (From Anderson Jr., J. D., *Fundamentals of Aerodynamics*, 3rd Edition, McGraw-Hill, New York, 2001 [3]; reprinted by permission of The McGraw-Hill Companies).

Shortly thereafter, the U.S. Air Force sponsored the Lockheed Aircraft Company X-7 and X-7A supersonic reusable pilotless flight research program. These vehicles were boosted by a solid rocket to ramjet takeover velocities and then propelled into sustained flight by ramjets. This program provided much significant ramjet performance information for Mach numbers up to approximately 4.3. Also during this timeframe, the use of ramjets for missile propulsion became

more attractive because of the ability to achieve greater range for the same propellant weight and because these systems were relatively simple with low initial costs. [1]

The first object of human origin to achieve hypersonic flight was that of a slender, needle-like rocket called the WAC Corporal. This rocket was mounted on the top of a V-2 rocket and served as a second stage to the V-2, ultimately detaching, igniting, and attaining a flight velocity of over 5000 mph. This was, of course, followed by the space age which began in 1961 when Russia's Flight Major Yuri Gagarin became the first human in history to experience hypersonic flight. Gagarin's orbital craft, the Vostok I, was launched into orbit, attained free flight around the earth and returned safely. Later that year Alan Shepard became the second man in space by virtue of a suborbital flight over the Atlantic Ocean where he entered the atmosphere at a speed above Mach 5.

The Hypersonic Research Engine (HRE) program was implemented by NASA in 1964 to develop scramjet engines. The goal of the HRE program was to test a complete, regeneratively cooled, flightweight scramjet engine on the X-15A-2 rocket research airplane. The X-15A-2 flew several times, achieving a maximum flight Mach number of 6.72 while having a dummy ramjet attached to its ventral fin. This program was ended prematurely though because of damage sustained to the rocket during its record breaking flight. In more recent times (early 1990s), the Russian Central Institute of Aviation Motors designed and launched a subscale, dual mode, ramjet and scramjet airbreathing engine mounted on the nose of a rocket for captive testing. This project not only sustained scramjet operation for 15 seconds, it also demonstrated ramjet to scramjet transition under realistic flight conditions. [1, 2]

The most recent demonstration of hypersonic flight and scramjet engines took place twice over the past year. Two successful flights of a subscale, unpiloted hypersonic vehicle, named the X-43A, demonstrated the capability of attaining high Mach number flight using air-breathing engines. The X-43A is a hypersonic aircraft developed under NASA's Hyper-X program. This program aimed to flight validate key propulsion and related technologies for air-breathing hypersonic aircraft and ultimately sought to expose the promise to increase payload capacities and reduce costs for future space and air travel. The latest flight brought to an end the eight year, $200 million plus program that incorporated three test flights. A depiction of the X-43A in flight in given in Figure 1-2 and the actual vehicle used in the test flights is shown in Figure 1-3.

Figure 1-2. Artist's rendition of the X-43A hypersonic experimental vehicle in flight. Photo taken from the website http://www.drfc.nasa.gov/Gallery/Photo/X-43A/HTML/index.html.

Figure 1-3. The actual X-43A hypersonic vehicle during ground testing. Photo taken from the website http://www.drfc.nasa.gov/Gallery/Photo/X-43A/HTML/index.html.

The X-43A is approximately 12 ft in length with a span of about 5 ft and is powered by a hydrogen fueled scramjet engine. For all test flights, the X-43A was mounted on the front of a booster rocket in which the rocket itself was mounted on a B-52B launch aircraft. The B-52B carried the rocket and X-43A to a given altitude and then launched the booster rocket. The booster rocket then took the X-43A to its desired test altitude and speed where at that point the X-43A separated from the rocket and flew for several minutes. The first test flight took place in June, 2001 but came to an abrupt end when the rocket and test vehicle had to be destroyed in mid-flight. The second test flight took place in March, 2004 where the X-43A was deployed at approximately 95,000 ft and successfully maintained a test flight Mach number of 7 under 10

seconds of scramjet engine operation. The final test flight occurred in November, 2004 where the X-43A separated from the rocket at around 110,000 ft. and cruised at Mach 9.6 (a little less than 7,000 mph) for 20 seconds of scramjet engine supplied power. The final test flight experienced approximately one-third hotter temperatures than the Mach 7 flight.

1.2 Hypersonic Vehicle Design Challenges

There are many design challenges associated with achieving hypersonic airbreathing propulsion because of the large range of flight operating conditions experienced and the highly integrated nature of the entire vehicle. Therefore, this section compares hypersonic vehicles with conventional high performance aircraft, describes hypersonic propulsion systems and their integration into the airframe, and also discusses the need for a common metric in hypersonic vehicle synthesis/design.

1.2.1 Hypersonic Vehicle versus Conventional Aircraft

Conventional subsonic and supersonic aircraft are designed such that the components for providing lift, propulsion, and volume (i.e. the wings, engines, and fuselage, respectively) are not strongly coupled to one another. The components are separate and distinct, i.e. each treated as a separate aerodynamic body and, when combined to form the entire aircraft, only interact moderately. Moreover, these components can be designed separately and still provide the necessary flight performance. The planform area of the wing supplies the lift necessary for flight and the engines contain rotating machinery to decelerate (compress) and accelerate (expand) the freestream flow. In addition, subsonic and supersonic aircraft operate over a fairly narrow flight Mach number range[6].

In contrast to conventional aircraft synthesis/design, the aerodynamic surfaces and the propulsive devices of a hypersonic vehicle are highly integrated. In fact, the entire undersurface of the vehicle serves as part of the scramjet engine. Compression of the freestream flow takes

[6] The statements made in this paragraph are completely consistent for the design of commercial and military transport aircraft but, to some point, are less applicable to advanced fighter aircraft design. Although advanced fighter aircraft have large, distinct wings for production of lift, they typically have portions of their engines integrated within the airframe which consequently results in some coupling of the components. However, advanced fighters are not nearly integrated to the degree of hypersonic vehicle configurations.

place on the front undersurface of the vehicle and is accomplished through a series of oblique shock waves generated as a result of flow deflection. Hydrogen fuel is burned in the supersonic combustor and is also used to cool vehicle surfaces. The combusted gases are expanded using the aft undersurface of the vehicle as an expansion nozzle. Most of the vehicle lift is produced by the high pressures on the compression and expansion surfaces and, therefore, large, distinct wings are not necessary for the production of lift. In addition, forces and moments change rather significantly in a nonlinear fashion with angle of attack. These are just a few reasons for the highly coupled aerodynamic and propulsion sub-systems of a hypersonic vehicle, i.e. changes to the propulsion sub-system inherently affect the vehicle aerodynamics. Furthermore, hypersonic vehicles are designed to traverse the atmosphere over rather large flight conditions (e.g., Mach 0 – 15) and, thus, need to be synthesized/designed to operate efficiently over these flight ranges. Hypersonic vehicles will ultimately incorporate both ramjet and scramjet propulsion in the vehicle, which adds further complexities to the synthesis/design. Finally, unlike conventional aircraft, hypersonic vehicles experience the various phenomena described in Section 1.1.1.

Capitalizing on vehicle surfaces for compression and expansion, as explained above, is essential to the success of the hypersonic vehicle synthesis/design. It was discovered in early hypersonic tests that making the hypersonic engines axisymmetric and attaching them to the vehicle using pylons or struts can produce enough external drag on the pylon and cowl to virtually cancel the internal thrust as well as producing internal flowfields that are difficult to manage [1].

1.2.2 Ramjet versus Scramjet Engines

Although ramjets can operate at subsonic flight speeds, they are predominately used for supersonic flight, specifically in the approximate Mach number range of 3 to 6. The freestream flow is compressed via a diffuser and is usually accomplished in several steps. The supersonic flow is initially decelerated by one or more oblique shock waves generated by the forebody of the vehicle or diffuser, further decelerated in a convergent duct, and then transformed into subsonic flow through a normal shock wave system. The subsonic flow may be further decelerated by a divergent duct to Mach numbers of about 0.2 to 0.3 where fuel is injected and burned in the combustor which typically contains a flameholder to stabilize the flame. The

burned gases are accelerated/expanded in a convergent-divergent nozzle and are exhausted into the atmosphere at supersonic speeds to provide the engine thrust.

At flight Mach numbers of about 6 and greater, the conversion of the freestream kinetic energy to internal energy via the compression system results in rather large combustor entrance pressures, temperatures, and densities. So pronounced is the effect that it is no longer advantageous to decelerate the flow to subsonic speeds. Adverse consequences can include pressures too high for practical burner structural design, excessive performance losses due to the normal shock system, excessive wall heat transfer rates, and combustion conditions that lose a large fraction of the available chemical energy to dissociation [1].

To avoid these problems, the flow is only partially compressed and decelerated using a supersonic combustion ramjet (i.e. scramjet) where the flow entering the combustor is supersonic. However, in contrast to ramjets, the scramjet engine diffuser takes greater advantage of the inevitable compression by the vehicle surface and the main compression mechanism is the oblique shock waves generated from the vehicle forebody and compression ramps. The diffuser is strictly convergent and, therefore, the flow entering the combustor is supersonic. Emphasis is placed upon mixing in the combustor because the supersonic flow throughout the combustor produces short available combustion times. Scramjet combustors will more than likely use hydrogen as fuel whereas ramjets typically burn some form of hydrocarbon fuel. The burned gases are then accelerated/expanded using only a divergent nozzle which tends to be the afterbody surface of the vehicle.

Note that, for both of these engines, it is convenient to use the outside surface of the vehicle as the boundary of the engine. In addition, both of these engines are capable of producing large amounts of thrust in their respective flight regimes. Unfortunately, both ramjet and scramjet engines are incapable of developing static thrust and, therefore, cannot accelerate a vehicle from a standing start.

1.2.3 The Need for a Unified Approach to Hypersonic Vehicle Synthesis/Design

Conventional aircraft systems and subsystems traditionally have been designed relying heavily on rules-of-thumb, individual experience, and rather simple, non-integrated trade-off analysis. There are methods for the synthesis/design of all the conventional aircraft systems and subsystems. However, they are highly dependent on the evolutionary nature of vehicle

development. In addition, there is a plethora of existing databases for all of the systems which can be used for synthesis/design.

As described in previous sections, hypersonic vehicles are extremely complex and highly integrated vehicles. These vehicles may contain many new subsystems and revolutionary concepts for which there is no existing database to support an evolutionary synthesis/design approach. As a result of the integrated nature of hypersonic vehicle subsystems, a simple trade-off analysis becomes virtually impossible. Many of the classical techniques are based upon simplifying assumptions that were implemented in the original derivation and, therefore, may not be applicable during the synthesis/design of these vehicles. In addition, traditional analysis techniques such as trajectory optimization or range performance may no longer produce an acceptable solution.

Therefore, the departure from existing databases and experience levels requires the need for a unified approach and common metrics in the synthesis/design of hypersonic vehicles with the ultimate hope of achieving an optimal synthesis/design. As stated by Moorhouse [4]:

> The need is for a methodology that can support the design of the complete vehicle as a system of systems in a common framework. All aspects in terms of common metrics must be considered in order to conduct credible trades. The vision is to develop such a methodology that will support all required levels of design activity in a natural fashion, from the conceptual comparisons through to the final configuration, and lead to a true system-level optimized design.

In other words, the lack of a common metric renders it quite difficult to make comparisons and trades between vehicle subsystems (i.e. components) and various vehicle syntheses/designs while searching for the optimal solution.

1.3 Thesis Objectives

The reasons for a unified approach to hypersonic vehicle design have already been presented and therefore a common metric is now required. Moorhouse et al. [4-6], Cambersos et al. [7, 8], Riggins et al. [9-13], Roth et al. [14, 15], Figliola et al. [16, 17], Paulus and Gaggioli [18], Bejan [19, 20], Curran et al. [21, 22], and Czyz [23] have proposed that the second law of

thermodynamics and exergy-based[7] methods will allow more complete system integration and facilitate the connection of all traditional results into a synthesis/design framework with a common metric. Therefore, the work conducted over the past year and a half at Virginia Tech and the Air Force Research Laboratory under the sponsorship of the AFOSR has aimed at extending those ideas and applying them to the conceptual design of a hypersonic vehicle configuration.

The specific goal of the work proposed for this thesis research is model with sufficient detail a hypersonic vehicle and demonstrate the use of exergy-based methods[8] in obtaining optimal synthesis configurations and designs (geometries). The major objectives envisioned for this thesis are as follows:

- Gain a fundamental understanding of how a hypersonic vehicle system and its sub-systems operate and a thorough comprehension of the fundamental phenomena present in each individual sub-system.
- Determine the key geometric parameters that drive the flow physics/thermodynamics and the various component performances and in turn use these parameters as the design decision variables.
- Create sufficiently accurate and detailed physical, thermodynamic, and aerodynamic models for the components and sub-systems of interest and describe their connectivities.
- Determine the irreversible loss mechanisms in each component and develop accurate methods to calculate the entropy generated or exergy destroyed from each loss mechanism.
- Define and choose the desired hypersonic vehicle performance measures.
- Define and use an optimization tool coupled with the component models to find the set of decision variables that optimizes a set of desired objection functions.
- Document and analyze the results for the various optimizations and other analyses of the hypersonic vehicle system.

It is apparent from the objectives stated above that a great deal of time and effort is to be put forth in developing realistic, sufficiently accurate component models that sufficiently describe

[7] Exergy is defined as the largest amount of energy that can be transferred from a system to a weight in a weight process while bringing the system to mutual stable equilibrium with a notional reservoir [24]. Also note that in the literature the terms "availabililty" [25] and "available energy" [24] are used synonymously with "exergy". This is true up to a point but the more general of these concepts is the "available energy" of Gyftopoulos and Beretta [24] which includes the other two as special cases.

[8] Although the term "2nd Law methods" is often used in the literature to be synonymous with "exergy methods", this is imprecise because "exergy" is in fact a concept which embodies both the 2nd and 1st Laws of thermodynamics (e.g., see [24]).

the flow characteristics and irreversibilites throughout the vehicle. It is imperative to do so because: (a) there are no analytical tools available to perform the calculations and analysis needed for this thesis work and (b) it is assumed simplistic component models may provide inaccurate information and ultimately lead to erroneous optimal synthesis/design conclusions. Additionally, to achieve the aforementioned objectives some sort of mission will need to be defined for the hypersonic vehicle.

Chapter 2

Literature Review

Many documents and papers have been examined which pertain to the topic of this research to provide a background in hypersonic vehicles and scramjet engines, to assist in the development of the analytical system and sub-system models, and allow means of comparison and validation of the models and performance measurements. However, the main focus of this work pertains to optimization and exergy methods for synthesis/design[9] of hypersonic vehicles and, therefore, this chapter is dedicated to the presentation of work in these and closely related areas.

2.1 Synthesis/Design Analysis and Optimization of High Performance Aircraft

Although high performance aircraft and their analysis have been present for quite sometime, the use of optimization methodologies in the synthesis/design of these systems appears to be fairly modern, most likely driven by the increase in computational power. In fact, only a sparse amount of literature was discovered on the topic of total vehicle synthesis/design using optimization. Therefore, the discussion in this section will provide a sufficient description of the strategies undertaken by others, models they have employed, and the results of their analyses and optimizations.

2.1.1 Subsonic/Supersonic Advanced Fighter Concepts

The synthesis/design of advanced fighter aircraft has been accomplished, for quite some time, by conventional methods such as rules-of-thumb, individual experience, and fairly non-

[9] Note that *synthesis* refers to changes in system configuration while *design* here refers exclusively to, for example, the nominal (full load or design point) capacity, performance, and geometry of a given component or technology.

integrated, simple trade-off analysis. However, the need for more complex, efficient, and cost effective aircraft systems calls for a more integrated, interdisciplinary approach to the synthesis/design analysis and optimization of these systems.

This integrated, interdisciplinary approach to synthesis/design was accomplished by Rancruel [26] and Rancruel and von Spakovsky [27-29] via a large scale decomposition methodology for the synthesis/design and operation which ensures the demands made by all sub-systems are accommodated in a way which results in the "optimal"[10] vehicle system for a given set of constraints (e.g. a mission, an environment, etc.). The decomposition methodology is based on the concept of "thermoeconomic isolation" [27, 30]; and conceptual, time, and physical decomposition were used to solve the system-level as well as unit-level sub-system optimization problems.

The main objective of Rancruel's and von Spakovsky's work was to demonstrate the feasibility of using a physical decomposition approach called Iterative Local-Global Optimization (ILGO) for the preliminary synthesis/design optimization of an Advanced Tactical Fighter Aircraft. ILGO is a decomposition strategy developed by Muñoz and von Spakovsky [31-33] in which highly coupled, highly dynamic energy systems are decomposed to arrive at the solution of the overall synthesis/design optimization problem and sub-system integration is facilitated. The Advanced Tactical Fighter Aircraft was decomposed into six sub-systems, namely, a propulsion sub-system, a fuel-loop sub-system, a vapor compressoion and PAO loops sub-system, an environmental control sub-system, an airframe[11] sub-system, and a permanent/expendable payload and equipment group sub-system. Of these, only the first five sub-systems were allowed optimization degrees of freedom totaling almost 500. The vehicle optimization defined was dynamic and highly non-linear with a mix of discrete and continuous decision variables. ILGO was employed for dynamically optimizing in an integrated fashion consistent with the optimum for the vehicle as a whole each of the sub-systems' syntheses/designs while taking into account the optimal behavior of each sub-system at off-design.

[10] The term "optimal" is used here in an engineering and not a strictly mathematical sense even though mathematical optimization and decomposition are used in the synthesis/design process. Improved synthesis/designs and not establishing whether or not the Kuhn-Tucker conditions for global optimality have been met is the focus of this type of methodological approach.

[11] Note that the airframe sub-system is a non-energy based sub-system.

Another objective was to gain a fundamental understanding of how a high performance aircraft system and its sub-systems operate and in the process as create physical, thermodynamic, and aerodynamic models of the components, sub-systems, and couplings between sub-systems involved. These models and computational tools were then used to optimize the system locally (i.e. at the component and sub-system levels) and globally (i.e. at the system level). Finally, an attempt was made to gain some insights into the usefulness of 1st and 2nd Law quantities for optimization purposes.

In the actual application given in this reference, the fighter aircraft system's synthesis/design was optimized over an entire flight mission consisting of fourteen separate mission segments such as take-off, subsonic cruise/climb, loiter, combat, supersonic cruise/climb, etc. The mission profile and the requirements/constraints of the mission segments were based upon the Request for Proposal for an Air-to-Air Fighter (AAF) given by Mattingly, Heiser, and Daley [34]. The airframe sub-system was based upon techniques and data provided by Raymer [35] and Mattingly, Heiser, and Daley [34]. The airframe sub-system supplied the lift over the entire mission while the propulsion sub-system modeled using an industry engine deck provided the necessary vehicle thrust as well as power and mass flow to the remaining sub-systems.

ILGO was then used to decompose and optimize the various sub-systems and overall system to arrive at a minimum fighter aircraft weight at take-off (gross take-off weight). Minimization of the thrust-to-weight ratio at take-off inherently led to the minimum gross take-off weight. The "global optimum" value for the gross take-off weight of the aircraft system was reached in seven iterations of ILGO. In the analysis, the final gross take-off weight was reduced by roughly 28% from the first iteration of the ILGO process. In the work done by Mattingly, Heiser, and Daley [34], a "best" gross take-off weight for the AAF in which only the engine design was "optimized" was determined to be 23,800 lb. The work on the whole vehicle done by Rancruel and von Spakovsky led to an optimum gross take-off weight of 22,396 lb, i.e. a 1404 lb (5.9%) lighter aircraft. Rancruel and von Spakovsky attribute this result to the integrated optimization of the aerodynamics, engine, and other sub-systems. The optimum solution also had an 11% lighter weight of fuel and 6.7% lower thrust-to-weight ratio at take-off in comparison with the work done by Mattingly et al.

2.1.2 Hypersonic Vehicle Concepts

A marginal amount of literature was discovered on the topic of the optimization of hypersonic vehicles. One such paper was written by Bowcutt [36] in which the optimization of the aeropropulsive performance of a hypersonic cruise and accelerator vehicle was developed. The hypersonic vehicle optimization approach used in the paper was based on four key elements:

1. Define a baseline configuration (see Figure 2-1).
2. Determine the fundamental geometric parameters of the baseline that drive the physics and component performance.
3. Develop parametric performance models or analysis tools for all vehicle components of interest.
4. Use an optimization tool to find the set of geometric parameters that maximizes or minimizes a desired objective function.

Bowcutt first defined a baseline configuration and selected the geometric parameters that were believed to govern the aerodynamic and propulsion physics of the simple baseline configuration. The baseline geometry was then parameterized so that the shape, size, and orientation of components could be altered in search of an arrangement that optimizes a parameter of interest (i.e. objective function). A hypersonic configuration of rectangular planform with a bottom integrated scramjet engine was chosen as the baseline. Five independent variables and three dependent variables were chosen for the analysis. The independent variables were the axial location of the cowl lip (X_{cowl}), the forebody compression angle (δ_{fb}), the isentropic compression ramp angle (δ_{ramp}), the engine cant angle (δ_{cowl}), and the nozzle chordal angle (δ_{nozz})(see Figure 2-1). The dependent variables, required to meet constraints, were the upper body bump height (h_u), wing size, and elevon deflection angle (δ_{elev}) (see Figure 2-1).

Bowcutt imposed a few important constraints on both the cruise and the acceleration vehicle. One constraint was to keep body volume constant for all perturbed geometries. This was accomplished by positioning of the upper body bump height. Pitching moments were trimmed to zero using the elevon and lift was required to equal the weight for all flight conditions. Finally, the cruise vehicle required an equal balance of thrust and drag.

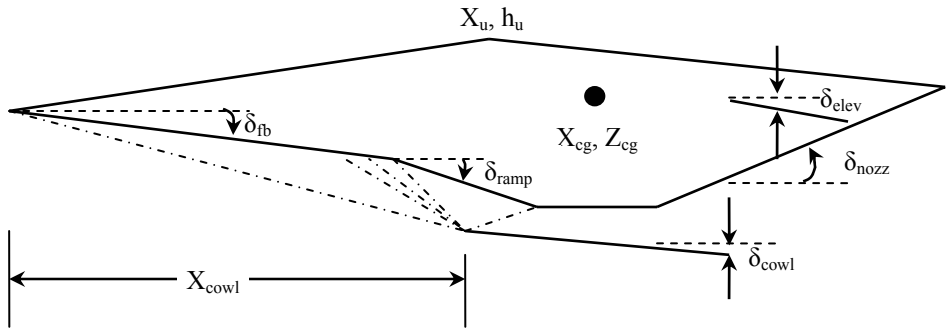

Figure 2-1. Representation of baseline configuration defined by Bowcutt [36]. Configuration shows independent and dependent variables.

Component performance models for the inlet, combustor, nozzle, and external aerodynamics (wing and fuselage) were developed[12]. All models ignored the effects of skin friction and heat transfer on vehicle performance and operability. The inlet was designed as a two-shock-plus isentropic ramp, mixed external and internal compression system (see, e.g. Figure 3-14). The shock-on-lip condition is maintained to ensure full mass capture, and uniform flow is delivered to the combustor. The combustor is modeled using the one-dimensional conservation equations (e.g., see Equations (3.5) – (3.7)), and it is assumed that hydrogen, oxygen, nitrogen, and water are the only chemical species, i.e. dissociation and chemical equilibrium are ignored. Hydrogen fuel is injected parallel to the combustor walls at specified conditions, the equivalence ratio is set to one except for cruise, and the combustor length is always set to fifteen times the inlet throat height. The nozzle is designed via ideal nozzle expansion analysis and the nozzle portion of the cowl is 15% of the total nozzle length. External aerodynamics (including wing, elevon) are analyzed using shock-expansion theory[13] for lift, drag, and moment coefficient predictions.

Bowcutt chose to use a non-liner simplex method[14] for function minimization developed by Nelder and Mead [37]. Optimizations were performed for both the acceleration and cruise vehicles at Mach 15 conditions. Effective specific impulse was selected as the objective function for the accelerator because maximizing this function will minimize the fuel fraction required to accelerate to a desired velocity. Therefore, the accelerator design problem was described as

[12] These main components of a hypersonic vehicle are described in some detail in Section 3.3 and may need to be referenced for assistance on the topics discussed in this chapter.

[13] Oblique shock and Prandtl-Meyer expansion theories are thoroughly presented in Section 3.2.

[14] This method is used extensively in hypersonic aerodynamics. It only requires an ability to numerically evaluate the function to be optimized and it handles a relatively large number of independent variables efficiently.

$$\text{Maximize } f(\vec{x}) = I_{sp_{eff}} = (T - D)/g\dot{m}_f \tag{2.1}$$

w.r.t $\vec{x}$

subject to a set of constraints and where $\vec{x}$ is the vector of independent decision variables, T is the trust, D is the drag, and $\dot{m}_f$ is the flow rate of fuel. Aircraft range was maximized for the cruise vehicle so that the cruise vehicle design optimization problem was given by

$$\text{Maximize } f(\vec{x}) = (L/D)I_{sp} \tag{2.2}$$

w.r.t $\vec{x}$

subject to a set of constraints and where L is the Lift. Optimizations were performed for each independent variable separately, and then the optimized variables were combined to observe how they interact.

The optimizations performed by Bowcutt led to an accelerator with an 89% increase in $I_{sp_{eff}}$ relative to the baseline and an elimination of the fixed wing. The optimum accelerator also had an engine further aft, a greater isentropic ramp angle to increase inlet compression, and an increased nozzle angle to increase thrust. Upper body height was also lowered to reduce drag. The optimum cruise vehicle had a similar geometry to the accelerator, except that there was a stronger emphasis on drag reduction and the engine was not as far aft. Also, a very low equivalence ratio less than one was needed to balance thrust and drag[15]. Finally, the separately optimized decision variables were combined to define the vehicle geometry, resulting in a 5% reduction in vehicle performance compared to the baseline. Therefore, the individually optimized parameters interact, or couple, negatively.

In more recent work, Bowcutt [38] presented a multidisciplinary design optimization (MDO) approach to the geometric optimization of a hypersonic cruise missile to maximize overall mission range [8]. The optimization was performed by varying the vehicle geometric variables by means of a numerical algorithm to maximize performance (i.e. range) for a fixed vehicle gross weight, length, height, and width. The specified flight trajectory accounted for both airbreathing acceleration and cruise, and trajectory analysis was conducted by first-order integration of the equations of motion and fuel flow rate between discrete Mach number and

[15] Bowcutt attributed this to the relatively small flow losses predicted by the simple models.

altitude points. The numerical algorithm used was once again that of the non-linear simplex method.

Five independent decision geometric variables were selected for their ability to influence longitudinal trim. Specifically, they were nose angle, engine axial location, engine cant angle[16], chine[17] length, and nozzle cowl length. These geometric variables were constrained to be within physically reasonable bounds. Constraints imposed on the vehicle were trim of lift and pitching moments during the acceleration phase and for cruise, trimmed lift and pitching moments and equal thrust and drag. Angle of attack, tail-deflection angle, and throttle setting were adjusted to effect trim.

An aerodynamic model, propulsion model, stability and control model, and mass property model were included in the analysis. In the aerodynamic model, surface forces were predicted using oblique shock and Prandtl-Meyer expansion theories and viscous drag was estimated from computed vehicle wetted area and a table of average skin-friction coefficients versus Mach number and altitude. The Hypersonic Arbitrary Body Program (HABP) [39] was used to evaluate the tail force and moment contributions and generate tabulated data which was added to the aerodynamic model. The propulsion system was based upon hydrocarbon scramjet technology developed under the Hypersonic Scramjet Engine Technology (HySET) [40] program. Three separate fluid dynamics codes were incorporated to determine performance. A two-dimensional Parabolized Navier-Stokes solver was used for the inlet analysis along with a two-dimensional method of characteristics flow solver for the nozzle analysis. The isolator and combustor analysis was performed using a one-dimensional cycle code. Finally, the stability and control model sized vehicle nose ballast weight and tail planform area to achieve longitudinal stability and control power.

The optimization resulted in a vehicle much different than that of the baseline. The optimal vehicle engine moved forward by 6% of the vehicle length, engine cant angle was reduced by 2 degrees, engine cowl length was reduced by 5% of the vehicle length, and, finally, chine length was reduced by 82% of vehicle length. The optimized vehicle achieved 46% greater airbreathing range while flying at the same Mach-dynamic pressure profile as the baseline. An improvement in effective specific impulse of 9% was realized for the optimized

[16] Engine cowl inclination angle from the vehicle body axis.
[17] Body chines are lifting surfaces outboard of the main fuselage lying in the forebody ground plane.

vehicle over the baseline during the acceleration portion of the mission. Finally, trim drag was lowered by 13% overall.

Research similar to that of Bowcutt has been embarked upon by O'Neil and Lewis [41] as well as Takashima and Lewis [42]. However, their work focused on optimization with a different approach to coupled vehicle-airframe problems. They made use of an inverse analytical method for hypersonic waverider[18] design which reduced calculation requirements by using known flowfields. In the inverse method, desired uniform flowfield conditions at the entrance to the combustor were specified (the desired shape of the inlet curve was also known), and then streamlines were traced forward from the inlet curve to the bow shock to produce the shape of the forebody undersurface that results in the desired conditions. The upper surface was generated by freestream streamlines traced rearward from the undersurface streamline/shock intersection. The known generating flowfields in these studies were produced via the method of osculating cones[19].

In general, the component models developed by O'Neil and Lewis and Takashima and Lewis were essentially the same, with some subtle differences. Two-dimensional planar inlet ramps were incorporated into the designs with all shocks focused on the cowl lip (similar design to that shown in Figure 2-1). A variable cowl was assumed to translate at off-design conditions to maintain both the shock-on-lip condition and shock cancellation at the inlet throat. A quasi-one-dimensional combustor that included area variation, heat addition, friction, mass injection, molecular weight variation, and specific heat variation was based upon Shapiro's influence coefficients [43] to determine the flow properties. The equations were solved step by step from combustor entrance to exit using a fourth-order Runge-Kutta technique. The nozzle was designed for isentropic flow using the two-dimensional method of characteristics and frozen chemical kinetics was assumed throughout the nozzle. Surface forces were predicted by shock-expansion theory and also a hybrid of tangent-wedge and tangent-cone methods.

O'Neil and Lewis, like Bowcutt and others, applied the non-linear simplex method as the optimization scheme. They optimized conically-derived waveriders integrated with scramjet engines for cruise conditions at flight Mach numbers 8-10 and for acceleration at flight Mach

[18] A waverider is essentially any vehicle which uses its own shock wave to increase lift-to-drag ratios and improve overall performance. In these studies, the waverider is considered the forward portion of the vehicle, i.e. upper and lower forebody.

[19] In this method, multiple cones are used to design non-axisymmetric shock patterns allowing greater flexibility in the vehicle design. A designer may use varying conical shock shapes for different portions of the vehicle to improve performance.

number 10, 12, 14, i.e. the vehicle was optimized for individual mission segments of cruise or acceleration and not across an entire mission of segments. The parameters that remained fixed throughout the optimization were flight Mach number, combustor entrance pressure and temperature, combustor equivalence ratio, and vehicle length, density, and wall temperature. Fifteen decision design variables were implemented for the cruise optimization and fourteen for acceleration optimization and were constrained to fall within realistic limits. Behavioral constraints were also imposed on the vehicle design. The cruise and accelerator vehicles were optimized by essentially using Equations (2.2) and (2.1), respectively. However, penalties were included in the objective functions when L = W and T = D were not satisfied for cruise and when L = W was not satisfied for acceleration.

One result of the cruise optimization was that as the flight Mach number increased, the vehicle planform shape became more pointed and the upper surface cross-sectional shape changed from flat for the Mach 8 configuration to more pointed for the Mach 10 vehicle (see Figure 2.2). Engine size increased with increasing Mach number in order to match the thrust to drag which, consequently, decreased the lift-to-drag ratio. Other results of the cruise optimization were a decrease in specific impulse with increasing Mach number and the majority of vehicle lift was produced by the forebody and outboard[20] surfaces of the vehicle. In comparison with the Mach 10 cruise vehicle, the optimal Mach 10 accelerator had a significantly larger engine span (i.e. width) and vehicle volume than the optimal cruiser (see Figure 2-2). The engine was located much farther forward for the accelerator which resulted in a considerable increase in nozzle length. The primary lifting surfaces for the accelerator vehicles were the ramp and nozzle (the outboard surfaces were quite small). When comparing all three accelerators, it was found that all three geometries were relatively similar. However, effective specific impulse decreased and lift-to-drag ratio increased with an increase in Mach number.

Takashima and Lewis chose to use a sequential quadratic programming method for optimization. A design was optimized for maximum range along a constant dynamic pressure trajectory starting from Mach 6 and ending at Mach 10 cruise. For comparison purposes, a design was also optimized for maximum cruise range for a fixed Mach 10 cruise condition. A total of eighteen decision design variables were implemented to define the vehicle geometry,

[20] In the case, forebody includes the undersurface forward of the ramp and the complete upper surface. Outboard refers to the section of the undersurface outboard of the engine and downstream from the start of the ramp.

many subjected to geometric constraints. Both design vehicles were subjected to the same constraints over the entire mission, including the same initial weight.

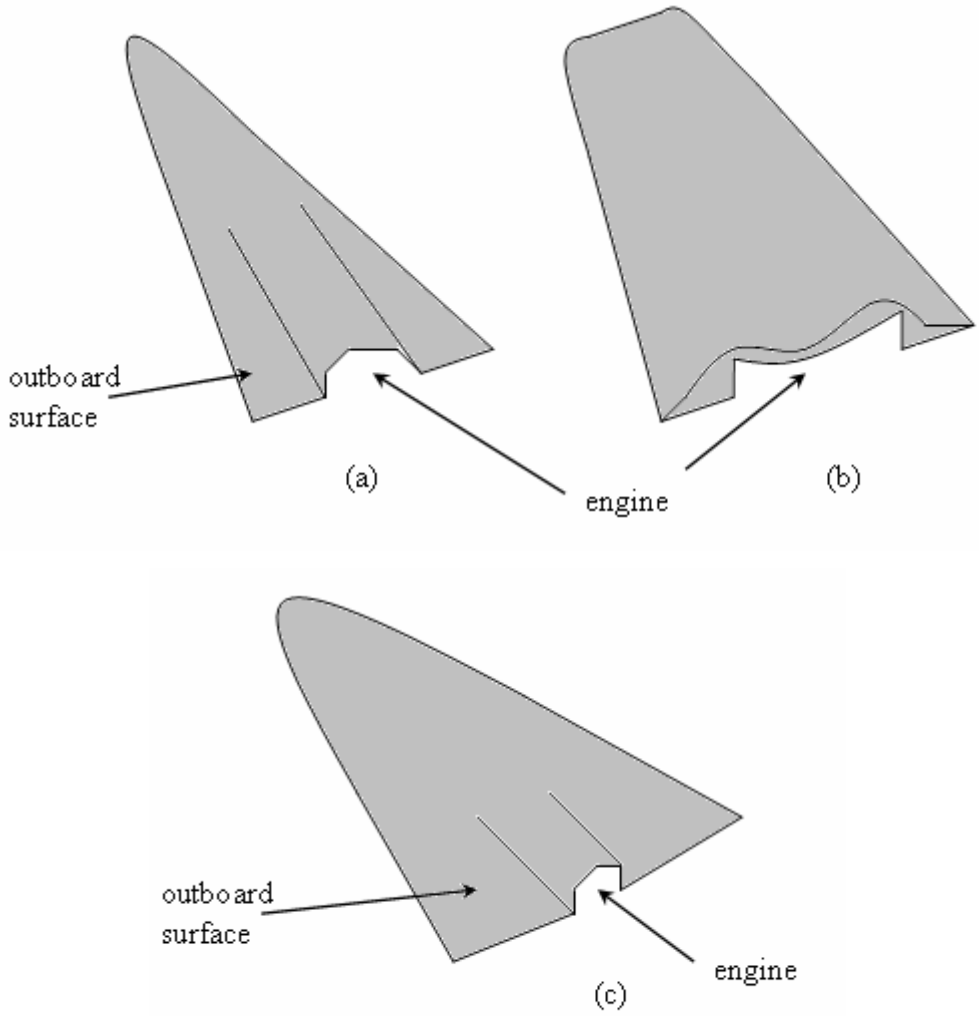

Figure 2-2. Representation of the optimal (a) Mach 10 cruise scramjet integrated waverider, (b) Mach 10 accelerator scramjet integrated waverider, and (c) Mach 8 cruise scramjet integrated waverider determined by O'Neil and Lewis [41].

To compare the performance of the two designs, the hypersonic range for the optimized Mach 10 cruise-range design was calculated along the same trajectory as the optimized total-range Mach 6-10 vehicle. A significant result of the comparison was that the maximum range of the total-range vehicle was only approximately 1% less than the maximum range the of cruise-range design. However, the optimal total-range vehicle covered an 11.5% greater distance during the acceleration phase and the optimal cruise-range vehicle covered a 2.6% greater

distance at the cruise condition. The geometries of both vehicles were relatively similar. The largest differences were the compression surface lengths, top surface angles, and forebody angles. A final result, in general, was that optimized accelerators had a greater engine width than corresponding optimized cruise designs.

The most recent publication (January 2004) in the area of hypersonic vehicle optimization addressed the issue of system level optimization of high speed tactical weapons. Baker et al. [44] developed the Integrated Hypersonic Aeromechanics Tool (IHAT) system which is a multidisciplinary analysis and optimization toolset designed to address the issues of high fidelity analysis and consideration of interdisciplinary interactions for high speed tactical weapons. The IHAT system, constructed in multiple builds, addresses many relevant disciplines important for high speed weapons in an integrated manner. Modules included in IHAT are geometry, aerodynamics, propulsion, trajectory, thermal, structural, stability and control, sensors, lethality, and cost index models. The modules are "glued together" using an Integration Core Module which is responsible for coordinating the execution of the IHAT system and ensuring that all modules are executed in order and required data is transferred. The four types of IHAT runs currently supported by the IHAT system are single point analysis, parametric trade studies, discrete trade studies, and optimization.

The geometry module is responsible for maintaining and updating a parametric geometry module of the configuration being analyzed. This module includes a finite element mesh used by the thermal and structural modules, a surface/volume mesh used by the aerodynamics module, and basic parameters such as volumes and flowpath areas. The aerodynamics module computes aerodynamic performance of the vehicle over the expected flight mission. The aerodynamics module implements a variable-fidelity approach with options ranging from simple surface-inclination methods to complete simulation of the Navier-Stokes equations. The IHAT propulsion module has the capability of computing propulsive performance of solid rocket boosters, ramjets, scramjets, dual combustion ramjets, or non-axisymmetric scramjets. The output of the propulsion module is a database of propulsive efficiency (i.e. thrust, fuel flow rate, specific impulse) as functions of flight condition and throttle setting. The propulsion and aerodynamic modules are used interactively to perform trajectory simulation and optimization. The best overall performance is obtained via the trajectory module once the aerodynamic and propulsion module are available. Several optimization options are available: minimize fuel burn,

maximize range, and minimize time to target. Constraints, such as dynamic pressure and acceleration limits, may be imposed on the trajectory. The thermal and structural modules are responsible, respectively, for computing the aerodynamic and propulsive heating environment as well as the thermal response of vehicle insulation and determining the structural sizing required for the vehicle to withstand load conditions.

The IHAT system implements nested optimizations, with the most successful being surrogate-based optimization (SBO). The SBO strategy creates a response surface, i.e. a 'trust region', over a portion of the design space and then applies conventional gradient-based optimization methods to find the optimum of the approximation. The trust region is then updated and the process is repeated to convergence.

A sample application was conducted using the IHAT system, more specifically, a system-level analysis and optimization of the Air Launched Low Volume Ramjet (ALVRJ). The ALVRJ was a previously built and tested vehicle that incorporated many of the features of a high speed tactical missile and served as a verification and validation test case. Six decision design variables were used in the sample application; each constrained to avoid excessively large perturbations from nominal values. The objective function was a simple weight-based metric termed the "Weight Margin". The Weight Margin was essentially equal to the weight of the payload that could be carried by the vehicle.

The most significant result was an approximate doubling of the weight margin after six iterations of the global optimization. The weight available for payload was approximately 15% of total vehicle weight for the baseline vehicle and 30% for the optimized vehicle. The most significant differences between the baseline and optimized vehicle configuration were that the optimal vehicle had a smaller booster and ramjet combustor, a longer fuel tank, and a somewhat reduced diameter.

2.2 Exergy-Based Methods in the Design/Analysis of Hypersonic Vehicles.

The need for a unified framework in the synthesis/design of high performance aircraft was presented in Section 1.2.It is envisioned that this unified methodology will support all levels of synthesis/design, lead to innovative configurations which maximize overall system efficiency

and minimize energy waste, and ultimately provide a true system-level optimized synthesis/design. A fair amount of work has made strides towards realizing a unified methodology for high performance aircraft systems. Specifically, exergy, work potential, and thrust potential methods have shown much promise in satisfying the aforementioned needs. Therefore, this section is dedicated to illustrating the usefulness of the methods.

2.2.1 Work Potential/Thrust Potential Methods

The concept of thermodynamic work potential[21], based upon the first and second law of thermodynamics, has been shown to hold promise as a universal figure of merit to gauge the performance of propulsion systems [9-12, 14, 15, 45]. Unlike conventional component performance measurements, i.e. component efficiencies, work potential methods applied to propulsion system performance analysis readily lead to generalized representations of engine component performance that are directly comparable to one another. Work potential serves as a basis for developing comprehensive loss accounting systems as well as providing a basis for relating losses directly to vehicle weight, fuel weight, and cost.

Roth [45] and Roth and Mavris [14, 15], exergy, gas horsepower, and thrust potential have shown considerable promise as work potential figures of merit for propulsion system design and analysis. As indicated earlier, exergy is a thermodynamic property which describes the maximum theoretical work that can be obtained from a system in taking it from an initial state to mutual stable equilibrium with the environment. Exergy measures loss relative to the absolute limits of thermodynamics. Gas specific horsepower, on the other hand, is defined by Roth as the ideal work that would be obtained by isentropic expansion of a high-enthalpy gas to atmospheric pressure through an imaginary turbine. Gas specific horsepower is a specific case of exergy and measures losses relative to an ideal Brayton cycle. Finally, thrust potential is defined by Riggins [9-12] as the overall vehicle net thrust work obtainable if the flow of a high-enthalpy gas at the station of interest is expanded isentropically to the exit area of the engine. The difference between each of these figures of merit is in their definition of useful work potential and, therefore, a loss defined by one figure of merit may not be considered a loss by the other figures of merit.

[21] In general, work potential is the ability of some energy source (energy content of fuel) to produce useful physical work (thrust power). The second law of thermodynamics places an upper bound on the maximum work that can be extracted from a fuel.

Roth and Mavris have pointed out that the application of work potential as a tool for vehicle analysis requires two significant considerations. First, the analysis must be able to accommodate the wide operating range typical to vehicle operation. Second, the reference condition for the dead state[22] used in vehicular applications must be allowed to 'float'[23]. They attribute these considerations to the fact that most vehicles operate over a wide variety of ambient conditions and throttle settings when performing their function.

Roth [45] and Roth and Mavris [15] present the general methodology for construction of detailed loss management models as a four step process. However, an initial step, step "0", requires the explicit definition of loss in a way most suited to the analysis at hand, i.e. choose a figure of merit. The four steps are defined as follow:

1. Identify explicitly all loss mechanisms that are significant to the operation of the vehicle.
2. Create a mathematical representation of each loss source, i.e. develop a differential loss management model.
3. Integrate the differential loss model through time over a single vehicle mission or duty cycle to obtain loss chargeable to each loss mechanism.
4. Assign chargeability for each loss to its underlying source.

The first step partitions losses into three general categories: propulsion-chargeable loss, vehicle-chargeable loss, and work storage mechanisms where vehicle and propulsion-chargeable losses can be broken down into more specific classes of loss mechanisms according to the desired level of analysis fidelity. The second step requires application of energy balances in the form of a thermodynamic cycle analysis to yield the detailed information on the thermodynamic state at each engine station and operating condition. Second law analysis can be used in conjunction with the supplied information to determine the work potential at every engine station and operating condition. Step 3 results in an analytical description of all losses and useful work transfer occurring in each component of every vehicle sub-system during the vehicle mission. Finally, step four allocates each loss to the factor(s) that drive it and, therefore, a thermodynamic cost of each design decision can be understood.

[22] Reference state used to determine the value of the exergy, i.e. the state of the "notional reservoir".

[23] This, however, is debatable since the "dead state" is only a reference state which means that the value of "exergy" (or work potential) as any thermo-physical property can only be determined in relative terms, i.e. relative to a given reference state. Thus, the need to vary the "dead state" throughout the mission seems to make little sense from a purely thermodynamic point of view.

Roth and Mavris demonstrated the proposed loss management methods on a lightweight fighter aircraft powered by two J85-GE-21 (gas turbine) engines. In order to demonstrate these methods, a cycle and installation model of the engines and a mission analysis model were developed[24]. The mission considered was a simple subsonic area intercept, consisting of maximum power take-off and climb, subsonic cruise, combat, and loiter. The figure of merit chosen to measure loss of thermodynamic work potential for this application was gas specific horsepower.

During the mission, instantaneous propulsion sub-system and aerodynamic performance were calculated at every flight condition and the power required to overcome each loss mechanism was also calculated. The result of this analysis was a set of data tables for propulsion and aerodynamic losses. These tables displayed the horsepower required to overcome a particular loss mechanism as a function of altitude and Mach number over the "flight envelope". The propulsion sub-system loss plots revealed that inlet losses were only significant at high Mach numbers and turbomachinery losses were greatest at high dynamic pressure conditions. Nozzle and afterbody drag losses were also larger at high dynamic pressure conditions. Exhaust residual kinetic energy was highest at low altitudes and had little dependence on Mach number. The aerodynamic sub-system loss plots showed contours of power required having a marked dependence on dynamic pressure and these plots appeared to be qualitatively similar. However, fuselage wave and skin friction drag and induced drag were the dominant aerodynamic loss mechanisms. These loss plots provided much useful information because they quantified all losses, losses which were readily comparable to one another.

When the instantaneous losses were integrated over the entire mission (see Figure 2-3), it was revealed that total propulsion power loss during climb and combat was much higher than during cruise. Aerodynamic drag power loss was also greatest during climb and combat. Residual kinetic energy left in the exhaust stream was by far the dominant gas-specific power loss during the mission (47% of all losses) (see Figure 2-3). Roth attributed this as a natural consequence of the thermodynamic cycle on which the J85 engine operates. It was also shown that the engine component losses decreased in magnitude from the back to the front of the engine. Finally, it was noted that total loss chargeability's were equivalent to total fuel mass

[24] These models were developed based upon available manufacturer's published data and using well-known cycle, propulsion installation, and mission analysis tools.

chargeability's because the fuel used to offset each source of loss must be proportional to the loss in work potential itself.

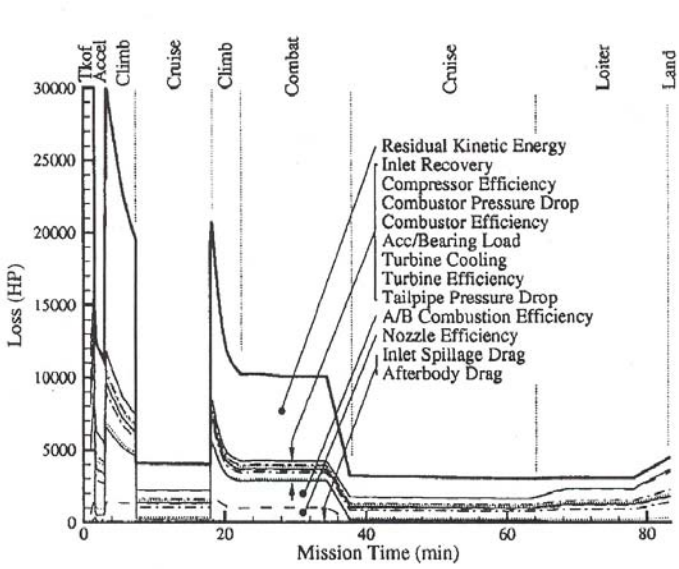

Figure 2-3. Loss of available gas specific power during F-5E area intercept mission. From Roth and Mavris [15]; reprinted by permission of author's.

Roth also derived a series of relationships linking classical efficiency-based performance metrics to modern measures of work potential [14]. The most common component efficiencies (nozzle gross thrust coefficient, inlet pressure recovery, compressor and turbine adiabatic efficiency, etc.) were derived in terms of the three previously mentioned work potential measures. The classical efficiency-based performance metrics were also compared and contrasted with the work potential figures of merit to highlight the strengths and weaknesses of each method.

Riggins [11] and Riggins, McClinton, and Vitt [10] pioneered the analysis of scramjet engines via thrust potential and exergy methods. They developed a method that allowed the calculation of the lost scramjet engine thrust or thrust potential caused by different loss mechanisms (i.e. irreversibilities) in one-dimensional or multi-dimensional flowfields and defined an engine effectiveness parameter to be used in the optimization of engine components. Riggins argued that the ability of the engine to develop thrust efficiently is the ultimate measure of engine performance and, therefore, all proposed methods for evaluating scramjet engine

performance at high Mach numbers must consequently define an engine efficiency whose numerator is vehicle thrust or thrust work delivered to the vehicle.

In these investigations, flow losses (irreversibilities) were produced by friction/viscous effects, shocks, heat diffusion, Rayleigh losses, fuel-air mixing, and non-equilibrium kinetics. The evaluation of the thrust losses caused by these loss mechanisms was based upon the principle that the lost thrust work as measured from that of the reversible engine is recoverable by an additional isentropic expansion of the actual nozzle exit flowfield. This method, referred to as the lost-thrust method, was applied to engines with uncoupled losses and coupled losses. However, coupled losses required a complete differential description of the entropy distribution throughout the engine. It was shown that the lost thrust contributions summed exactly to the difference in thrust between the reversible flowfield and the actual flowfield. The lost-thrust method was used to calculate the lost stream thrust by an additional isentropic expansion utilizing the relation

$$\frac{A_{er}}{A_e} = e^{\frac{\Delta s_{irr}}{R}} \tag{2.3}$$

where *e* refers to the actual nozzle exit area and *er* refers to the effective nozzle exit area. For a known amount of irreversibility and nozzle exit area, Equation (2.3) was applied to determine the effective nozzle exit area required to recover the lost thrust. Coupled loss mechanisms required the exit nozzle to be differentially expanded for each separate differential irreversibility increase, moving from the rear to the front of the engine. The lost-thrust method provided a rigorous identification and ranking of components in which propulsive losses occurred and also the engine location of these propulsive losses.

In [10], Riggins, McClinton, and Vitt demonstrated these methods (lost-thrust and thrust potential) for the analysis of thrust losses in a scramjet engine using a one-dimensional cycle code with detailed second law (irreversibility) accounting. The analysis was implemented on a generic hypersonic engine configuration, which include inlet/forebody, combustor, and nozzle, at flight Mach number 12 conditions and fixed fuel injection conditions. As a result, the actual thrust potential, the various loss thrust increments, and the ideal thrust potential were plotted (see Figure 2-4) versus axial engine distance. From this figure, it was evident the incomplete combustion losses were by far the largest loss mechanism followed by mixing losses. It was also

shown that when the thrust losses caused by irreversibilities were added to the actual thrust potential, the sum recovered exactly the corresponding reversible flow.

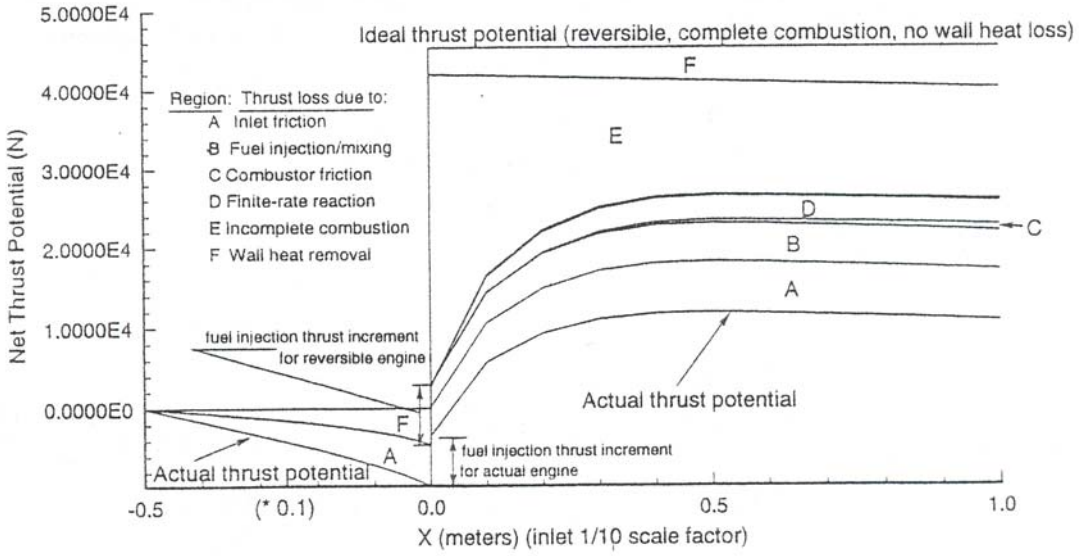

Figure 2-4. Thrust potential and losses versus axial distance for engine flowfield. From Riggins, McClinton, and Vitt [10]; reprinted by permission of the American Institute of Aeronautics and Astronautics, Inc.

An overall engine thrust effectiveness parameter was also presented in [10] and was defined as the ratio of the actual net thrust across the engine to the ideal engine net thrust. The methods developed in this reference eliminated the need to actually compute a reversible high-enthalpy flowfield[25] and, therefore, evaluation of the ideal engine net thrust was relatively straightforward. The engine effectiveness parameter was developed to evaluate and compare scramjet engine thrust performance.

Riggins also illustrated and clarified issues relating to the thrust-potential and exergy methods (when applied to high-speed aerospace engines) using simple one-dimensional steady flows with friction, Rayleigh heat addition, and incomplete combustion losses [9, 12]. It was shown that a conventional exergy-based rational efficiency[26] yielded less effective design information than the thrust-potential method. This was attributed to the fact that the

[25] This is based upon slowing the flow reversibly to Mach zero before heat addition.

[26] The rational efficiency of an engine component was defined as the ratio of the exergy exiting the component to the total exergy entering the component. This rational efficiency was developed in earlier work by Curran and Murphy [23] as an exergy-based measure of engine performance. However, this measure appears more appropriate for stationary engines than aerospace engines. An exergy-based measure which does work well for aerospace engines, the thermodynamic effectiveness [24], is given in Chapter 6 of this thesis (Section 6.1).

conventional exergy method did not account for the degree of nozzle expansion and the open nature of the Brayton cycle (essential cycle of a scramjet engine). Additionally, an engine-based exergy[27] was developed to account for the open nature of the aerospace engine cycle.

In these references, a component design problem was posed using both the exergy-based rational efficiency and thrust-potential-based engine effectiveness. The design challenge was to find the combustor length of a high speed engine (scramjet engine) that optimizes the performance of the vehicle. A simplified scramjet with a steady flow of air at flight Mach 12 conditions was illustrated in this example (see Figure 6-1). An isentropic inlet and nozzle of equal area ratios and a constant area combustor with Rayleigh heat addition and high skin friction were implemented in the model. Although the total energy expended was held constant, the actual heat released was determined by using an exponential combustion efficiency distribution. The nature of this function allowed the ongoing friction, at some point, to negate the benefit of the progressively smaller amounts of heat release and arrive at an optimal combustor length. The engine effectiveness parameter predicted an optimal combustor length of 0.46 m and was maximized at the engine axial station where the sum of the lost thrust caused by irreversiblities was minimized. The rational efficiency predicted an optimal combustor length of 0.952 m, approximately twice the length predicted utilizing the thrust effectiveness. The exergy-based method optimal combustor length also produced approximately 20% less net engine thrust.

A comparison of component losses using the aforementioned methods was performed on a simple one-dimensional flow (standard air) through a 10-m long constant area adiabatic duct with friction. The duct was arbitrarily sectioned into an upstream component Y and downstream component Z, with component Y being one-third of the duct length. Exergy losses and stream thrust losses were both measured from the duct inflow values. Component Y had a stream thrust loss of 50.6 N and an exergy loss of 174 kJ/kg. Component Z had a stream thrust loss of 88 N and an exergy loss of 168 kJ/kg. It was therefore shown that the exergy method did not correctly rank components (as to largest performance losses) and yielded no useful propulsive information.

A final measure of the issues involved with assessing component performance losses was illustrated by revisiting the optimal combustor length problem. The combustor length was fixed

[27] Whether or not the quantity so defined is "exergy" is problematic. However, a discussion of the details of this quantity is beyond the scope of this thesis.

at 1 m and the combustor was divided into two separate components in a similar manner as the duct problem. A design problem was to identify the component in which the greatest frictional losses occurred and then optimize that component by eliminating skin friction within that component; ultimately seeing which method (rational efficiency or thrust-potential) resulted in a more optimal engine (greater thrust). Exergy losses caused by friction were greatest in component Y and thrust losses caused by friction were greatest in component Z. Elimination of the skin friction within the identified component led to the optimal engines for both methods. The thrust-potential method produced an engine with 20% more engine net thrust than the rational efficiency method. This clearly illustrated that the thrust-potential method in conjunction with the lost-thrust method provided accurate information in terms of identifying component losses for high speed engine applications, whereas the rational efficiency method did not.

Riggins, Taylor, and Homan [13] continued and extended work on these methods, specifically towards the auditing and optimization of high speed vehicles. A theory was developed for the detailed characterization of high-speed vehicle performance in terms of irreversibility, combustion, and flow area relief/flow angularity. A full performance audit, performance losses and gains, was completed in representative scramjet-powered vehicle simulations. As done in earlier work, it was shown that losses can be stripped out of individual streamtubes to yield reversible forces and performance lost by a particular component. Some major findings in this work was that the combustor was the main source of irreversible entropy production for the entire vehicle, wake mixing cannot be ignored in vehicle optimization, and vehicle vertical forces are not significantly affected by irreversible entropy production.

2.2.2 Exergy Methods for System-Level Multidisciplinary Analysis

Moorehouse [4] has proposed the need for a unifying framework and a set of metrics to facilitate system-level analysis and optimization of aerospace vehicles (with focus on hypersonic vehicles) and suggested that exergy-based methods show potential to do so. It was postulated that exergy-based methods would allow more complete system integration, manage the connection of all traditional results into a design framework with a common metric, and permit explicit trades between dissimilar technologies in a system context. It was also suggested that a

minimum exergy destruction solution via system-level analysis should, ideally, be the same as the more traditional minimum weight solution.

In [4], the development of a systems-level approach for vehicle synthesis/design in exergy terms is illustrated. It is shown that mission requirements can be stated in terms of work to be accomplished; and, thus, total mission requirements can be defined as an energy (exergy) problem. Consequently, each sub-system of a vehicle can be analyzed as a component in finding the most efficient way to accomplish that work.

Moorhouse illustrated the synthesis/design process by creating a 'business case' that the work to be done is composed of work the customer wants to purchase plus the overhead work. The customer work is defined as the work necessary to deliver a specified payload to a certain altitude and velocity and maintain a power supply to accomplish what is required. The rate of doing customer work is written as

$$\frac{dw_c}{dt} = W_p \frac{dE_w}{dt} + P_p + D_p U \tag{2.4}$$

where the first term on the right hand side represents the work required to generate the specific energy of some payload weight, the second term is the power supply required by the payload, and the last term is the work to overcome drag chargeable to the payload. The weight specific energy was defined as the total of kinetic plus potential energies per unit of weight, i.e. $E_w = h + U^2/2g$. Integration of Equation (2.4) over a total mission represents the quantity of work to be considered as a fixed requirement. The overhead work, as defined by Moorhouse, is the work that has to be done carrying the weight of the vehicle plus the required fuel throughout the mission.

The rate of doing overhead work is expressed as

$$\frac{dw_o}{dt} = W \frac{dE_w}{dt} + DU \tag{2.5}$$

where W is the sum of all vehicle components except for the payload. The customer pays for both the mission plus the overhead work done, which is accomplished using the exergy of the fuel burned.

At the system level, the conservation of energy in the time interval dt is shown to be

$$-\eta H dW = dw_c + dw_o \tag{2.6}$$

The energy content per weight of the fuel, H, and the overall system efficiency, η, were incorporated into Equation (2.6). The overall efficiency introduces consideration of the first and second laws of thermodynamics as well as that of all components of the vehicle. Moorhouse explains that Equations (2.4)-(2.6) represent the balance between the work achieved from the exergy of the fuel and the changes in payload and aircraft specific energy plus the exergy destroyed to overcome drag, i.e. mission work. The synthesis/design problem posed is to minimize the overhead work and maximize the overall system efficiency through the use of exergy as the common currency.

Moorhouse, Hoke, and Prendergast [6] applied these methods (i.e. the exergy process) to the design of the inlet of a hypersonic vehicle. The addition of a 'device' was considered to maintain the inlet shock focused on the cowl lip to avoid problems of mass spillage or shock ingestion. The device used the concept of energy addition/extraction with the inlet flow in order to tailor the Mach number and shock angle. The device was incorporated to avoid the weight and complexity of a movable inlet system.

In this analysis, a nominal inlet Mach number and ramp angle were specified. Then, for incoming flow over a range of Mach numbers, the heat input required to achieve the nominal Mach number was found using Rayleigh line analysis. Thermal energy was exchanged with a notional thermal reservoir in order to achieve the required heat addition/extraction. The thermal reservoir was examined for cases of constant temperature and a linear profile (to approximate ideal heat exchange). The entropy generation rates (exergy destruction rates) were calculated for both the energy exchange process and the shock process.

From this analysis it was shown that exergy destruction was much greater when thermal energy shock tailoring was incorporated as opposed to an inlet with no thermal energy exchange. There was an exergy benefit if the heat exchange process was close to ideal heat exchange. Even though the no "energy exchange" process had less exergy destruction, the affects of mass spillage or shock ingestion were not considered in this analysis and would ultimately need to be taken into account during a complete system analysis. Also, the large changes in the thermodynamic properties of the inlet flow as a result of energy exchange would need to be

considered, i.e. the effects on combustion performance. Finally, the weight consideration of adding such a device to a vehicle was demonstrated by Moorhouse, Hoke, and Prendergast.

2.2.3 Additional Exergy/Available Energy Research in Advanced Aircraft Analysis

A fair amount of work on exergy methods applied to high performance aircraft analysis has been presented in the literature. Although many of these works are directed towards specific vehicle components or systems, the methodologies undertaken and the results of these analyses have presented valuable insights into exergy methods for aerospace applications.

Ravichandran and Murthy [46] engaged in a generalized available energy analysis of a scramjet combustor. The performance of a scramjet combustor was established in terms of four available energy utilization effectiveness parameters based on available energy or exergy. Ultimately, these parameters were a measure of how well the energy input into the combustor was converted into the scramjet engine thrust work. One parameter referred solely to the combustor, while the other three were based on thrust generation by a nozzle attached to the combustor. Parameters such as combustor entrance Mach number, combustor equivalence ratio, heat loss fraction, and friction and shock loss fraction were varied to evaluate the trends of the available energy effectiveness parameters, i.e. scramjet engine performance.

Another analysis of scramjet engines using exergy methods was conducted by Brilliant [47]. In this work, performance of scramjet systems were predicted using energy balances and then exergy calculations were performed for the end states obtained from the conventional anaylsis. Various exergy measures were plotted for the inlet, combustor, and nozzle as a function of flight Mach number and the trends of these figures were analyzed. Brilliant attributed a greater understanding of the interactions of the components to the use of the exergy analysis.

Camberos and Moorhouse [7] have proposed a methodology to incorporate the second law of thermodynamics into existing computational fluid dynamics (CFD) algorithms. The objectives included the development of the theoretical framework for calculating local and global entropy generation rates, entropy-based numerical metrics, and residuals. Also, the approach taken was to formalize the entropy and entropy generation equation into a form appropriate for the unstructured Euler/Navier-Stokes solver. The theoretical expressions were to be coded and then validated and tested by comparing the induced drag of two wing planforms [17]. Camberos

and Moorhouse presented an example of the significance of using second law analysis for the design of planforms. It was stated that classical lifting-line theory predicts that a planform with elliptical lift distribution will minimize induced drag and recent work has shown that explicit consideration of entropy generated in the wake shows that a parabolic lift distribution will minimize induced drag. Also, when using CFD methods, it was emphasized that separation of the numerical entropy generation from the physical model needs consideration.

Camberos [8] has also worked on quantifying irreversible losses for magnetohydrodynamic (MHD) flow simulation. The appropriate equations for MHD fluid flow were first developed and then were supplemented with the entropy and exergy balance equations. The inclusion of the second law into this complex physical process was to complement and assist the development of a unified approach to multidisciplinary optimization with minimum entropy generation (minimum exergy destruction) as the objective function.

Aside from hypersonic vehicle related topics, Figliola, Tipton, and Li [16] applied an exergy approach to the decision-based design of integrated thermal aircraft systems. Specifically, both a traditional energy-based approach and an exergy-based approach were utilized in the design of the environmental control system (ECS) of an advanced aircraft. Analytical models of the ECS were developed for both methods and compared to assess the ability of each method to suggest optimal design paths. Multiobjective optimization tradeoff studies between design weight and entropy generated were used to determine the optimal design points. As a result, the two analyses provided similar but different decision solutions.

Paulus and Gaggioli [18] have proposed a method for creating overall objective functions and weighting factors for a light experimental aircraft. Bejan [19, 20] has presented a constructal theory for the energy systems of aircraft, one example being the derivation of a complete structure of a heat exchanger for an ECS based upon exergy methods. Others who have applied work potential and exergy methods to high-performance aircraft are Czysz and Murthy [23], Curran and Craig [22], and Curran and Murphy [21].

Chapter 3

Hypersonic Airbreathing Propulsion Technical Background

The purpose of this chapter is to facilitate and supplement the remainder of the work in this thesis. The fundamental features of hypersonic flight and hypersonic vehicles along with a moderately comprehensive vehicle component description and investigation is presented in this chapter. Relevant equations of compressible fluid mechanics and thermodynamics which will be referred to throughout this thesis are briefly presented and discussed.

3.1 Fundamental Definitions and Relations

A good place to begin the discussion of the fundamental definitions and equations of hypersonic flight is a description of the forces acting on an aerospace vehicle in flight. Figure 3-1 depicts the system of forces acting on the aerospace vehicle as it carries out some flight trajectory. It is evident from this figure that the instantaneous installed engine thrust (T) and vehicle drag (D) are parallel to the instantaneous vehicle velocity (V), and the vehicle lift (L) is perpendicular to the instantaneous vehicle velocity. The weight (W) or gravitational force is directed towards the center of the Earth. The vehicle flight path angle (θ) is defined as the angle between the vehicle velocity and the horizontal.

Application of Newton's second law of motion along an axis parallel to the instantaneous velocity multiplied by the instantaneous velocity leads to the following energy balance on the aircraft:

$$\{T - D\}V = W\frac{dh}{dt} + \frac{W}{g}\frac{d}{dt}\left(\frac{V^2}{2}\right) \tag{3.1}$$

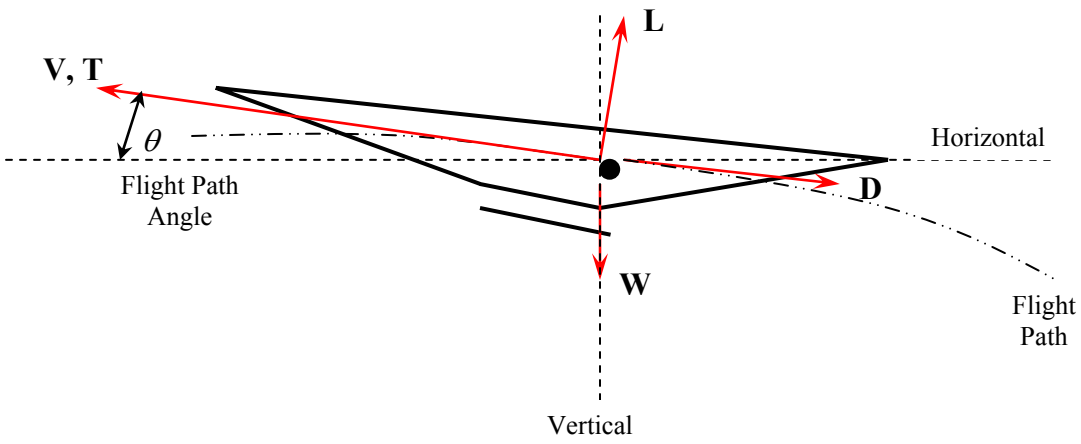

Figure 3-1. Forces acting on an aerospace vehicle in flight.

The left-hand side of Equation (3.1) represents the net rate of mechanical energy input. The first and second terms on the right-hand side signify the storage rate of potential energy and kinetic energy, respectively. Looking at Figure 3-1 from a propulsion standpoint, the engine thrust produces vehicle acceleration while overcoming the vehicle drag and supporting part of the vehicle weight. Equation (3.1) and Figure 3-1 reveal two significant details of aircraft flight. The first is that if the vehicle is neither accelerating/decelerating or ascending/descending then the vehicle installed thrust equals vehicle drag, i.e. $T = D$. This flight condition is known as vehicle *cruise*. The second detail is that for constant altitude flight or for a sufficiently small flight path angle (θ) the vehicle lift equals the instantaneous weight, $L = W$. The well known aircraft relationships for lift and drag are defined as follows:

$$L = nW = q_0 C_L S \tag{3.2}$$

$$D = q_0 C_D S \tag{3.3}$$

where n is the load factor, which is equal to the number of g's perpendicular to the direction of the velocity.

A parameter frequently used in aerospace applications as a scaling factor for pressures and forces exerted on an aircraft is dynamic pressure (q_0) . As seen in Equation (3.4), dynamic pressure can be determined from the static properties of the atmosphere at a given flight

elevation and knowledge of the velocity or Mach number of the atmosphere as seen from the moving vehicle such that

$$q_0 = \frac{\rho_0 V_0^2}{2} = \frac{\gamma_0 p_0 M_0^2}{2} \tag{3.4}$$

The dynamic pressure has proven to be valuable for calculating the forces exerted on conventional aircraft, specifically the lift and drag (Eqs. (3.2) and (3.3)). It is also effective in determining forces experienced by hypersonic vehicles with the most popular method being the modified Newtonian theory [2, 3]. The modified Newtonian theory predicts pressure coefficients and local surface static pressures of inviscid hypersonic flows through a local surface inclination method.

The fact that dynamic pressure is a significant parameter in vehicle surface force determination leads to two critical implications. Structural forces and vehicle drag can become quite excessive if the dynamic pressure is too large. Secondly, if dynamic pressure is too small, the wing area required for sustained flight may become unreasonably large. Therefore, hypersonic vehicles are essentially designed to operate within a fairly narrow range of q_0, approximately $20{,}000 - 90{,}000\ N/m^2$, and the tendency is to fly the vehicles along the trajectory of their highest allowable q_0. [1]

Standard day altitudes versus Mach number trajectories for the aforementioned dynamic pressure design range are provided in Figure 3-2. These trajectories can be generated in a straightforward fashion by selecting desired combinations of dynamic pressure and Mach number, using Equation (3.4) to calculate the static pressure, and then obtaining altitude by interpolation of the table in Appendix B of [1].

There are a few notable attributes of constant dynamic pressure trajectories and Figure 3-2 worth emphasizing. First, truly enormous flight altitudes would be required for hypersonic vehicles if it were not for the exponential decrease of static pressure with altitude [1]. Second, freestream mass flow per unit area is proportional to dynamic pressure at a given Mach number. Therefore, it is imperative that hypersonic vehicles are flown at as high a dynamic pressure as other considerations will allow in order to maintain mass flow and engine thrust [1]. Finally, if small dynamic pressure trajectories are chosen, the freestream static pressure may be

excessively low resulting in unreasonable inlet compression ratios for proper operation of the combustor. As previously mentioned, small q_0 trajectories may also require large wing or lifting surface areas.

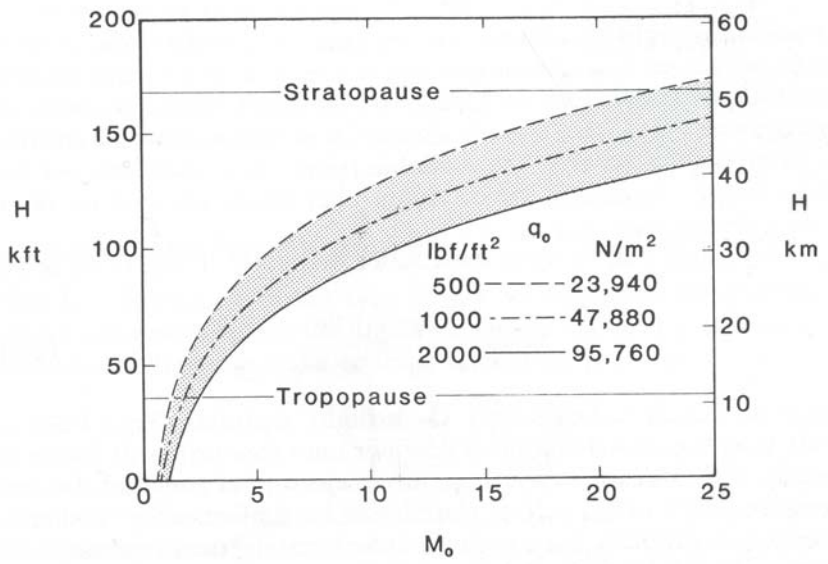

Figure 3-2. Standard day geometric altitude versus flight Mach number trajectories for constant dynamic pressure. From Heiser et al. [1]; reprinted by permission of the American Institute of Aeronautics and Astronautics, Inc.

It is of significance to be aware of the general behavior of air because it is the essential fluid upon which airbreathing engines depend. Therefore, an issue that is not trivial to hypersonic flight is the equilibrium behavior of air and the validity of the ideal gas assumption. The importance of this issue takes affect at high static temperatures and low static pressures, both of which are commonplace to hypersonic flight.

By definition, an ideal gas is a substance, at relatively high T and sufficiently low P, which behaves as a single-phase fluid in which each molecule is so weakly coupled to the other molecules that it hardly experiences their presence [24]. The departure of a gas from ideal behavior can be estimated from the compressibility factor, where it is customary to use reduced values of temperature, pressure, and volume in the expression for compressibility factor. It is proposed that as long as the reduced pressure is less than about 2.0 and the reduced temperature is greater than about 1.8, the compressibility factor will be within a few percent of unity (substance exhibits ideal-gas behavior) [1]. In [1] it is suggested that the reduced pressure

should never exceed 2.68, the reduced temperature should never be less than 1.64, and the worst combination of them should never occur due to the nature of the compression process (P and T increase simultaneously) [1]. Thus, based on known conditions for hypersonic aircraft, it a reasonable assumption that air behaves as an ideal-gas for the analysis of this thesis.

The significance of the ideal-gas behavior assumption is that specific heats of constant pressure and volume (consequently, the specific heat ratio γ) are functions of temperature only. It also permits application of the *ideal gas equation of state*, which will be presented shortly. Figure 3-3 presents the equilibrium ratio of specific heats of air as a function of temperature and pressure. The figure makes it evident that for the temperature range of air pertinent to this thesis, ideal-gas behavior is a valid assumption. It also shows that at lower temperatures (below about 500 K), air can be approximated as a perfect gas, meaning specific heats are a weak function of temperature and are conceivably constant.

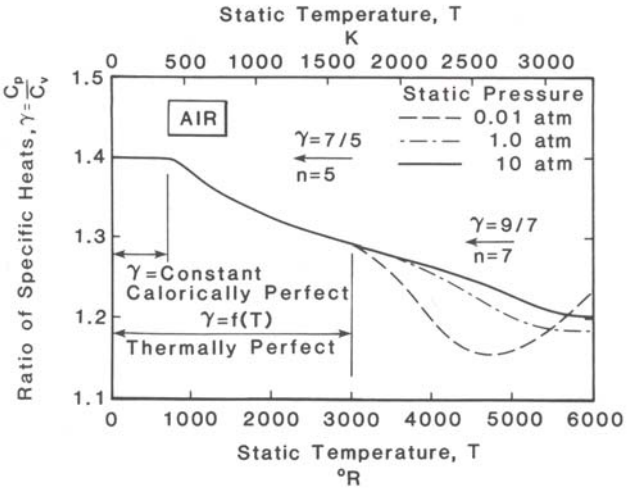

Figure 3-3. Equilibrium ratio of specific heats of air as a function of static temperature and static pressure. From Heiser et al. [1]; reprinted by permission of the American Institute of Aeronautics and Astronautics, Inc.

The equilibrium behavior of several major constituents of air as a function of static pressure and temperature are presented in Figure 3-4. A static pressure of 0.01 atm was chosen because this is approximately the lowest pressure expected to be found in the hypersonic flight envelope. Similar results would occur at higher static pressures; however, the higher pressures merely delay the onset of dissociation of the constituents.

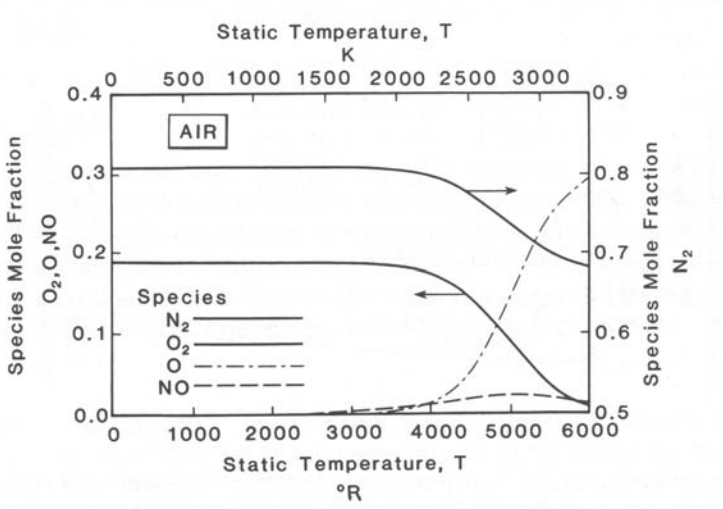

Figure 3-4. Equilibrium mole fraction composition for several constituents of air as a function of temperature. Static pressure fixed at 0.01 atm. From Heiser et al. [1]; reprinted by permission of the American Institute of Aeronautics and Astronautics, Inc.

It can be seen in Figure 3-4 that the dissociation of molecular oxygen (O_2) into atomic oxygen (O) is the principal chemical reaction. It is also evident that the dissociation of molecular nitrogen (N_2) into atomic nitrogen (N) as well as the formation of nitric oxide (NO) is practically insignificant. For the air temperature range of interest in this thesis work (less than 2000 K), dissociation of air will be assumed irrelevant.

Finally, a presentation of the governing and supporting equations is fundamental to any analysis. The finite control volume governing equations are presented because this analysis approach was essential to the thesis work. The governing balances of mass, momentum, energy, and entropy are given in Equations (3.5) to (3.8), respectively.

$$\frac{dm}{dt} = \sum_q \dot{m}_q^{\leftarrow} \tag{3.5}$$

$$\sum F = \frac{d}{dt}\iiint_{c.v.} \rho V d\forall + \iint_s V\left(\rho V \cdot dA\right) \tag{3.6}$$

$$\frac{dE}{dt} = -\dot{W}_s^{\rightarrow} - P_0\dot{\forall} + \dot{Q}_0^{\leftarrow} + \sum_k \dot{Q}_k^{\leftarrow} + \sum_q \dot{m}_q^{\leftarrow}\left(h_q + \frac{V_q^2}{2} + gz_q\right) \tag{3.7}$$

$$\frac{dS}{dt} = \frac{\dot{Q}_0^{\leftarrow}}{T_0} + \sum_k \frac{\dot{Q}_k^{\leftarrow}}{T_k} + \sum_q \dot{m}_q^{\leftarrow} s_q + \dot{S}_{irr} \tag{3.8}$$

In the above equations, the subscript q refers to any bulk-flow port (inlet or exit) where mass flow crosses the control volume boundary. The subscript 0 refers to interactions with the environment and the subscript k refers to interactions with other systems. The left-hand side of Equation (3.6) represents the sum of all forces acting on the control volume whereas the right-hand side represents the rate of increase of linear momentum within the control volume added to the net rate of linear momentum crossing the control volume boundary. In Equation (3.7), the first and second term on the right-hand side signify the transfer of energy by means of a work interaction. The third and fourth terms represent the transfer of energy by means of a heat interaction and the last term denotes the transfer of energy by bulk-flow. It is important to note that work interactions do not appear in the entropy balance because work involves a transfer of energy only with no entropy.

Two supporting equations that are utilized frequently in the control volume analysis are the ideal gas equation of state and the enthalpy relation for an ideal gas, i.e.

$$P = \rho RT \tag{3.9}$$

$$dh = c_p(T)dT \tag{3.10}$$

The equation of state (EOS) is convenient for relating properties at a given equilibrium state. Equation (3.10) shows that the specific heat at constant pressure and, consequently, the specific enthalpy are functions of temperature only as well.

Two other equations that are extremely convenient for a point-to-point analysis of hypersonic flows are that of total temperature and total pressure. The expression for total temperature and total pressure derived from energy and momentum balances are [3]

$$T_t = T\left(1 + \frac{\gamma - 1}{2} M^2\right) \tag{3.11}$$

$$P_t = P\left(1+\frac{\gamma-1}{2}M^2\right)^{\frac{\gamma}{\gamma-1}} \tag{3.12}$$

where it obvious that they are both strong functions of Mach number. Total temperature is a fixed property of constant energy flows of perfect gases and total pressure is a fixed property of constant energy isentropic flows of perfect gases. As will be seen in the next section, changes in total pressure are directly linked to changes in entropy.

3.2 Shock/Expansion Overview

Shock and expansion processes are quite prevalent during high speed vehicle flight, and it is, therefore, of utmost importance to have a good understanding of how these mechanisms work and where and why they arise. It is also critical to understand these mechanisms because the performance of hypersonic vehicles depends largely upon them, as will be seen in later chapters. Thus, the following three sections make an attempt to provide a detailed explanation and discussion of the aforementioned processes.

3.2.1 Oblique Shock Theory

A complete and thorough comprehension of the shock wave process and its ramifications on flow properties is essential to a study of compressible flow. The shock process represents an abrupt change in fluid properties in which finite variations in pressure, temperature, and density occur over a shock thickness comparable to the mean free path of the gas molecules involved [48]. The shock process itself is adiabatic, thermodynamically irreversible; and mass, momentum, and energy are conserved throughout the process.

Two types of shock waves occur in supersonic compressible flow. The first type is a normal shock wave which is effectively a plane shock normal to the direction of flow. Therefore, changes in the flow properties occur only in the direction of flow. The second type occurs when a compression shock wave is inclined at an angle to the flow direction. This is referred to as an oblique shock wave. The oblique shock wave process results in a change in flow direction across the wave. Consequently, a second momentum equation is needed for derivation of the oblique shock equations. For both types of shocks waves, the shock is assumed

thin enough so that there is no area change across the wave [48]. A detailed description of only the oblique shock wave is given below because it is somewhat more complex and is the predominant shock wave found throughout the vehicle analysis. Normal shocks are handled in a very similar fashion.

An oblique shock must occur when a supersonic stream is forced to undergo a finite change in flow direction into itself due to the presence of a body in the flow and the stream is unable to gradually adjust to the presence of the body. There are two main types of oblique shocks referred to throughout this paper. One type occurs during the presence of a wedge in a supersonic stream (Figure 3-5) and the other is a result of supersonic compression in a corner (Figure 3-6). For small flow deflection angles, the oblique shock wave remains attached to either the apex of wedge (Figure 3-5) or to the compression corner (Figure 3-6). The flow after the shock is uniform and parallel to the body's surface, with the flow having been turned through the wedge half-angle or corner deflection angle, both of which are defined by the symbol θ (see Figure 3-7). These angles are considered synonymous because one can simply imagine the corner deflection to be a wedge half-angle.

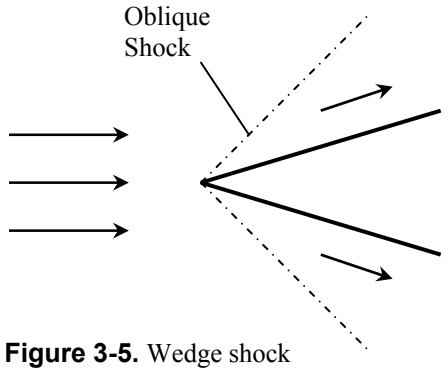

Figure 3-5. Wedge shock

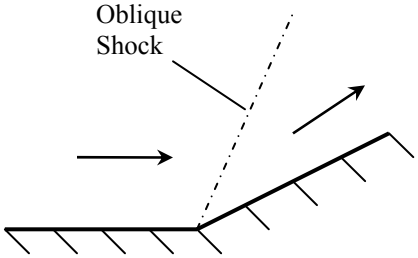

Figure 3-6. Corner shock

Figure 3-7 provides a more physical representation of the flow characteristics of an oblique shock wave. As can be seen from this diagram, the upstream (state 1) and downstream (state 2) velocities are broken down into their components tangential and normal to the oblique shock. From the geometry of the oblique shock wave and the definition of Mach number,

$$M_{1_n} = M_1 \sin\beta \tag{3.13}$$

$$M_{1_t} = M_1 \cos\beta \tag{3.14}$$

$$M_{2_n} = M_2 \sin(\beta - \theta) \tag{3.15}$$

$$M_{2_t} = M_2 \cos(\beta - \theta) \tag{3.16}$$

where θ is the local flow deflection angle and β is the oblique shock angle. The deflection angle and shock angle are related by the θ-β-M correlation (Equation (3.17)) which specifies θ as a unique function of M_1 and β, i.e

$$\tan\theta = 2\cot\beta \frac{M_1^2 \sin^2\beta - 1}{M_1^2(\gamma + \cos 2\beta) + 2} \tag{3.17}$$

For a known upstream Mach number M_1 and deflection angle θ, Equation (3.17) can be solved iteratively or by using a root finder to calculate the shock angle. The equations of continuity, momentum, and energy can be written for uniform, supersonic flow over the control surface indicated by the red dashed lines in Figure 3-7.

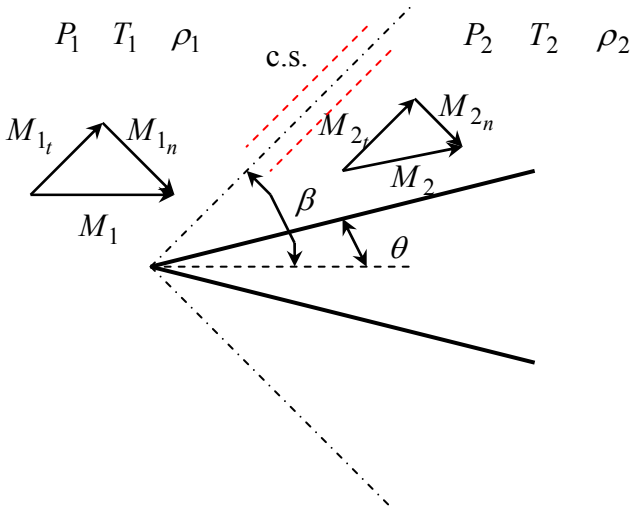

Figure 3-7. Oblique shock diagram

The application of these equations leads to two important results, namely, the Mach number (and velocity) components tangential to the wave are equal, $M_{1_n} = M_{2_n}$, and the total

temperature remains constant throughout the shock process, $T_{t_1} = T_{t_2}$. This simply means that an oblique shock acts as a normal shock for the component normal to the wave. Algebraic manipulation of the continuity, momentum, and energy equations along with the perfect gas equation of state leads to relations for the pressure and temperature ratios across the shock as well as an equation for the downstream normal Mach number as a function of the upstream normal Mach number [3]. They are

$$M_{2_n}^2 = \frac{M_{1_n}^2 + \frac{2}{\gamma - 1}}{\frac{2\gamma}{\gamma - 1} M_{1_n}^2 - 1} \tag{3.18}$$

$$\frac{P_2}{P_1} = \frac{1 + \gamma M_{1_n}^2}{1 + \gamma M_{2_n}^2} \tag{3.19}$$

$$\frac{T_2}{T_1} = \frac{1 + \frac{\gamma - 1}{2} M_{1_n}^2}{1 + \frac{\gamma - 1}{2} M_{2_n}^2} \tag{3.20}$$

With knowledge of the upstream Mach number M_1 and deflection angle θ, Equations (3.13), (3.17) and (3.18) produce the downstream normal component of the Mach number, M_{2_n}. Thus, equations (3.19) and (3.20) can be easily solved to obtain the pressure and temperature ratios across the wave. This process can be repeated for multiple-shock mechanisms with the local deflection angle θ and shock angle β measured from the previous deflection angle (surface angle).

Now, the perfect gas expression for the change in entropy across the shock and an entropy balance over the control surface gives the irreversibility of the shock process which can then also be related to total pressure losses across the shock wave, namely,

$$s_{irr} = s_2 - s_1 = c_p \ln\left(\frac{T_2}{T_1}\right) - R \ln\left(\frac{P_2}{P_1}\right) \tag{3.21}$$

$$\frac{s_2 - s_1}{R} = -\ln\left(\frac{P_{t_2}}{P_{t_1}}\right) \tag{3.22}$$

A few other characteristics of the oblique shock equations are worth mentioning here and can be seen in Figure 3-8 which shows the variation of shock wave angle with flow deflection angle for a given Mach number. A more detailed depiction of Figure 3-8 for numerous Mach numbers can be found in Appendix C of [48].

For a given M_1 and θ, two solutions of β are possible (as seen in Figure 3-8). There may be a weak shock, with M_2 either supersonic or slightly less than 1, or a strong shock, with M_2 subsonic [48]. In both cases, the supersonic flow is turned through the same angle, however, the strong shock is accompanied by a much larger pressure ratio. When a wedge or airfoil travels through the atmosphere at supersonic velocities with an attached oblique shock, only the weak solution is found to occur because large pressure differences cannot be supported [48].

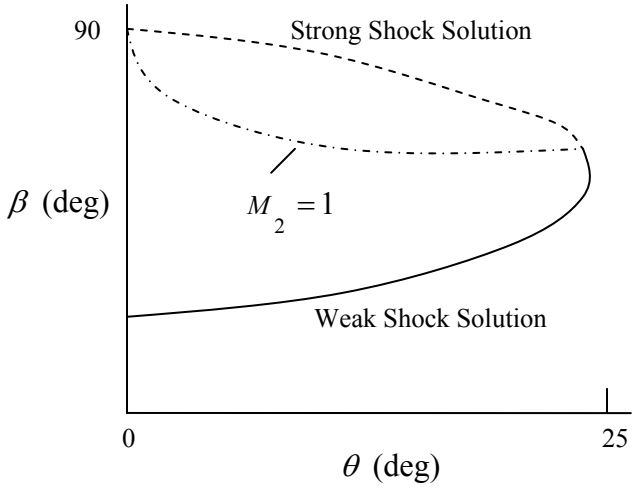

Figure 3-8. Shock angle versus deflection angle

Another characteristic of the oblique shock equations (also seen in Figure 3-8) is that large turning angles θ can produce no solution. These conditions result in a shock that is no longer attached to the apex of the wedge or the expansion corner as seen in Figures 3-5 and 3-6. The detached shock is a curve with the shock strength diminishing progressively from that of a

normal shock at the former attachment point to that of a Mach wave far from the body [48]. Therefore, a detached shock produces the entire range of shock solutions for a given Mach number. Subsonic flow occurs in the vicinity of the wedge apex or compression corner and supersonic flow occurs farther back along the wedge or farther out in the flow around the corner. Due to the non-uniformity of the flow properties, it is highly undesirable to have detached shocks occur anywhere throughout the hypersonic vehicle flowpath.

Oblique shock reflections and conical shock waves are two other types of supersonic flow phenomena. The dynamics of these processes will not be discussed here, but further discussion of these topics can be found in [48].

3.2.2 Gradual Compressions

As discussed in the previous section, an oblique shock occurs when a supersonic stream undergoes a sudden change in flow direction. However, supersonic compression in a more gradual fashion can approach an isentropic process. Allowing supersonic flow to pass through several weak oblique shocks rather than one strong shock reduces the total pressure losses (entropy rise) for a given change in flow direction [48]. In the limit, as the number of oblique shocks gets larger and larger, with each shock turning the flow through a smaller and smaller angle, the oblique shocks approach Mach waves[28] [48]. Therefore, a smooth turn will result in a continuous compression in the vicinity of the wall. However, the compression waves converge away from the wall and form a finite oblique shock wave with flow characteristics of those already discussed in section 3.2.1.

A comparison of abrupt compression and gradual compression can be seen in Figures 3-9 and 3-10. These figures will be used to conduct a simple example to evaluate and compare the final flow properties (M_f, T_f, P_f) as well as the entropy increases for one, two, and three flow deflections (θ's). For all cases, the properties at state 1 are $M_1 = 7$, $P_1 = 1000\ N/m^2$, $T_1 = 250\ K$ and the total deflection angle is $\theta = 12^\circ$. Application of Equations (3.13) through (3.21) for the given state 1 conditions along with the aide of Figures 3-9 and 3-10 lead to the results presented in Table 3-1.

[28] Mach waves are infinitesimal disturbances which combine to form shock waves or which individually are capable of producing expansions.

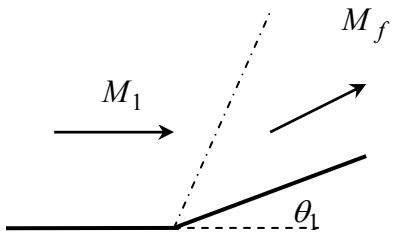

Figure 3-9. Abrupt compression of flow.

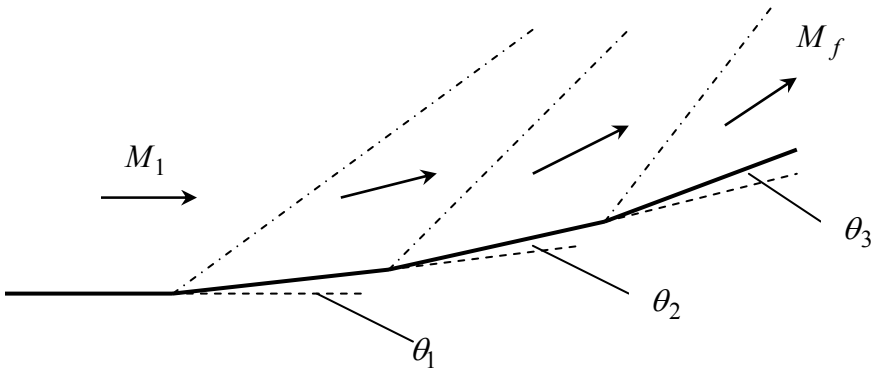

Figure 3-10. Gradual compression of flow.

It is quite evident from Table 3-1 that as the number of shock increase and the individual flow deflection angles decrease, the irreversibility (entropy increase) becomes considerably less. This consequently results in smaller total pressure losses described by Equation (3.22). It can also be seen that multiple weaker shocks produce a greater final Mach number and pressure and a slightly lower temperature.

Table 3-1. Gradual compression example results.

Case	θ_1	θ_2	θ_3	M_f	$T_f\ (K)$	$P_f\ (N/m^2)$	$s_{irr}\ (J/kg \cdot K)$
1	12	0	0	4.89	466.4	5530	136.1
2	6	6	0	5.13	431.2	5854	40.34
3	4	4	4	5.18	423.8	5943	18.68
4	4	2	6	5.17	426.2	5929	25.09

The results presented in Table 3-1 emphasize why designers of supersonic and hypersonic inlets would love to have the compression process carried out via isentropic compression waves. However, it is very difficult to achieve such a compression in real life because the contour of the compression surface must be quite precise and is only a point design

for the given upstream Mach number. Therefore, off-design Mach numbers will result in shocks for even the best-designed compression contour [3].

3.2.3 Prandtl Meyer Flow

In contrast to oblique shock waves as discussed in section 3.2.1, an expansion wave is formed when a supersonic flow is turned away from itself. The expansion wave is a two-dimensional mechanism that typically occurs during supersonic flow over a convex corner or at the exit of an under-expanded supersonic nozzle [48]. Figure 3-11 depicts an expansion fan emanating from a sharp convex corner. An expansion fan is simply a continuous expansion region which can be visualized as an infinite number of Mach waves (weak flow disturbances). Since the expansion occurs across a continuous succession of Mach waves, and since $ds = 0$ for each Mach wave, the expansion is isentropic [3]. Also, in contrast to the oblique shock wave, an expansion fan results in an increased flow velocity and a decrease in pressure and temperature after the expansion. However, it can be seen in Figure 3-11 that the supersonic flow is still turned through the local deflection angle θ.

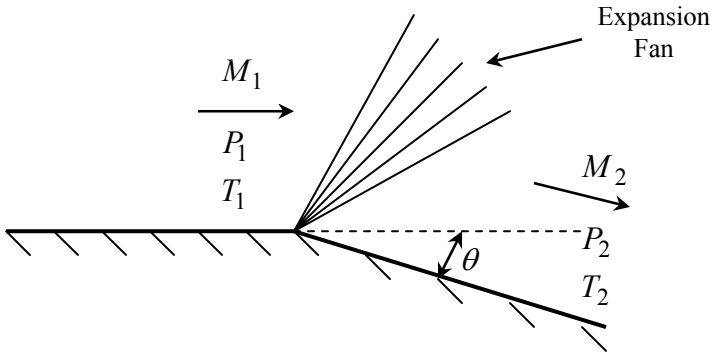

Figure 3-11. Prandtl-Meyer expansion.

Through a geometrical construction of the infinitesimal changes across an infinitesimally weak wave (in the limit, a Mach wave) and after substantial algebraic and trigonometric manipulation, the main relationships between flow deflection and Mach number can be determined and are given in Equations (3.23) and (3.24), namely,

$$\nu(M) = \sqrt{\frac{\gamma+1}{\gamma-1}}\tan^{-1}\sqrt{\frac{\gamma-1}{\gamma+1}\left(M^2-1\right)} - \tan^{-1}\sqrt{M^2-1} \tag{3.23}$$

$$\theta = \nu(M_2) - \nu(M_1) \tag{3.24}$$

Equation (3.23) is known as the *Prandtl-Meyer function*, and it represents the angle through which a stream, initially at Mach 1, must be expanded to reach a supersonic Mach number M [48]. It is the key to the calculation of changes across an expansion wave.

For a problem that requires the solution of the properties at state 2 from the known properties at state 1 and the known deflection angle θ as described in Figure 3-11, a straightforward analysis procedure is described as follows:

1. For the given M_1, calculate $\nu(M_1)$ from Equation (3.23)
2. Using the known θ and the value of $\nu(M_1)$ obtained in step 1, solve for $\nu(M_2)$ from Equation (3.24).
3. Obtain M_2 through iteration of Equation (3.23) or from tables provided.
4. Total pressure and temperature are constant across the expansion fan because of its isentropic definition. Therefore, using M_1 and M_2 the pressure and temperature ratios can be determined from

$$\frac{P_2}{P_1} = \left(\frac{1+\frac{\gamma-1}{2}M_1^2}{1+\frac{\gamma-1}{2}M_2^2}\right)^{\gamma/\gamma-1} \tag{3.25}$$

$$\frac{T_2}{T_1} = \frac{1+\frac{\gamma-1}{2}M_1^2}{1+\frac{\gamma-1}{2}M_2^2} \tag{3.26}$$

It is evident that, unlike the oblique shock ratios for pressure and temperature (Equations (3.19) and (3.20)), the normal components of the upstream and downstream are not needed for the expansion fan pressure and temperature ratio calculation.

A more detailed description of the derivation of Equations (3.23) and (3.24) along with extensive tables for the Prandtl-Meyer function can be found in [3, 48].

3.3 Hypersonic Vehicle and Component Description/Investigation

Before a rigorous discussion of the hypersonic vehicle system and component models is presented, a general discussion of the major hypersonic components along with synthesis/design and performance considerations is undertaken. A complete understanding of the geometrical configuration of the vehicle and components is essential to understanding the behavior of hypersonic airbreathing engines. This section attempts to provide a portrait of how hypersonic airbreathing engines operate and of present synthesis/design and performance issues.

It is important to be able to visualize the hypersonic vehicle engine flowpath to properly understand the distinction between the individual components. A generic representation of the scramjet propulsion system is, therefore, depicted in Figure 3-12. As seen in this figure and as mentioned in Chapter 1, the vehicle undersurface operates as the engine, i.e. thrust providing mechanism. Depending on individual preferences and designs, the propulsion system may consist of three to five separate sub-systems (the engine cowl is not a sub-system). The three main sub-systems are the inlet, combustor, and nozzle. The aircraft forebody can be either included as a propulsion component or be charged to the airframe sub-system (aerodynamics), a topic of detailed investigation [49-52]. This is attributed to the function of the forebody to provide pre-compression as well as an adequate amount of vehicle lift. The isolator is usually disregarded when performing an analysis solely on the scramjet operation of a hypersonic vehicle. However, it is a significant component of hypersonic vehicles that incorporate the dual-mode combustion system, i.e. both ramjet and scramjet operation. Although an isolator is not included in the system models of Chapter 4, a brief discussion of isolator performance is presented in this section.

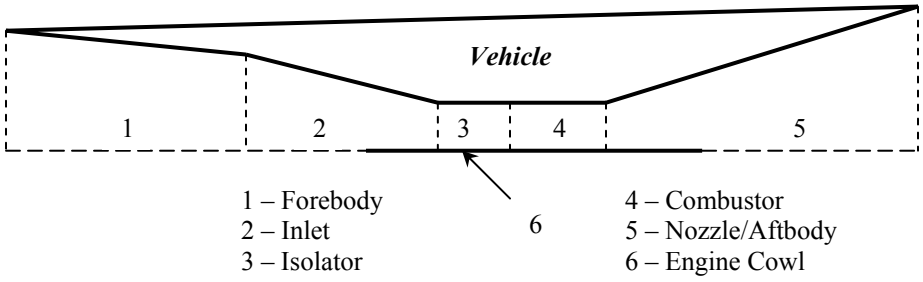

Figure 3-12. Generic propulsion sub-system terminology/components.

Efficient operation of the individual components and interactions among the components displayed in Figure 3-12 are crucial to overall scramjet propulsion system performance. The combination of forebody and inlet must efficiently compress the air to a suitable Mach number and pressure to allow for both auto-ignition and effective combustion of the fuel. The inlet must accomplish all of this all while providing uniform combustor entrance flow (as uniform as possible) and avoiding high static temperatures. Depending on injector location, non-uniform flow to the combustor may cause ignition problems. Excessive static temperatures can result in the onset of dissociation (see Figure 3-4), which significantly reduces the combustion heat release [21]. A lower static temperature can be generated while achieving a desired static pressure level by utilizing a more efficient compression process composed of mainly isentropic turning and weak shocks. In contrast, a compression via stronger shock waves is much less efficient and thus results in greater static temperatures. For a given static pressure, entering the combustor at a lower static temperature ultimately produces a lower combustion temperature and consequently less chemical dissociation occurs [21]. However, it should not go without saying that too low of a combustion temperature can have negative effects on the auto-ignition of the fuel. Any dissociation that may occur could, ideally, be recombined to recapture the dissociation energy by means of an equilibrium expansion process. Conversely, hypersonic vehicle synthesis/designs generally require rapid initial area expansion, producing a rapid decrease in static pressure freezing any chemical processes [21]. The dissociation energy is therefore lost from the propulsion cycle, and, thus, the net thrust is reduced [21].

3.3.1 Inlet Compression and Isolator Components

The goal in the design of any hypersonic inlet is to provide an efficient compression process, deliver nearly uniform flow and desirable static properties to the combustor, generate low drag, and provide these characteristics over a wide range of flight and engine operating conditions [21]. Due to the wide range of flight conditions to be encountered, the chosen configuration must simultaneously satisfy numerous interrelated and sometimes conflicting design requirements. The design of hypersonic inlets is greatly influenced and complicated by vehicle and flight constraints - i.e. mass capture and contraction limits, starting limits, boundary layer separation, and others.

Once again, a physical representation of some typical inlet geometries is imperative to understanding compression component analysis. Two common configurations are depicted in Figures 3-13 and 3-14. Figure 3-13 demonstrates an inlet compression system that is solely comprised of external oblique shock waves. The internal flow downstream of the final oblique shock is uniform and parallel to both the vehicle and engine cowl. A mixed external and internal oblique shock wave system, shown in Figure 3-14, is employed to achieve desired combinations of compression and flow turning. In contrast to external compression systems, mixed compression systems can result in configurations with the cowl parallel to the freestream flow and, generally speaking, allow a system of weaker shocks. An ideal compression system would be that of a continuously curved surface that results in infinitesimal compression waves (Section 3.2.2), culminating with isentropic pressure increase. Other configurations include inlet sidewalls and strut-like structures. A more detailed explanation of inlet configurations can be found in [1, 21].

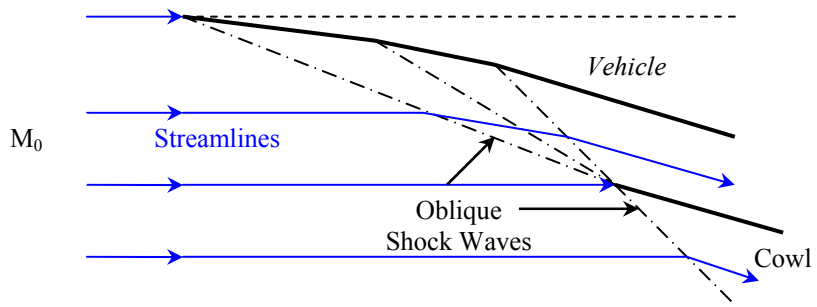

Figure 3-13. External oblique shock wave compression component.

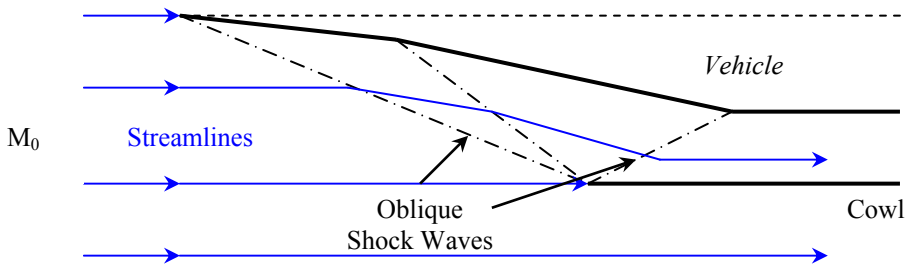

Figure 3-14. Mixed external and internal compression component.

It should be evident that understanding oblique shock characteristics is imperative because they provide the main mechanism for compression. An important design trait of a hypersonic inlet is the 'shock-on-lip' condition. As shown in Figures 3-13 and 3-14, the external oblique shock waves are 'focused' on and terminate at the lip of the engine cowl. This condition permits 100% mass capture, avoids flow spillage, and prevents shock ingestion. Shock ingestion could be detrimental to effective combustion and, thus, should be avoided at all costs. Flow spillage may be either beneficial or detrimental, depending on engine operating conditions.

Given that hypersonic engines operate over a large flight envelope, compression systems seldom operate at their synthesis/design point. Inlets operating at 'off-design' require means of controlling and tailoring oblique shocks to avoid unfavorable flow conditions. To some degree, this can be accomplished through a variable-geometry compression system. However, the large operating range inhibits its effectiveness. Therefore, additional means of controlling the inlet shock system are necessary, i.e. thermal energy exchange with flow, off-cowl energy deposition, or MHD[29].

Work by Moorhouse, Hoke, and Prendergast [6] demonstrated the use of a thermal energy exchange with the inlet flow in order to tailor the inlet shock position and maintain an inlet design Mach number under off-design conditions. This simplified methodology is employed in this thesis work (see Chapter 4) because it readily adaptable to one-dimensional analysis. The maintaining of an inlet design Mach number allows the satisfaction of the 'shock-on-lip' condition for fixed geometries over the entire flight range. However, the energy exchange may cause unsatisfactory changes to the freestream static pressure and temperature. This issue will be touched upon further in the individual component models of Chapter 4.

Extensive research has been performed on off-cowl local energy deposition and MHD sub-systems [53]. Local energy deposition in essence creates a heated region upstream and slightly below the cowl lip, thus, elevating the region's temperature and pressure. This results in inlet flow deflection and increased mass flow capture, creating a 'virtual cowl'. The possible mechanisms of energy addition are plasmas, laser or electron beams, microwave energy, etc. [53]. MHD generated power can also be used to create a 'virtual cowl' that would increase mass capture and possible engine thrust. One use of MHD generated power would be to extract

[29] Magnetohydrodynamics is the study of the interaction of a magnetic field and an electrically conducting fluid. It can be also defined as the study of plasma motion and dynamics in the presence of a magnetic field.

energy from high temperature regions downstream of the combustor and add that energy upstream of the inlet to optimize inlet performance [53]. These methods of shock system control are far from trivial and are practically impossible to model in a one-dimensional analysis. Therefore, even though energy addition/subtraction for creating the virtual cowl are used in this thesis work, the methods used to practically achieve this are not considered.

Mass Flow Capture

Inlet mass flow capture is vital to engine operation and overall hypersonic vehicle performance. As previously stated, 100 % mass flow capture occurs at the 'shock-on-lip' condition. When inlets shocks stand out in front of the cowl lip, mass flow escapes under the cowl and the engine is not operating at 100 % mass flow capture. This phenomenon, known as *spillage*, is demonstrated in the inlet of Figure 3-15. Spillage is defined as the difference between the airflow that could pass through the area obtained by projecting the end point of the cowl lip axially to the freestream flow, referred to as A_1, and the throughflow area of the freestream flow A_0 that actually enters the physical opening [19]. The spillage in Figure 3-15 is therefore $A_1 - A_0$.

At large hypersonic flight altitudes where the density is quite low, mass flow spillage may be highly undesirable. Mass flow spillage may also be undesirable during hypersonic acceleration where thrust requirements are rather large. Higher density, lower flight altitudes may require some spillage, but it does not go without a penalty. Mass flow spillage results in additional drag around the spillage area and, therefore, higher than necessary equivalence ratios[30] may be required in the combustor in order to produce the extra thrust to compensate for the drag.

Accurately predicting and calculating mass flow spillage in the context of one-dimensional analysis can be difficult. Consequently, the modeling done in this thesis work aims at maintaining the 'shock-on-lip' condition at all flight conditions for 100 % mass flow capture and is done so via means described in the individual component models of Chapter 4.

[30] The equivalence ratio is defined as the ratio of the actual fuel-to-air ratio to the stoichiometric fuel-to-air ratio. It is commonly used to indicate quantitatively whether a fuel-oxidizer mixture is rich, lean, or stoichiometric.

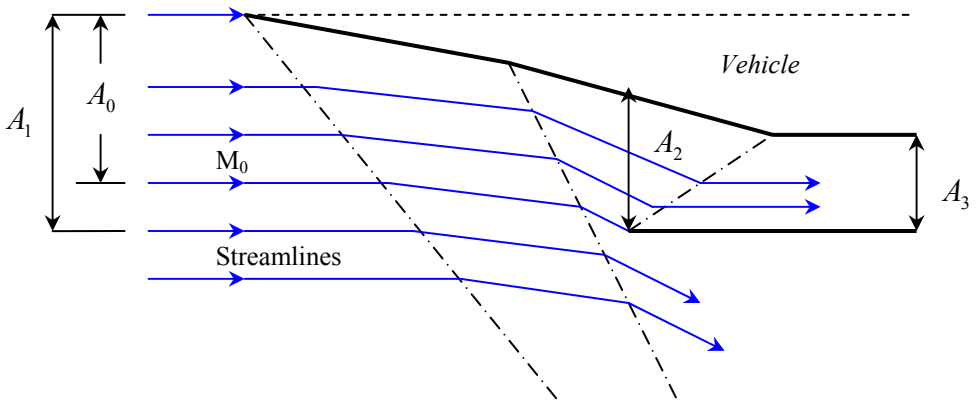

Figure 3-15. Mass flow spillage and area definitions.

Inlet Flow Starting and Contraction Limits

Scramjet inlets must operate in started mode for proper operation of the vehicle. Starting limits refer to the degree of acceptable internal contraction that an inlet may possess to ensure that the flow phenomena in the internal portion of the inlet do not alter the capture characteristics of the inlet. An inlet will self-start at a certain internal contraction depending upon the freestream conditions and the inlet geometry. With use of Figure 3-15, the inlet internal contraction ratio is defined as A_2/A_3 where A_2 is the area between the vehicle undersurface and the cowl lip and A_3 is the area at the inlet throat. Preliminary estimates of the internal contraction ratio that will self-start can be approximated by the Kantrowitz limit given by [21].

$$\left(\frac{A_2}{A_3}\right)_{Kantrowitz} = \frac{1}{M_2}\left(\frac{(\gamma+1)M_2^2}{(\gamma-1)M_2^2+2}\right)^{\frac{\gamma}{\gamma-1}}\left(\frac{\gamma+1}{2\gamma M_2^2-(\gamma-1)}\right)^{\frac{1}{\gamma-1}}\left(\frac{1+\gamma-\frac{1}{2}M_2^2}{\gamma+\frac{1}{2}}\right)^{\frac{\gamma+1}{2(\gamma-1)}} \quad (3.27)$$

M_2 here is the Mach number of the inlet flow where internal contraction begins. Although not immediately evident from Equation (3-27), the allowable starting contraction ratio increases as Mach number increases. Experimental data suggest that the Kantrowitz limit becomes conservative at higher Mach numbers and internal contraction ratios as high as 2 to 3 can be tolerated [21].

An inlet can be unstarted either by overcontracting to the point where the flow chokes at the inlet throat, having sufficiently distorted flow at the inlet face, or by raising the back pressure

beyond the level that can be sustained by the inlet [21]. When inlet unstart occurs, boundary layer separation may occur, creating undesirable flow characteristics. Mass flow spillage may also occur, depriving the engine of the airflow necessary for thrust. Finally, fuel control systems may be unable to properly adjust to the rapidly changing combustor entrance conditions [1]. For these reasons, inlet unstart must be avoided by any means necessary.

Since overcontraction is an area of concern, correlations for maximum contraction ratios have been developed via experimental analysis. The contraction ratio is defined as, with the aid of Figure 3-15, the ratio of freestream capture area to the inlet throat area, A_0/A_3. An empirical fit to experimental data is given in [21] as

$$\frac{A_3}{A_0} = 0.05 - \frac{0.52}{M_0} + \frac{3.65}{M_0^2} \tag{3.28}$$

and is applicable to the Mach number range of $2.5 < M_0 < 10$. Non-uniform flowfields at the inlet throat have an affect on the maximum contraction ratio; and, thus, the inlet throat profile should be as uniform as possible to operate at high contraction ratios.

Boundary Layer Friction and Separation

The development of the boundary layer within an inlet substantially affects the overall performance and operability of the inlet at hypersonic speeds [21]. The boundary layer serves as an additional compression mechanism of the captured flow, along with oblique shocks and area change. Issues briefly addressed are that of boundary layer friction and separation.

Friction within the boundary layer provides viscous dissipation of the flow and, therefore, a loss mechanism with which it must be reckoned. However, rigorous modeling within the framework of one-dimensional flow cannot be done. Heiser and Pratt [1] employs a method of separating out the oblique shock wave system analysis from the frictional analysis and a method somewhat similar to that is used in the system models of Chapter 4. Experimental studies have shown that viscous compression at leading edges is appreciable at hypersonic speeds. However, it is not as significant as the other mechanisms previously discussed [21].

Boundary layers are subjected to high adverse pressure gradients due to the desire to compress the captured air in a relatively short length. These adverse pressure gradients adjacent to the vehicle surfaces, stemming from oblique shock waves, may cause separation, depending

on shock and boundary layer strength. The main mechanism for separation is that the cumulative upstream viscous forces have dissipated the momentum necessary for the boundary layer to overcome the imposed pressure rise [1]. Boundary layers more than likely will reattach with the consequence of a region of reversed and recirculating flow and a zone of high heat transfer near the reattachment point. Turbulent boundary layers can sustain much larger pressure gradients and are, therefore, more resistant to separation than laminar boundary layers. Turbulent boundary layers, unfortunately, increase frictional losses and heat transfer. Therefore, it is highly desirable to design an inlet knowing where boundary layer transition will occur.

An increase in drag, much stronger than skin friction drag, is another consequence of separation. The separated region is unstable with large distortion which can lead to flow blockage and uncertainty downstream of the separation. These undesirable characteristics of separated flow are just a few reasons why boundary layer separation should be avoided on hypersonic vehicles.

Inlet Isolator

Isolators are needed during the low Mach number (ramjet mode) portion of the flight regime where subsonic combustion is expected. Isolators are usually constant area ducts that contain a shock train (normal or oblique) to provide a mechanism for a supersonic flow to slow to subsonic speeds and adjust to a static back pressure higher than its inlet static pressure. They also contain the high pressure produced by the large pressure rise in the subsonic combustor and prevent inlet unstart. Shock trains in constant area ducts have the characteristic that the maximum static pressure rise they can generate is exactly the same as that which would exist behind a normal shock wave at the inlet throat [1]. The synthesis/design and operation of a dual-mode scramjet requires an isolator at low speeds without penalizing scramjet performance at hypersonic speeds.

Inlet Constraints and Performance Measures

In addition to being able to address the wide array of synthesis/design issues, the hypersonic vehicle inlet is subject to constraints for proper operation of the scramjet engine. The main constraints imposed on the inlet are restrictions on the flow static conditions at the inlet exit/combustor entrance. Suitable pressures and temperatures are necessary for auto-ignition of the fuel in the combustor and to provide reasonable combustion reaction rates. If the pressure

and temperature are too low, the length of the combustor required to complete the reaction and consume the available fuel will be excessive. Curran and Murphy [21] and Heiser and Pratt [1] suggest a commonly applied rule of thumb of 0.5 atm. for the minimum pressure and 10 atm. for the maximum at the inlet exit/combustor entrance interface. However, it is highly unlikely that inlet exit pressures will ever be anywhere near the maximum allowed value because compression to rather high pressures would almost certainly cause the inlet flow to go subsonic. These same researchers state that a minimum temperature of 1100 K must be provided by the inlet to ensure auto-ignition and a maximum of approximately 1700 K to prevent excessive dissociation in the exhaust flow. Other literature references [41, 54] assert pressures between 0.25 – 1 atm. and temperatures in the range of 1000 to 2000 K must be provided to the combustor by the inlet compression system. Other constraints are the starting and contraction limits already discussed and flow turning restrictions to prevent boundary layer separation.

There are an abundance of parameters that have been formulated for the quantitative evaluation of compression component performance, each with its own rational. Three of the more accepted and more widely applied of these in hypersonic compression systems are total pressure ratio, kinetic energy efficiency, and adiabatic compression efficiency which are expressed as

$$\pi_c = \frac{P_{t_3}}{P_{t_0}} = \frac{P_3}{P_0}\left(\frac{1+\frac{\gamma-1}{2}M_3^2}{1+\frac{\gamma-1}{2}M_0^2}\right)^{\frac{\gamma}{\gamma-1}} \tag{3.29}$$

$$\eta_{KE} = \frac{V_{ideal\,\exp}^2}{V_0^2} \tag{3.30}$$

$$\eta_c = 1 - \frac{(\gamma-1)}{2}M_0^2\left(\frac{1-\eta_{KE}}{\psi-1}\right) \tag{3.31}$$

The total pressure ratio is defined as the ratio of the total pressure at the entrance to the combustor divided by the total pressure of the freestream flow. The kinetic energy efficiency is defined as the ratio of the square of the velocity that the compression system exit flow would achieve if it were isentropically expanded to the freestream static pressure to the square of the

freestream velocity [1]. Kinetic energy efficiency is a direct measure of the preservation of kinetic energy, the most important quantity in scramjet propulsion for thrust production. The kinetic energy efficiency is near 1 at most large Mach numbers; therefore, at least three significant figures are needed to insure acceptable accuracy. Finally, it is shown in Equation (3.31) that the adiabatic compression efficiency is a function of the flight Mach number, kinetic energy efficiency, and ψ, which is the inlet static temperature ratio.

3.3.2 Combustion Component

The development of a hypersonic vehicle utilizing air-breathing engines suggests the injection and burning of hydrogen fuel in a supersonic airstream and a thorough understanding of the means by which this can be accomplished. Supersonic combustion is preferred at increased Mach numbers because higher levels of performance can be attained. The primary function of the combustor is to burn the fuel in order to release energy to the flow, which can then be expanded via the nozzle to produce vehicle thrust. The combustion of the fuel may take place in constant area ducts or ducts with some area relief (divergent sections) to prevent the thermal choking of the flow. The effects of reaction and heat release from combustion at greater hypersonic Mach numbers are less pronounced than at lower hypersonic Mach numbers. The energy from heat release may be only a relatively small portion of the total enthalpy of the working fluid at higher hypersonic Mach numbers whereas at lower hypersonic Mach numbers the kinetic energy of the air and the potential combustion heat release are roughly equal [21].

Large heat loads occur in the combustor at hypersonic velocities; and, therefore, a thermally balanced combustor is required to avoid material limits. The main mechanism used for combustor wall cooling is to circulate fuel behind the walls and allow the fuel to act as a heat sink. Thus, fuel injection characteristics are directly determined by system cooling requirements. Allowing the coolant to be raised to its highest possible temperature without avoiding material limits makes best use of each unit of coolant. The more thermal energy each unit of fuel used as coolant can absorb, the less likelihood of having to 'waste' fuel because the equivalence ratio exceeds 1 [1]. One benefit of using hydrogen as the fuel is that hydrogen is far superior as an engine coolant to typical hydrocarbon fuels because of its ability to absorb more energy per unit mass. Another benefit is that hydrogen's large energy release per unit mass, $119{,}954\ kJ/kg$, offers the potential of flight to freestream Mach numbers of 15 and beyond. There are a few

disadvantages of using hydrogen as a fuel as well. The low density of liquid hydrogen requires large storage tanks and storage of liquid hydrogen is accomplished through cryogenic systems that are often costly and quite complex.

The combustion component tends to be the one in the hypersonic vehicle with the largest destruction exergy, i.e. flow losses. Consequently, combustion system synthesis/design has the greatest impact on vehicle performance over the vehicle's operating range. Flow losses occurring in the combustor arise from fuel-air mixing, non-equilibrium chemical kinetics, injector and wall drag, and heat transfer across a finite temperature difference. Accurate methods of predicting these losses and their individual effect on hypersonic propulsion and thrust production are of the utmost importance.

Optimal combustor synthesis/designs are based, as a minimum, on the engine thrust potential [21]. The concept of thrust potential was presented and more thoroughly discussed earlier in Section 2.2.1. Briefly, thrust potential is the thrust generated by an ideal expansion of combustor exit conditions. It is often non-dimensionalized by an ideal thrust to form an effectiveness parameter which in turn can be used for engine analysis and synthesis/design. For example, the effectiveness parameter can be implemented to compare competing fuel injection concepts or to determine optimal combustor lengths.

Fuel Injection and Fuel-Air Mixing

The efficiency and effectiveness of fuel injection to a large degree determines the net heat release achieved in scramjet combustion [21]. The extent of fuel-air mixing achieved reflects the efficiency while a more effective injection strategy translates into a greater thrust potential, i.e. a minimization of combustor exit streamthrust losses incurred during mixing. The combustion efficiency is critically related to the degree of fuel-air mixing and ultimately the feasibility of hypersonic propulsion. Therefore, it is advantageous to understand some fundamental implications of the various fuel injection strategies and their associated benefits and disadvantages.

A wide array of fuel injection strategies have been proposed and examined throughout the literature [1, 21, 55-57]. A few of these strategies have also been studied to predict mixing efficiency and the losses associated with mixing and their inherent affect on thrust potential [56, 57]. A few injection/mixing techniques are parallel stream mixing, normal fuel injection via wall jets, and in-stream injectors (e.g., angled ramp injectors).

The mixing of air and fuel in parallel streams is one injection technique proposed for scramjet engines. The fuel and air velocities can either be equal or of different magnitude. If the velocities are equal there is no lateral transport of momentum and only a lateral transport of mass due to molecular diffusion. Unequal velocities in the two streams produce mass transfer through diffusion and lateral momentum transfer from the faster to the slower stream, resulting in a shear and mixing layer. Although parallel injection is beneficial in terms of fuel momentum addition, it results in non-efficient mixing and unreasonably long combustor lengths. A further increase in the velocity difference between the two streams can reduce convective times and axial distance required for mixing to be completed [1]. However, detrimental consequences such as increased drag and viscous dissipation are more than likely to occur. In the end, shear layer mixing (parallel streams) cannot meet the stoichiometric requirements for optimal combustion [1].

Mixing with normal fuel injection by means of wall jets is another technique investigated for scramjet propulsion. Normal injection minimizes intrusion in the combustor flowpath and increases local mixing of fuel and air but, unfortunately, creates a relatively complex flow structure in the vicinity of the jets. A detached normal shock wave forms just upstream of the jet and, as a result, leads to boundary layer separation [1]. Inherently, total pressure losses arise from the normal shock wave and boundary layer separation which lead to a decrease in overall cycle efficiency. Normal injection reduces the mixing transition distance, i.e. 'jump-starts' the mixing, and causes a greater initial growth of the mixing efficiency but weakens the far-field mixing characteristics in such a way that approximately the same length combustor is required for complete mixing as with the parallel configuration [1]. An increase in efficiency may possibly be realized through an optimization of wall jet injection angle and jet spacing.

A final injection strategy examined is in-stream injection, usually[31] through axial vortex mixers termed hypermixers. The design objective of these devices is to create axial vortices[32] to sweep through and entrain the central fuel jet, successfully leading to enhanced near-field and downstream mixing and lower total pressure losses. Fairly recent research has shown that the addition of streamwise (axial) vorticity in supersonic flow can increase mixing rates, as much as sixty percent [1]. One typical type of hypermixer is that of wall-mounted inclined ramps aligned with the flow, i.e. injectors pointing downstream. These configurations make use of an oblique

[31] Other in-stream injection techniques have been investigated such as strut-like injectors with configurations similar to the wing/airfoil geometry of conventional aircraft.
[32] This is in opposition to lateral vortices, which are the predominant vortex structures found in parallel and normal fuel injection.

shock or expansion fan to produce the necessary axial vorticity. A significant increase in the near-field, fuel-air mixing and combustion has been shown in a study comparing near-field mixing for a parallel-injected jet with and without passage of the jet through an oblique shock [1]. Although there may be a gain in mixing enhancement, it should not be overlooked that an additional total pressure loss occurs due to the oblique shock.

After examination of the various mixing strategies, it should be apparent that shear layers created by parallel injected streams and the use of lateral vortices cannot sufficiently achieve near-field mixing to required stoichiometric proportions of air and hydrogen. However, valuable insights and concepts have been clarified that may be utilized in future work.

Dual-Mode Combustion Component

As noted in Chapter 1 of this thesis, sustained flight over a large range of Mach numbers requires hypersonic vehicles to be able provide subsonic combustion for flight Mach numbers less than about 5, and supersonic combustion for flight Mach numbers greater than about 6 or 7. For this to be achieved and to avoid having to carry two different engines, it is desirable to have subsonic flow, when necessary, in the combustor without area constrictions either upstream or downstream of the burner[33] as required by a purely ramjet engine. Heiser and Pratt [1] credits E.T. Curran and F.D. Stull with developing the concept of a *dual-mode combustion system* in which both subsonic and supersonic combustion can be made to occur within the same scramjet engine geometry.

When operating in ramjet mode, the flow is made subsonic at the combustor entrance by means of the isolator, which has already been described in Section 3.3.1. Instead of two physical throats, a choked[34] thermal throat is provided by the dual-mode combustor which thereby chokes the flow and fixes a large burner entry back pressure [1]. This back pressure produces a normal shock train to form in the isolator and, therefore, results in subsonic flow delivered to the combustor. The choked thermal throat is brought about by choosing the right combinations of area distribution, fuel-air mixing, and combustion [1]. This thermal throat also allows the subsonic flow to be accelerated to supersonic velocities.

Since in scramjet mode the desired flow is to be supersonic at the combustor entrance, there is no apparent need for an inlet isolator. Even though the flow anywhere within the engine

[33] Burner and combustor are used synonymously throughout this discussion.
[34] Choked refers to conditions in the flow where the Mach number equals one, M = 1.

is *ideally* neither choked nor subsonic, if the area increase in the burner is not sufficient to relieve the thermal occlusion resulting from heat addition to a supersonic stream, an adverse pressure gradient arises [1]. Boundary layer separation may occur as a result of these pressure gradients which allow the pressure rise to propagate upstream and, if not contained, cause engine unstart. This phenomenon can be contained once again through the isolator.

Transition between these two operating modes (ramjet and scramjet) adds further complexities to the design of dual-mode combustion systems. General one-dimensional analysis of dual-mode systems has led to the conclusion that a constant area combustor in conjunction with a constant area isolator is not a good combination for these configurations [1]. Instead, a burner with some area relief (increasing area) coupled with a constant area isolator provides the means to allow a useful operating range for mode transition [1].

3.3.3 Expansion Component

The expansion component, i.e. the nozzle, functions to expand the high pressure and high temperature gas mixture exiting from the combustor to local atmospheric pressure and accelerate the flow to high exit velocities to generate thrust[35]. Potential energy is converted to kinetic energy during the expansion process and the shape of the expansion component determines the angle of the gross thrust vector relative to the vehicle's flight direction. Two important factors of hypersonic nozzle design are efficient generation of thrust and the aerodynamic stability of the vehicle. These issues are significant because the nozzle 'works' on the total flow through the engine and the high surface pressure forces and thrust direction encompass a substantial portion of vehicle trim [21].

Performance of the expansion component is influenced by the loss mechanisms occurring in the component. The main loss mechanisms found in expansion components are skin friction, heat loss, failure to recombine dissociated species, and flow divergence and under-expansion losses. The most complex loss mechanisms are dissociation losses, which result from the flow freezing in the rapid expansion process and consequently prevent energy addition by the recombination of free radicals produced by the combustion process [21]. Dissociation tends to be more prevalent at higher Mach number flight where combustor exit static temperatures are usually higher. Therefore, it is easy to see that dissociation losses are directly related to the

[35] Moreover, it functions to capitalize on the thrust potential of the flow leaving the combustor.

efficiency of the compression component. Skin friction and heat transfer are much larger in the first half of the nozzle, therefore, it would be beneficial to form laminar flow within this region to reduce both of these losses. Flow divergence losses are a result of the streamlines at the nozzle exit being at different angles relative to the flight path and under-expansion losses arise by not expanding the flow to ambient pressure. Nozzle performance can be very sensitive to both of these last two design consideration [21].

One typical measure of nozzle performance is the gross thrust coefficient, sometimes referred to as CFG. It is defined as the actual gross thrust of the stream tube at the exit plane of the nozzle divided by the equilibrium ideal thrust of the flow-path stream tube expanded to the local atmospheric pressure [1, 21]. A well-designed nozzle would have a gross thrust coefficient of about 0.96, with a practical upper limit of about 0.97 [21]. Other performance measures are the total pressure ratio, Equation (3.29), as well as a parameter similar to the kinetic energy efficiency termed the velocity coefficient. The velocity coefficient is simply the ratio of the actual average total velocity at the exit of the expansion sub-system to the ideal total velocity [1].

Due to the tight integration of the airframe and engine, hypersonic vehicles synthesis/designs use two-dimensional expansion as opposed to axisymmetric or circular expansion. A reason for this is because circular nozzles are comparatively heavy and are not easily adaptable to variable geometry [1]. Also typical of hypersonic scramjet engines, optimal exhaust areas are approximately 1.5 to 2.0 times the freestream engine capture areas [21]. A final nozzle design constraint is that the initial nozzle expansion is limited to a maximum value of somewhere around 18 degrees [58-60].

Although expansion components are simpler than other vehicle components in the sense that the number of synthesis/design requirements to be met are fewer, their performance throughout the entire flight regime is very important to overall vehicle system performance.

Chapter 4

Comprehensive Sub-system and Component Models

Realistic component models are necessary to adequately describe the flow physics and predict the performance of a hypersonic vehicle over a rather large range of operating conditions. Therefore, an appreciable amount of time was dedicated to developing and validating the individual component models presented in detail in this chapter. A variety of analysis techniques were utilized throughout the model development, ranging from simple geometric relations to oblique shock and Prandtl Meyer expansion theories to more advanced differential 'marching' schemes. The objective of this chapter is to provide a rather rigorous description of the hypersonic vehicle systems and sub-systems and the equations governing the analysis.

4.1 Propulsion Sub-system Description

The propulsion sub-system of a hypersonic vehicle, as noted in Chapter 3, is comprised of three main components; specifically the inlet, combustor, and nozzle. This analysis excludes an isolator model because the hypersonic vehicle undergoes supersonic combustion at all operating conditions, i.e. ramjet operation omitted. The propulsion sub-system components are presented in the manner in which flow proceeds through the engine. A sufficient number of figures are included to provide a more detailed physical representation of components, analysis methods, etc. and to supplement the discussion that follows.

4.1.1 Inlet Component Description and Modeling

A mixed external and internal compression component is implemented to model the inlet component. The main mechanism for compression, as noted in Chapter 3, is a direct result of the oblique shocks produced from flow turning. Skin friction drag is included on the vehicle inlet

surfaces and, therefore, provides an additional compression mechanism (although much less significant than the oblique shocks). The reduction of the flow area from inlet entrance to exit offers a final means of compression.

A detailed physical representation of the inlet component is displayed in Figure 4-1. The inlet is comprised of two compression ramps, each of which generates an oblique shock as a result of flow deflection. An additional oblique shock originates at the cowl leading edge and is canceled at the inlet throat expansion corner to provide uniform flow parallel to the combustor. The oblique shock wave emanating from the vehicle nose and the entire forebody are not considered part of the inlet sub-system in this analysis and are charged to the aerodynamic system (see section 4.3.2). The forebody and its associated oblique shock are displayed as well, because they inherently affect the inlet entrance flow characteristics. The inlet, and therefore, its geometrical configuration, is designed on the premise that the 'shock-on-lip' condition is to be satisfied at all flight conditions.

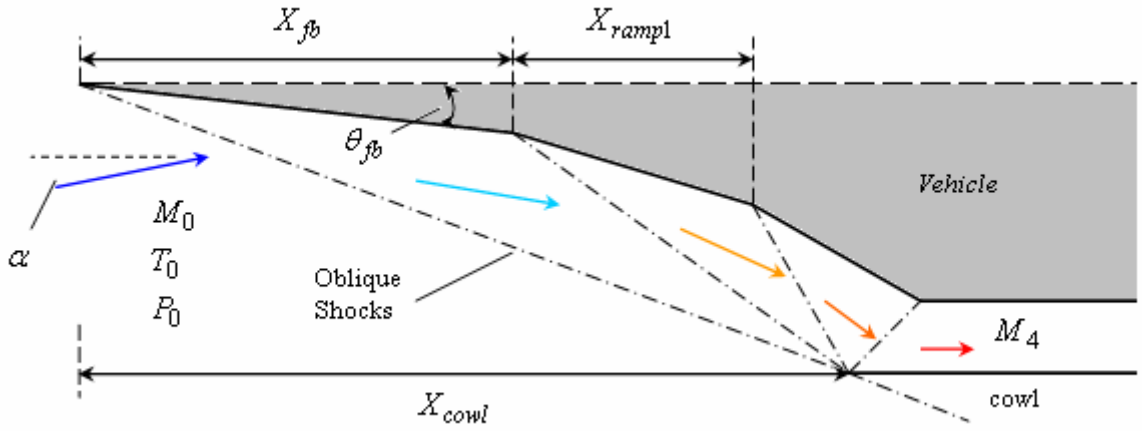

Figure 4-1. A physical representation of the inlet component (front undersurface of the vehicle). The decision and operational variables that govern the flow characteristics throughout the inlet are displayed along with the flow velocity vector from freestream to inlet exit.

Also shown in Figure 4-1 are the four design decision variables and one operational[36] decision variable which are associated with the inlet component. Knowledge of these five variables allows for a complete generation of the front undersurface geometrical configuration of the vehicle as well as a comprehensive description of flow properties throughout the inlet. The

[36] An operational decision variable is varied throughout the range of operation of the vehicle, i.e. varied over the different mission segments.

four design decision variables are: forebody axial length (X_{fb}), first-ramp axial length (X_{ramp1}), axial location of the cowl lip from the front of the vehicle (X_{cowl}), and forebody deflection angle (θ_{fb}). The sole operational decision variable is the angle-of-attack (α) which influences the initial forebody compression, i.e. it is necessary for determination of the forebody oblique shock angle.

From this point forward the freestream will be termed station '0', the inlet entrance interface will be termed station '1', and the inlet exit interface will be termed station '4'. These stations can be seen by referring to Figures 4-2. Also presented in this figure are the three relevant flow areas encountered in the inlet. The term A_{total} represents, with the shock on lip, the total capture area of freestream flow and also the location of the engine cowl from the reference line[37]. The area where internal compression begins is signified by A_{ic} and the symbol A_{throat} represents the inlet throat[38] area. An example of what is referred to as a ramp (or forebody) height (h_{ramp1}) is given as well in Figure 4-2 because it will be referred to in the solution procedure description.

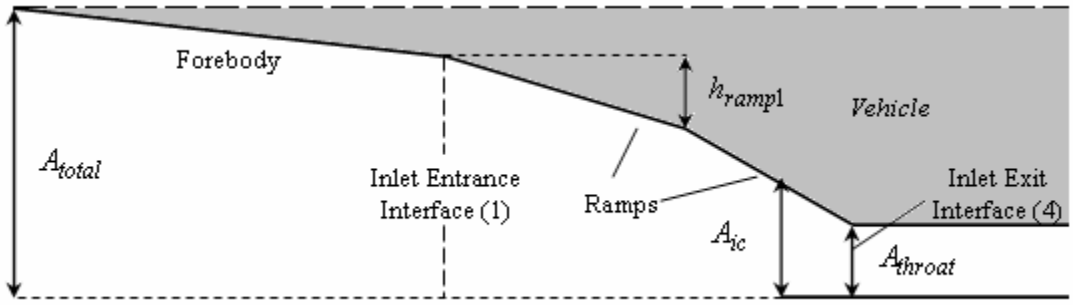

Figure 4-2. Inlet interface and vehicle surface definitions along with some basic area and height representations.

The total vehicle contraction ratio and the inlet contraction ratio are given by Equations (4.1) and (4.2), respectively. As mentioned in Section 3.3.1 of this thesis, theoretical and

[37] The reference line is the line which separates the upper surface of the vehicle from the lower surface of the vehicle.
[38] The throat area is the minimum flow path area encountered in the propulsion system. It also equals the combustor area if the combustor is non-divergent.

experimental limits have been developed for the minimum internal contraction ratio needed for inlet self-starting and the maximum allowable contraction ratio.

$$CR = A_{total} / A_{throat} \tag{4.1}$$

$$ICR = A_{ic} / A_{throat} \tag{4.2}$$

The height of the first inlet ramp, for example, can be calculated as follows

$$h_{ramp1} = X_{ramp1} \tan\left(\theta_{fb} + \theta_{ramp1}\right) \tag{4.3}$$

where it needs to be emphasized that, for successive inclination angles, the following angle is measured from the previous angle.

Inlet Solution Procedure

The solution procedure taken to provide a complete description of the flow properties throughout the inlet and allow for the calculation of the front undersurface geometry and other necessary parameters is a relatively straightforward process. The solution procedure for the oblique shock wave system and geometry calculation is described first and then the method for incorporating skin friction into the inlet component is presented.

The steps taken to solve the oblique shock wave system and its associated geometry for the hypersonic vehicle at 'on design' conditions are as follows:

1. With knowledge of the freestream properties $\left(M_0, T_0, P_0, u_0\right), \alpha$, and θ_{fb}, calculate the forebody oblique shock angle, β_{fb}, the flow properties downstream of the shock[39], and the
   irreversiblility associated with the shock process using Equations (3.13)-(3.21).
2. Calculate the total capture area, A_{total}, from the relationship

   $$A_{total} = X_{cowl} \tan\left(\beta_{fb} - \alpha\right) \tag{4.4}$$

   and then the captured mass flow rate is easily computed.

[39] The flow properties downstream of the forebody oblique shock wave are those of the physical inlet entrance.

3. Determine the height of the forebody, h_{fb}, from Equation (4.3) with the variables X_{fb} and θ_{fb}.

4. The oblique shock angle emanating from the first inlet ramp can now be obtained from basic geometry

$$\beta_1 = \tan^{-1}\left(\frac{A_{total} - h_{fb}}{X_{cowl} - X_{fb}}\right) - \theta_{fb} \tag{4.5}$$

and the corresponding first inlet ramp angle, θ_1, is produced by direct application of Equation (3.17).

5. Once again, calculate the downstream properties and the irreversibility associated with the shock using Equations (3.13)-(3.21).

6. Repeat step 3 to determine the height of the first inlet ramp.

7. Repeat steps 4 and 5 for the second inlet ramp and then step 3 for the second inlet ramp as well.

8. With knowledge of the forebody deflection angle, both inlet ramp angles, and the Mach number just upstream of the cowl shock, the cowl shock angle needed to produce/return parallel flow to the combustor, β_3, is calculated from Equation (3.17).

9. Two separate expressions can be written for A_{throat} and to ensure that the shock emanating from the cowl lip is canceled at the expansion corner, the expressions must be set equal to one another. The second inlet ramp axial length that satisfies this condition is

$$X_{ramp2} = \frac{A_{throat} - h_{fb} - h_{ramp1} - \left(X_{fb} + X_{ramp1} - X_{cowl}\right)\tan\delta_3}{\tan\delta_3 + \tan\left(\theta_{fb} + \theta_1 + \theta_2\right)} \tag{4.6}$$

where the angle δ_3 is defined in Figure 4-3.

10. Step 3 is used to find the second ramp height and steps 4 and 5 are repeated for the cowl oblique shock. The throat area is calculated by subtracting the forebody and ramp heights from the total capture area. The total inlet length is calculated by summing the forebody axial length with the two ramp axial lengths.

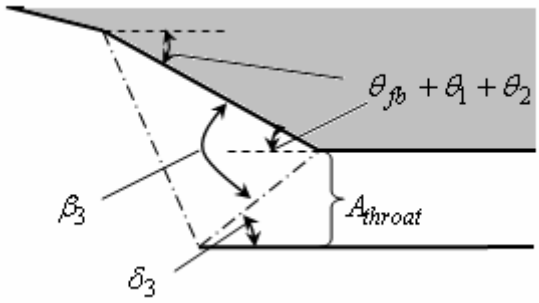

Figure 4-3. Close up view of the cowl oblique shock and inlet throat region.

11. With a complete description of the flow properties throughout the inlet as well as the inlet configuration now known, the positive vertical (y-direction) pressure forces on both inlet ramps and the negative vertical pressure force on the inside of the cowl extending into the inlet can be calculated. These pressure forces along with their corresponding location of action (assumed to be center of each segment) are passed on to the aerodynamic program.

These 11 steps were developed to provide the most straightforward method (for the work in this thesis) for solving the oblique shock system and are by no means the only, or for that matter the best, method to design an inlet or solve the shock system.

Skin friction affects on compression are predicted using a method similar to that described in Section 3.3.1 where the oblique shock system is separated out from the friction analysis. The method used to capture skin friction affects in this inlet model was suggested by Riggins [58]. A conceptual diffuser[40] of contraction ratio A_1 / A_{throat} and surface area equal to the inlet surface area (length of both inlet ramps) is employed in conjunction with the flow properties at the inlet entrance (station 1) to determine the rate of irreversibility produced by the friction, $\dot{S}_{irr_{frict}}$ (see Figure 4-4). The diffuser, using a differential 'marching' scheme[41], solves the following equations provided by Shapiro [43]

[40] A conceptual (i.e. imaginary) diffuser is used in this analysis as a means to separate out the frictional affects on the flow from the oblique shock system affects on the flow.
[41] A step by step evaluation of the governing equations, i.e. an explicit solution procedure.

$$\frac{dM}{M_x} = -\frac{\left(1+\frac{\gamma-1}{2}M_x^2\right)}{1-M_x^2}\frac{dA}{A_x} + \frac{\gamma M_x^2\left(1+\frac{\gamma-1}{2}M_x^2\right)}{1-M_x^2}\frac{2C_f\,dA_{surf}}{A_x} \tag{4.7}$$

$$\frac{dT}{T_x} = \frac{1}{1-M_x^2}\frac{dA}{A_x} - \frac{\gamma(\gamma-1)M_x^4}{2\left(1-M_x^2\right)}\frac{4C_f\,dA_{surf}}{A_x} \tag{4.8}$$

$$\frac{dP}{P_x} = \frac{\gamma M_x^2}{1-M_x^2}\frac{dA}{A_x} - \frac{\gamma M_x^2\left[1+(\gamma-1)M_x^2\right]}{2\left(1-M_x^2\right)}\frac{4C_f\,dA_{surf}}{A_x} \tag{4.9}$$

$$\frac{ds}{c_p} = \frac{dT}{T_x} - \frac{\gamma-1}{\gamma}\frac{dP}{P_x} \tag{4.10}$$

The friction irreversibility value along with the properties exiting the inlet exit interface (station 4) is then passed to a separate solver to produce the flow properties at the entrance to the combustor, station '5'. To clarify this statement, station 4 is the actual *physical* exit of the inlet component. Station 5 coincides with this physical location, however, the properties at station 5 are 'adjusted' (using the known rate of irreversibility produced from friction) from the properties at station 4 to reflect the affects of friction on the inlet flow. A depiction of the diffuser and the solver are presented in Figures 4-4 and 4-5 to supplement the discussion.

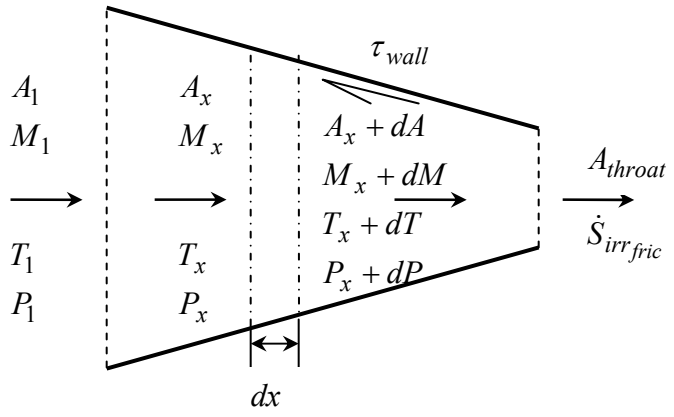

Figure 4-4. Conceptual diffuser used to approximate the irreversibility rate due to skin friction.

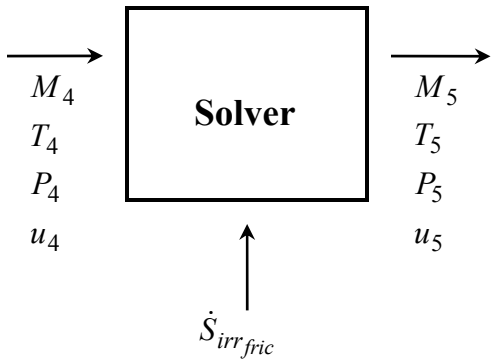

Figure 4-5. Isolated solver description used to calculate combustor entrance properties.

The total temperature at station 5 is equal to that at station 4 and the total pressure loss as a result of the irreversibility due to friction is calculated from

$$\frac{\dot{S}_{irr_{fric}}}{\dot{m}R} = -\ln\left(\frac{P_{t_5}}{P_{t_4}}\right) \tag{4.11}$$

The area of the solver is taken to be that of the inlet throat area. Since the mass flow rate, area, and total pressure and temperature at station 5 are known, the relationship

$$\dot{m} = \frac{P_{t_5}}{\sqrt{RT_{t_5}}} A_5 \sqrt{\gamma} M_5 \left(1 + \frac{\gamma - 1}{2} M_5^2\right)^{(\gamma+1)/(2-2\gamma)} \tag{4.12}$$

can be used to set up a sixth order polynomial (when $\gamma = 1.4$) for the Mach number at station 5. The polynomial is solved using a root finder and only one of the six roots is an acceptable solution (does not contain an imaginary part, is not negative, and is not a subsonic Mach number). Once the correct Mach number is chosen,

$$T_{t_5} = T_5\left(1 + \frac{\gamma - 1}{2} M_5^2\right) \tag{4.13}$$

$$P_{t_5} = P_5\left(1 + \frac{\gamma - 1}{2} M_5^2\right)^{\frac{\gamma}{\gamma-1}} \tag{4.14}$$

are used to determine the pressure and temperature at the combustor entrance.

The total rate of entropy generated by the inlet component is given by

$$\dot{S}_{irr\,inlet} = \dot{S}_{irr\,fric} + \dot{S}_{irr_{shocks\,1-3}} \tag{4.15}$$

which is a sum of the two loss mechanisms found in the inlet; friction and shocks. In addition, the necessary geometric parameters are passed to the aerodynamic program to calculate the vehicle volume and center of gravity.

Inlet Constraints and Constants

The flow of air through the inlet is considered a perfect gas with a constant specific heat ratio of $\gamma = 1.4$ and a specific gas constant of $R = 288.2\ J/kg \cdot K$. This results in a constant pressure specific heat for the inlet of $c_p = 1009\ J/kg \cdot K$. Another parameter that is at a fixed value throughout the inlet is the skin friction coefficient, and it is set at $C_f = 0.00123$. This value was taken from [1] as an average of the Mach 6 and 10 turbulent skin friction coefficients and is comparable to value Riggins [58] employed ($C_f = 0.001$) in his analyses.

There are several constraints imposed on the inlet component, including constraints on the geometry and on flow properties. One geometric constraint is the axial position of the cowl lip, X_{cowl}, and it must fall in the range

$$X_{fb} + X_{ramp1} < X_{cowl} < X_{fb} + X_{ramp1} + X_{ramp2} \tag{4.16}$$

to ensure there is no internal ramp. This must be avoided because, if it were to occur, the second ramp shock could not be focused on the cowl lip and the shock would be ingested into the combustor. A second geometric constraint is applied to prevent the front undersurface of the vehicle from becoming unreasonably large and is represented as

$$X_{inlet} = X_{fb} + X_{ramp1} + X_{ramp2} \le 0.85 L_{veh} \tag{4.17}$$

where L_{veh} is the total vehicle length. Constraints are also applied to the minimum and maximum oblique shock angles that can occur from flow deflection. The minimum shock angle constraint is imposed to prevent either of the ramp angles from falling below 1°. The maximum

shock angle constraint avoids unattainable solutions or strong shock solutions (refer to Figure 3-8) and is therefore set to keep an individual ramp less than 20°. A final geometric constraint limits the angle in which the flow can be turned back as a result of the cowl shock (to avoid a strong shock) and the limit depends on the Mach number just upstream of the cowl shock (28° to 38° for allowable inlet Mach number range).

There are three fairly significant flow property constraints which must be met at the exit of the inlet/entrance to the combustor. The three constraints are

$$2.2 \leq M_5 \leq 4.0 \tag{4.18}$$

$$P_5 \geq 50600 \; N/m^2 \tag{4.19}$$

$$T_5 \leq 2000 \; K \tag{4.20}$$

It is important that these constraints are satisfied to prevent the Mach number from going subsonic for short combustors and also to ensure auto-ignition of the fuel and reasonable reaction times (refer to Section 3.3.1).

Inlet Off-Design Considerations

The oblique shock system solution procedure is, as mentioned, for a vehicle design flight conditions. When the fixed geometry vehicle is at off-design, the oblique shock system changes. In other words, a vehicle with fixed geometry and at Mach 8 flight conditions will not have the same shock structure (i.e. angles) as the Mach 10 flight conditions. Therefore, to ensure the 'shock-on-lip' condition over all flight conditions, some additional 'device' is required to tailor the oblique shock structure.

The method used in this thesis work to focus the oblique shocks on the cowl lip over the flight envelope is the concept of thermal energy exchange developed by Moorhouse, Hoke, and Prendergast [6]. As mentioned earlier, this simplified method is readily adaptable to one-dimensional analysis. Energy exchange is required at two places: in front of the forebody oblique shock and in front of the first ramp oblique shock. The energy exchange process in front of the forebody oblique shock and the first ramp oblique shock is demonstrated in Figure 4-6.

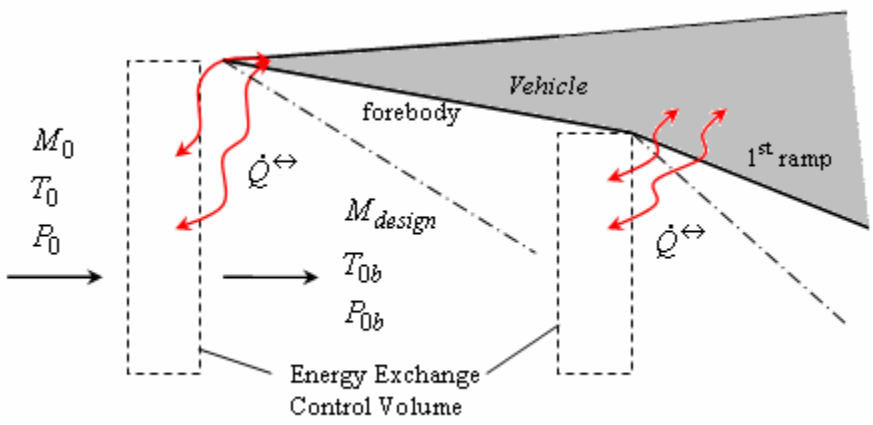

Figure 4-6. Oblique shock tailoring with energy exchange.

A design Mach number is chosen for the design flight conditions and equals $M_{design} = 9$ for this analysis unless otherwise stated. The cross-sectional area of the energy exchange control volume equals the freestream capture area, A_{total} (see Figure 4-1). For a given freestream Mach number M_0, the thermal energy required to achieve the design Mach number is found using

$$\dot{Q}^{\leftrightarrow} = \dot{m} c_p \left(T_{t_{0b}} - T_{t_0} \right) \tag{4.21}$$

where the total temperature exiting the energy exchange control volume is obtained from

$$\frac{T_{t_{0b}}}{T_{t_0}} = \left(\frac{1+\gamma M_0^2}{1+\gamma M_{design}^2} \right)^2 \left(\frac{M_{design}^2}{M_0^2} \right)^2 \left(\frac{1+\frac{\gamma-1}{2} M_{design}^2}{1+\frac{\gamma-1}{2} M_0^2} \right) \tag{4.22}$$

For freestream Mach numbers less than the design Mach number, thermal energy must be extracted to achieve the design value and, conversely, thermal energy must be added to the flow at Mach numbers greater than the design value. Once $T_{t_{0b}}$ is calculated, the temperature and pressure exiting the control volume are determined from Equations (3.11) and (3.19). The entropy generated from this process is calculated by applying an entropy balance (Equation (3.8)) to the control volume shown in Figure 4-6.

A vehicle with fixed geometry (fixed values of A_{total}, X_{cowl}, θ_{fb}) may inevitably require a different angle-of-attack(α) at off-design flight conditions and, in accordance with Equation (4.4), consequently results in a different forebody oblique shock angle. Therefore, a design Mach number different from that presented above is necessary to maintain the shock-on-lip condition.

The same methodology is applied to the energy exchange process before the first inlet ramp shock. However, to maintain both ramp shocks focused on the cowl lip, the Mach number before the first inlet ramp shock must be the same over all flight conditions. Equations (4.21) and (4.22) are once again applied along with Equations (3.11) and (3.19) to determine the required energy exchange and the flow properties before the shock.

The need for a device to tailor the oblique shock system is just one example of the complexity of hypersonic vehicle systems and it also demonstrates the interrelated nature of the propulsion and aerodynamic systems.

4.1.2 Combustor Component Description and Modeling

A constant area combustor, equal to the inlet throat area, allows air entering at station 5 to react with hydrogen fuel which results in combustion products which exit the combustor at station 6. The combustion process takes place within a mixing layer where the air and hydrogen have sufficiently mixed to combustible proportions. Realistically, variations of the flow properties of the combustion products exiting the combustion would occur. However, the combustor model used in this thesis work assumes that the mixing layer occupies the entire combustor area to provide uniform combustor exit flow properties. Heat loss through the combustor walls and drag due to skin friction and injectors are included in the model. Figure 4-7 shows a simple sketch of the combustor along with the only design decision variable associated with the combustor component, the combustor length.

The combustion of air with hydrogen fuel is governed for this analysis by the overall reaction and the stoichiometric reaction mechanism, and are represented as, respectively,

$$H_2 + a(O_2 + 3.76N_2) \rightarrow bH_2O + cO_2 + dH_2 + 3.76aN_2 \tag{4.23}$$

$$H_2 + 1/2O_2 \rightarrow H_2O \tag{4.24}$$

This combustion model, as can be seen from Equation (4.23), captures the affect of incomplete combustion but it does not, however, include species dissociation. Species dissociation is not included in the combustor (or nozzle) because finite-rate kinetics is quite difficult to model and since we are simulating and mathematically optimizing the vehicle over a mission, finite-rate kinetics may present a rather large computational burden, which is unacceptable for the purposes of this analysis.

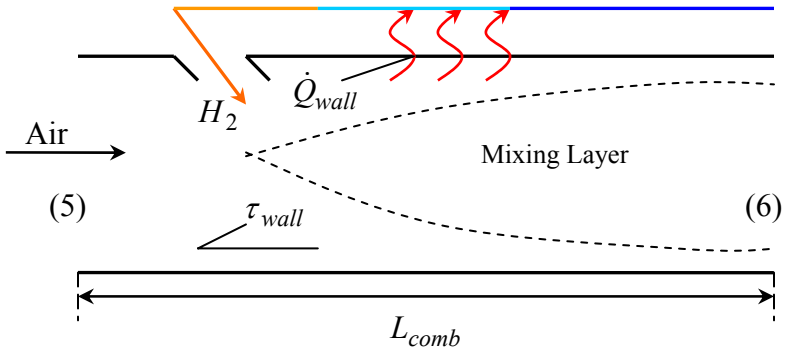

Figure 4-7. Combustor component schematic with station numbers.

Combustor Constraints and Constants

The constant pressure specific heat, c_p, is held constant throughout the combustor and is calculated using (for example, for air at the combustor entrance, station 5)

$$c_p = 0.21 c_{p_{O_2}}(T_5) + 0.79 c_{p_{N_2}}(T_5) \tag{4.25}$$

Therefore, the ratio of specific heats, γ, is constant throughout the combustor as well[42]. Likewise, the skin friction coefficient is fixed at a value of $C_f = 0.015$, as suggested by Riggins [58]. The skin friction coefficient is set to a relatively high value to capture the affects of drag caused by the combustor walls and the intrusive injectors. Additionally, the molecular weight and specific gas constant of the combustor flow are held constant at values equal to that of air, i.e. their changes are of secondary importance.

[42] Note that the effect of this assumption of constant specific heats is examined numerically in Chapter 6.

Hydrogen fuel is injected into the combustor at a 45° angle in order to achieve adequate mixing with the air. Fuel injection conditions are set to the following:

$$M_{H_2} = 1.0, \quad T_{H_2} = 600\ K, \quad P_{H_2} = 101325\ N/m^2, \quad \gamma_{H_2} = 1.4$$

In reality, the temperature of the fuel being injected into the combustor would be determined from the heat removed from the combustor and nozzle. However, for this analysis, the injection temperature is fixed, and instead the mass flow rate necessary to complete the required cooling is calculated (discussed shortly). The constant pressure specific heat of hydrogen is determined from [43]

$$\bar{c}_{p_{H_2}} = \frac{1}{T_{H_2} - T_{t_{H_2}}} \int_{T_{t_{H_2}}}^{T_{H_2}} c_{p_{H_2}} dT \tag{4.26}$$

where T_{H_2} is the fuel injection temperature and $T_{t_{H_2}}$ is the total temperature of the injected fuel. The heat of reaction[43] for hydrogen and the stoichiometric fuel/air ratio are, respectively, $h_{pr} = 119{,}954\ kJ/kg$ and $f_{st} = 0.0294$.

Other than the length constraint placed on the decision variable L_{comb}, there are only two additional constraints placed on the combustor component. The first is that the flow through the combustor must remain supersonic at all operating conditions. The second is that the combustor length cannot be longer than the length for the minor mixant[44] to be depleted. This is undesirable because the combustor, as modeled for this work, allows no further combustion once the minor mixant is depleted.

Combustor Solution Procedure

The combustor component is solved in a differential 'marching' fashion from combustor entrance to exit. A differential element of the mixing layer, *dx*, is depicted in Figure 4-8 where the upstream control volume face is labeled '*x*' and the downstream control volume face is labeled '*x*+*dx*'. It is shown that at each differential step the change in Mach number,

[43] The heat of reaction is equivalent to the lower heating value (LHV) at standard conditions.
[44] Defined as either fuel or air, depending on whether the overall equivalence ratio is less than or greater than 1.

temperature, pressure, and rate of irreversibilities are calculated and then are updated in the fashion, for example, of

$$M_{x+dx} = M_x + dM \tag{4.27}$$

where M_{x+dx} becomes M_x for the next step. A differential amount of hydrogen fuel, $\delta\dot{m}_{H_2}$, is added to the main gas stream (initially air) and the differential combustor wall heat loss is calculated at each step as well. In addition, the molar flow rates and mole fractions of each species included in Equation (4.16) are determined and needed for the irreversibility calculation.

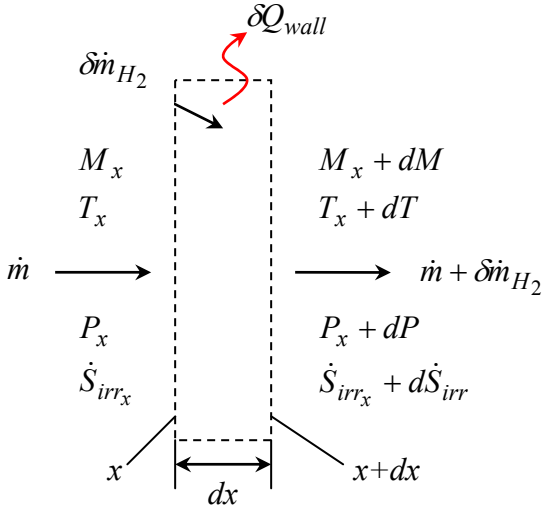

Figure 4-8. Mixing layer differential element

The differential equations utilized in the combustor sub-system analysis are given by Shapiro's influence coefficients method [43]. The change in Mach number, temperature, and pressure at each step are obtained from

$$\frac{dM}{M_x} = \frac{1+\gamma M_x^2}{2\left(1-M_x^2\right)}\frac{dH - \delta Q_{wall}}{c_p T_x} + \frac{\gamma M_x^2\left(1+\frac{\gamma-1}{2}M_x^2\right)}{2\left(1-M_x^2\right)}\left(\frac{4C_f\,dx}{D_h} - 2y\frac{\delta\dot{m}_{H_2}}{\dot{m}}\right)$$
$$+ \frac{\left(1+\gamma M_x^2\right)\left(1+\frac{\gamma-1}{2}M_x^2\right)}{1-M_x^2}\frac{\delta\dot{m}_{H_2}}{\dot{m}} \tag{4.28}$$

$$\frac{dT}{T_x} = \frac{1-\gamma M_x^2}{1-M_x^2}\frac{dH-\delta Q_{wall}}{c_p T_x} - \frac{\gamma(\gamma-1)M_x^4}{2\left(1-M_x^2\right)}\left(\frac{4C_f dx}{D_h} - 2y\frac{\delta\dot{m}_{H_2}}{\dot{m}}\right)$$
$$-\frac{(\gamma-1)M_x^2\left(1+\gamma M_x^2\right)}{1-M_x^2}\frac{\delta\dot{m}_{H_2}}{\dot{m}} \tag{4.29}$$

$$\frac{dP}{P_x} = -\frac{\gamma M_x^2}{1-M_x^2}\frac{dH-\delta Q_{wall}}{c_p T_x} - \frac{\gamma M_x^2\left[1+(\gamma-1)M_x^2\right]}{2\left(1-M_x^2\right)}\left(\frac{4C_f dx}{D_h} - 2y\frac{\delta\dot{m}_{H_2}}{\dot{m}}\right)$$
$$-\frac{2\gamma M_x^2\left(1+\frac{\gamma-1}{2}M_x^2\right)}{1-M_x^2}\frac{\delta\dot{m}_{H_2}}{\dot{m}} \tag{4.30}$$

where the hydraulic diameter of a rectangular duct per unit width, D_h, and the hydrogen-to-main stream axial velocity ratio, y, are defined as

$$D_h = \frac{2A_x}{A_x + 1} \tag{4.31}$$

$$A_x = A_{throat} \tag{4.31a}$$

and $$y = \frac{u_{x_{H_2}}}{u_x} \tag{4.32}$$

Note the dH and δQ_{wall} are non-rate quantities with the former explained immediately below and the latter in the section *Combustor Wall Heat Loss Model*. In addition, the first group of terms on the right hand side of Equations (4-28) to (4-30) represents the influence of energy addition from fuel and convective heat loss on the main stream Mach number, temperature, and pressure. The second group of terms represents the influence of drag due to wall skin friction, injectors[45], and mass addition on the main stream Mach number, temperature, and pressure. The final group of terms represents the affect of mass addition on the aforementioned properties.

A term common to Equations (4-28) to (4.30) is an energy term defined by

[45] In the combustor model used in this analysis, the drag to injectors is directly incorporated into the skin friction coefficient for simplicity. Another term, however, can be included in the second group on the right hand side of Equations (4.28) to (4.30). See Shapiro [43] for more details.

$$dH = dh_{pr} - \left[\bar{c}_{p_{H_2}} \left(T_x - T_{t_{H_2}} \right) + \frac{u_x^2}{2} \right] \frac{\delta \dot{m}_{H_2}}{\dot{m}} \tag{4.33}$$

that includes enthalpy changes due to both chemical reaction and temperature difference between the injection total temperature, $T_{t_{H_2}}$, and main stream mixture temperature, T_x. The amount of fuel absorbed into the mixing layer at each step and the amount of energy released each step are predicted by mixing efficiency and combustion efficiency models, both of which are described shortly.

The combustor component model implemented in this analysis requires two major assumptions regarding the injection of the fuel. First, fuel mass addition (mixing) and combustion are assumed to commence immediately downstream of the combustor entrance interface, i.e. combustion ignition delay and injector position are ignored. Second, fuel is assumed to be injected (absorbed) continuously along the combustor duct length and into the mixing layer. Both of these approximations create a simplified model of a real injection process.

Mixing and Efficiency Models

As previously mentioned, the hydrogen fuel is injected into the combustor and then incremental amounts are absorbed into the mixing layer as the flow proceeds from combustor entrance to combustor exit. The mass flow rate of the unabsorbed hydrogen stream at any axial combustor location is calculated in [1] as

$$\dot{m}_{H_2}(x) = \dot{m}_{air_5} f_{st} \phi (1 - \eta_M(x)) \tag{4.34}$$

with knowledge of the mixing efficiency, η_M, the equivalence ratio ϕ, and the stoichiometric fuel-to-air ratio, f_{st}. With the mass flow rate of the unabsorbed hydrogen stream known at stations x and $x+dx$, the amount of fuel absorbed into the mixing layer each step is given by

$$\delta \dot{m}_{H_2} = \dot{m}_{H_{2_x}} - \dot{m}_{H_{2_{x+dx}}} \tag{4.35}$$

Equation (4.34) reveals the need for a mixing efficiency to be defined as a function of axial combustor length. A study of chemical kinetics in scramjet burners suggests an exponential

function representation for the mixing efficiency [55]. The mixing efficiency model used is taken from [1] in this analysis and is defined as

$$\eta_M(x) = \frac{1 - e^{\frac{-Ax}{L_m}}}{1 - e^{-A}} \tag{4.36}$$

where A is a fit parameter that represents near-field mixing and L_m is the distance for minor mixant to be mixed to stoichiometric proportion (depleted). The fit parameter A typically varies in the range 1 to 5 and for this analysis it is chosen to be $A = 4.5$ [56, 57]. If the equivalence ratio is less than or equal to unity, the fuel is considered the minor mixant and if the equivalence ratio is greater than unity, the air is considered the minor mixant. The axial distance at which the minor mixant is depleted is given by the relations

$$L_m \cong 0.179 b C_m e^{1.72\phi} \qquad \phi \le 1 \tag{4.37}$$

$$L_m \cong 3.333 b C_m e^{-1.204\phi} \qquad \phi > 1 \tag{4.38}$$

where $b = A_{throat}$ and the mixing constant is C_m. The mixing constant is reported to vary from values of 25 to 60 and is chosen to be $C_m = 47$ for this analysis [61]. It is evident from Equation (4.36) that the mixing efficiency equals unity when combustor length equals the length for the minor mixant to be depleted, i.e. $\eta_M = 1$ when $L_{comb} = L_m$. The exponential nature of the mixing efficiency, along with the combustion efficiency (defined below), is illustrated in Figure 4-9 for an example combustor length of 1 m (assumes $L_m = 1$ as well).

A combustion efficiency model is required to calculate the incremental energy release by the fuel per step in Equation (4.33). As seen in Figure 4-9, the combustion efficiency is also an exponential function, however, it grows at a slower rate than the mixing efficiency and attains a value of $\eta_b = 0.9$ at a value of $\eta_M = 1$. The relations for the combustion efficiency model and the incremental energy release at a given axial location are described by, respectively,

$$\eta_b(x) = 1 - e^{\frac{-Bx}{L_m}} \tag{4.39}$$

$$dh_{pr} = \eta_b(x+dx)h_{pr} - \eta_b(x)h_{pr} \tag{4.40}$$

The coefficient B is once again a fit parameter and is chosen to be $B = 2.3$ to provide the characteristics displayed in Figure 4-9.

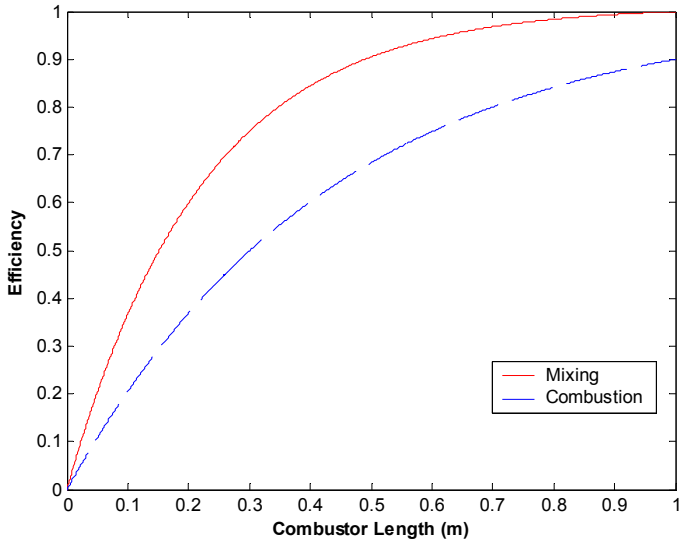

Figure 4-9. Axial growth of the mixing and combustion efficiencies for the combustor component.

Combustor Wall Heat Loss Model

The total enthalpies encountered in the combustor during hypersonic flight demands the need for combustor wall cooling to avoid material temperature limits. This is accomplished by using the fuel to be injected into the combustor as the coolant and, thereby, preventing excessive energy 'waste'. Before the amount of fuel necessary for cooling can be calculated, an estimate of the convective wall heat transfer must be provided.

The technique used in this thesis work to estimate the convective wall heat transfer is the *Eckert Reference Enthalpy Method* [1]. This method is based upon the premise that the overall effects of a variable property boundary layer can be replaced by those of a constant property boundary layer whose properties reflect that of an average reference enthalpy and temperature. A significant restriction on this method is that it cannot be applied when species dissociation occurs.

The first step in the Eckert reference enthalpy method is to solve for the *reference enthalpy* from

$$h^* = \frac{h_e + h_w}{2} + 0.22r\frac{u_e^2}{2} \tag{4.41}$$

where the recovery factor r is determined from the relationship

$$r = \frac{h_{aw} - h_e}{\frac{u_e^2}{2}} \tag{4.42}$$

In Equations (4.41) and (4.42) the subscript *e* refers to the undisturbed flow at the outer edge of the boundary layer at the combustor entrance, i.e. station 5 while *w* refers to the conditions at the wall and *aw* refers to adiabatic wall. The adiabatic wall enthalpy and the enthalpy at the combustor entrance need to be determined for calculation of the recovery factor and are done so by knowledge of the total temperature and static temperature, respectively. The maximum combustor wall temperature desired is set to $T_w = 1960\ ^\circ R = 1088.7\ K$ for this analysis. This temperature (T_w) is used to obtain the wall enthalpy and is used in conjunction with the recovery factor and station 5 properties to compute the reference enthalpy (Equation (4.41)). Iteration is then utilized to obtain the reference temperature T^* which is required to determine the convective wall heat flux from the following:

$$\dot{q}_{wall} = \frac{0.0287 P_e u_e \left(h_{aw} - h_w\right)}{RT^* \,\mathrm{Pr}^{*2/5}\, \mathrm{Re}_x^{*1/5}} \tag{4.43}$$

$$\mathrm{Re}_x^* = \frac{P_e u_e L_{comb}}{RT^* \mu^*} \tag{4.44}$$

$$\mathrm{Pr}^* = r^{1/3} \tag{4.45}$$

The reference Prandtl number and the convective wall heat transfer relations, given by Equations (4.44) and (4.45), respectively, assume turbulent flow at the combustor entrance. It is apparent that the reference Prandtl number is simply a function of the recovery factor and the convective wall heat transfer is a function of both reference and combustor entrance conditions. The units of the heat flux $\dot{q}_{wall}$ in Equation (4.43) are W/m^2. Therefore, to obtain the differential heat

loss per step $\left(\delta Q_{wall}\right)$ on a per unit mass basis in Equations (4.28) to (4.30), Equation (4.43) must be divided by the combustor entrance mass flow rate and then multiplied by the differential surface area[46] $dA_{surf} = 2dx\left(A_x + 1\right)$. Additionally, the reference kinematic viscosity required for calculation of the reference Reynolds number is given by the correlation [1]

$$\mu^* = 1.46\left(10^{-6}\right)\frac{T^{*3/2}}{T^* + 111} \tag{4.46}$$

Although the Eckert Reference Enthalpy Method is based upon combustor entrance and reference conditions, it provides a reasonable approximation to the convective wall heat loss. Available experimental and analytical data support this statement and estimate that convective heat transfer values based on the Eckert method are very likely to be within 10 to 20 percent of the correct value [1].

With knowledge of the total heat removal rate and the hydrogen fuel injection temperature, $T_{H_2} = 600\ K$, the mass flow rate necessary to cool the combustor surfaces can be determined. In this thesis, hydrogen is assumed to be stored in a liquid state and heated to a vapor state, as a result of combustor heat absorption, before being injected into the combustor. The relation

$$\begin{aligned} h_{fc} = {} & c_{p_{liq\,H_2}}\left(T_{vap} - T_{\tan k}\right) + h_{vap} + c_{p_{H_2\,100}}\left(100 - T_{vap}\right) + c_{p_{H_2\,400}}\left(400 - 100\right) \\ & + c_{p_{H_2\,600}}\left(T_{H_2} - 400\right) \end{aligned} \tag{4.47}$$

is used to calculate the amount of thermal energy that is absorbed by each unit mass of fuel in going from storage conditions to injection conditions. Equation (4.47) is the sum of the enthalpy of vaporization of hydrogen, $h_{vap} = 454.3\ kJ/kg$, and all the sensible enthalpy increases over a given temperature range. The specific heats used in Equation (4.47) are averaged over the temperature range in the adjacent parenthesis. The vaporization temperature of liquid hydrogen is known to be $T_{vap} = 20.35\ K$. Therefore, the mass flow rate needed for cooling is determined from

[46] This is for a rectangular duct per unit width.

$$\dot{m}_{H_{2need}} = \frac{1.5\dot{Q}_{wall}}{h_{fc}} \tag{4.48}$$

where $\dot{Q}_{wall}$ is the heat flux $\dot{q}_{wall}$ multiplied by the wall surface area and the factor of 1.5 is added to the numerator to account for heat removal in the nozzle, i.e. nozzle heat loss is assumed to be 50 percent[47] of combustor the heat loss. Realistically, an iterative scheme between the combustor and nozzle would be required to properly thermally balance the vehicle. However, doing so for the work done in this thesis would potentially produce a computational burden in the optimization process which would be unacceptable at this juncture[48]. If the needed mass flow rate predicted by Equation (4.48) is greater than that determined from the equivalence ratio, the extra mass flow of hydrogen is assumed to be re-circulated back to the storage tank.

Irreversibilities Due to Loss Mechanisms

There are four major loss mechanisms attributed to the combustor component in this thesis. These loss mechanisms are friction, heat transfer across a finite temperature difference, fuel/air mixing, and incomplete combustion[49]. Each individual loss mechanism creates an irreversible increase in entropy, which is calculated at every differential step (*dx*). The relations for the rate irreversibility increases due to friction, heat transfer, incomplete combustion, and mixing are given respectively, as

$$d\dot{S}_{irr_{fric}} = \frac{\dot{m}C_f u_x^2 dA_{surf}}{2T_x A_x} \tag{4.49}$$

$$d\dot{S}_{irr_{ht}} = \delta\dot{Q}_{wall}\left(\frac{1}{T_{H_2}} - \frac{1}{T_w}\right) \tag{4.50}$$

$$d\dot{S}_{irr_{inc\ comb}} = \dot{m}_{H_2} dh_{pr}\left(\frac{1}{T_{H_2}} - \frac{1}{T_x}\right) \tag{4.51}$$

[47] The value is assumed based upon individual component assessment.

[48] In effect more computing power in the form, for example, of a distributed set of PC workstations would be required for the large-scale optimization used here. As is, only a single PC workstation was available for this work.

[49] The unburned fuel taken into account with the combustion efficiency is a loss but not a loss mechanism which results in an increased entropy generation.

$$d\dot{S}_{irr_{mix}} = \frac{\delta\dot{Q}_{wall}}{T_w} - \frac{\dot{m}_{H_2} dh_{pr}}{T_x} - d\dot{S}_{irr_{fric}} + \sum_1^j \dot{m}_j \left(c_{p_j} \ln \frac{T_{x+dx}}{T_x} - R \ln \frac{P_{x+dx}}{P_x} - R \ln \frac{x_{j_{x+dx}}}{x_{j_x}} \right) \tag{4.52}$$

where x_j is the mass fraction calculated from

$$x_j = \frac{y_j MW_j}{MW} \tag{4.53}$$

using the mole fraction y_j and the molecular weights of each constituent and the main gas stream (MW_j and MW, respectively). The rates of irreversibility increases predicted by Equations (4.49) to (4.52) are all in units of kW/K and are updated each step as shown in Equation (4.27). The rate of irreversibility produced by heat transfer is calculated by drawing a control volume containing the combustor walls only. Incomplete combustion losses are obtained by drawing a control volume around the fuel stream and main stream (mixing layer) interface. The mixing losses are determined from an entropy balance (Equation (3.8)) on a differential element of the main stream. The sum of all these losses results in the total rate of irreversibility produced by the combustor, i.e.

$$\dot{S}_{irr_{comb}} = \dot{S}_{irr_{frict}} + \dot{S}_{irr_{ht}} + \dot{S}_{irr_{inc\ comb}} + \dot{S}_{irr_{mix}} \tag{4.54}$$

It is evident from Equation (4.52) that the mass flow rates and mass fractions of each constituent (j^{th}) must be determined for prediction of mixing losses. Additionally, the molar flow rates of each constituent entering the combustor must be computed for equations to follow and this is done from knowledge of the corresponding mass flow rates and molecular weights. The mass flow rate of hydrogen is known at both x via the mixing model and $x + dx$ via the assumption that all the hydrogen entering the mixing layer is consumed[50]. Therefore, the molar flow rates are known as well and are used to calculate the *reaction coordinate rate* [24], i.e.

$$\dot{n}_{H_{2_{out}}} = \dot{n}_{H_{2_{in}}} + \nu\dot{\varepsilon} \tag{4.55}$$

[50] The reasonableness of this last assumption is discussed following Equation (4.59)

From the assumption of complete combustion, $\dot{n}_{H_{2_{out}}}$ is zero and from the mixing model,

$$\dot{n}_{H_{2_{in}}} = \dot{n}_{H_{2_x}} - \dot{n}_{H_{2_{x+dx}}} \tag{4.55a}$$

Thus, from the reaction mechanism $\nu = 1$ for hydrogen and the reaction coordinate rate is

$$\dot{\varepsilon} = \frac{\dot{n}_{H_{2_{x+dx}}} - \dot{n}_{H_{2_x}}}{-1} \tag{4.55b}$$

As a result, the remaining constituent molar flow rates and the mole fraction of each constituent are given by

$$\dot{n}_{O_{2_{x+dx}}} = \dot{n}_{O_{2_x}} + (-0.5)\dot{\varepsilon} \tag{4.56}$$

$$\dot{n}_{N_{2_{x+dx}}} = \dot{n}_{N_{2_x}} \tag{4.57}$$

$$\dot{n}_{H_2O_{x+dx}} = \dot{n}_{H_2O_x} + 1\dot{\varepsilon} \tag{4.58}$$

$$y_j = \frac{\dot{n}_j}{\sum_1^j \dot{n}_j} \tag{4.59}$$

where once again the stoichiometric coefficients of oxygen and water are taken from Equation (4.24). The combustor exit flow mole fractions are passed to the nozzle sub-system along with the flow properties and necessary geometric parameters for nozzle evaluation.

Finally, an explanation is in order regarding the assumption of complete combustion used to calculate the mole flow rates in Equations (4.55) to (4.58), i.e that all the hydrogen entering a differential element is consumed. In terms of equilibrium, it turns out that for the typical range of temperatures (1000 K to 4000 K) and pressures (100,000 N/m^2 – 600,000 N/m^2) involved at the combustor entrance, the deviation of equilibrium from complete combustion of H_2 is about 4.5% at a maximum and usually much less than this (on the order of tenths of a percent of less) towards the lower end up the above mentioned ranges of temperature and pressure. As to non-equilibrium or kinetic considerations, the deviations from complete combustion depend of course, on residence times which for the conditions see by the combustor are probably on the

order of 10^{-4} seconds. As can be seen from Figure 4.10 [1], the reaction rates for the species involved are on the order of 10^{-5} seconds at 1500 K which leads to the reasonable assumption that the kinetic results must also be fairly close to those for the complete combustion of H_2. In fact, at temperatures much close to the low end of our range (i.e. to 1000 K), the deviations can be important but due to the goal of the modeling being done here, i.e. that of vehicle optimization, they are not taken into account in the calculation of the reacted species mole flow rates.

Where non-equilibrium effects are considered is in the use of the combustion efficiency schedule given in Figure 4-9 and appearing in Equation (4.40) and in the calculation of the rate of entropy generation for incomplete combustion, Equation (4.51).

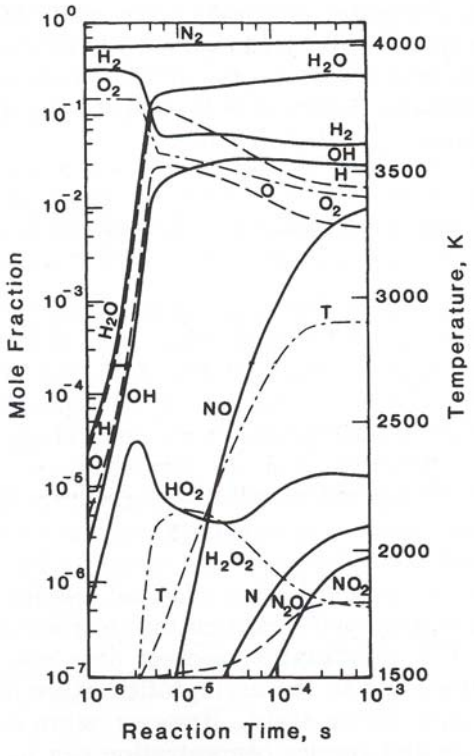

Figure 4-10. Isobaric batch reaction of stoichiometric hydrogen and air mixture. Initial conditions are: P = 2 atm, T = 1500 K. From Heiser et al. [1]; reprinted by permission of the American Institute of Aeronautics and Astronautics.

4.1.3 Nozzle Component Description and Modeling[51]

The combustor exit conditions at station 6, equivalent to the nozzle entrance conditions, are expanded to the nozzle component exit plane, labeled station '7' (see Figure 4-11), to provide the vehicle thrust. The nozzle sub-system is modeled with 'frozen' chemical kinetics, i.e. recombination and dissociation of species exiting the combustor are ignored. The two loss mechanisms incorporated into the nozzle sub-system are friction and heat transfer at a finite temperature difference. A physical representation of the nozzle sub-system is displayed in Figure 4-11.

Two design decision variables are assigned to the nozzle component. One of those is the nozzle expansion angle, θ_{nozz}, which, as shown in Figure 4-11, is simply the angle between the vehicle aftbody and the combustor reference line. The other decision variable is the $\%_{cowl\ ext}$ and is defined by

$$\%_{cowl\ ext} = \frac{L_{cowl_{nozz}}}{L_{nozz}} \tag{4.60}$$

which is merely the ratio of the length that the cowl extends into the nozzle to the total nozzle length. The length of the nozzle is fixed by the previously determined inlet and combustor lengths and the overall vehicle length.

Only two constraints are imposed on the nozzle component for this analysis. The nozzle expansion angle cannot be larger than 18° because undesirable, two-dimensional boundary layer separation effects manifest beyond this limit [58, 60]. Also, the nozzle exit area referenced from the cowl reference line (i.e. excluding plume area) must be less than 2.5 times the inlet capture area. This constraint is aimed at preventing excessive nozzle exit areas and possibly overexpansion.

The same differential 'marching' scheme as used in the combustor is employed in the nozzle analysis, except with slight variations in the differential equations. The change in Mach number, total pressure, and total temperature at each step are governed by

[51] The nozzle component model presented here was developed as part of the M.S. thesis work [62] of K. M. Brewer at Virginia Tech who has worked in collaboration with me on the developing the hypersonic vehicle model. His work is ongoing with an anticipated completion date of May 2005.

$$\frac{dM}{M_x} = \frac{\left(1+\frac{\gamma-1}{2}M_x^2\right)}{1-M_x^2}\left[-\frac{dA}{A_x}+\frac{1+\gamma M_x^2}{2}\frac{dT_t}{T_{t_x}}+2\gamma M_x^2 C_f\frac{dx}{D_h}\right] \tag{4.61}$$

$$\frac{dP_t}{P_{t_x}} = -\frac{\gamma M_x^2}{2}\left(\frac{dT_t}{T_{t_x}}+\frac{4C_f dx}{D_h}\right) \tag{4.62}$$

$$\frac{dT_t}{T_{t_x}} = \frac{1}{\left(1+\frac{\gamma-1}{2}M_x^2\right)}\frac{-\delta Q_{wall}}{c_p T_x} \tag{4.63}$$

The skin friction coefficient in Equations (4.61) to (4.63) is held constant at $C_f = 0.005$ as suggested by Riggins [58]. The specific heat ratio is calculated based upon the chemical composition and properties of the combustor exit flow and is held constant at that value. The specific heat is also determined from the chemical composition, however, it is adjusted each step based upon the local temperature, T_x. Also, in Equations (4.61) to (4.63), it is important to include the additional area resulting from the exhaust plume when calculating area changes. On a similar note, an appropriate hydraulic diameter must be specified as a function of nozzle length, i.e. it changes when the cowl extension portion ends. The nozzle hydraulic diameter is defined as

$$D_{h_{inner}} = \frac{2A_x}{1+A_x} \tag{4.64}$$

for the portion of the nozzle which contains the cowl extension and as

$$D_{h_{outer}} = 4A_x \tag{4.65}$$

for the portion of the nozzle where the plume exists.

The nozzle component also makes use of the Eckert reference enthalpy method to predict nozzle heat losses (see the combustor component) and maintains the same maximum wall temperature as that used by the combustor. However, it has been determined that this method

over-predicts the heat loss by a rather substantial portion[52]. This is because, in reality, the heat loss in a nozzle is greatest in the vicinity of the combustor exit and drops off considerably as the flow is expanded to nozzle exit conditions. Therefore, to compensate for this decline in heat loss a simple assumption is made based on Riggins [58] that the heat loss is half of that provided by the Eckert Method. This is consistent with the assumption made in the combustor where the nozzle heat loss is taken into account when determining the mass flow rate of fuel needed for the vehicle surface cooling. Again, as mentioned earlier, this is to avoid a possibly significant computational burden which would be imposed by iterating between the nozzle and combustor.

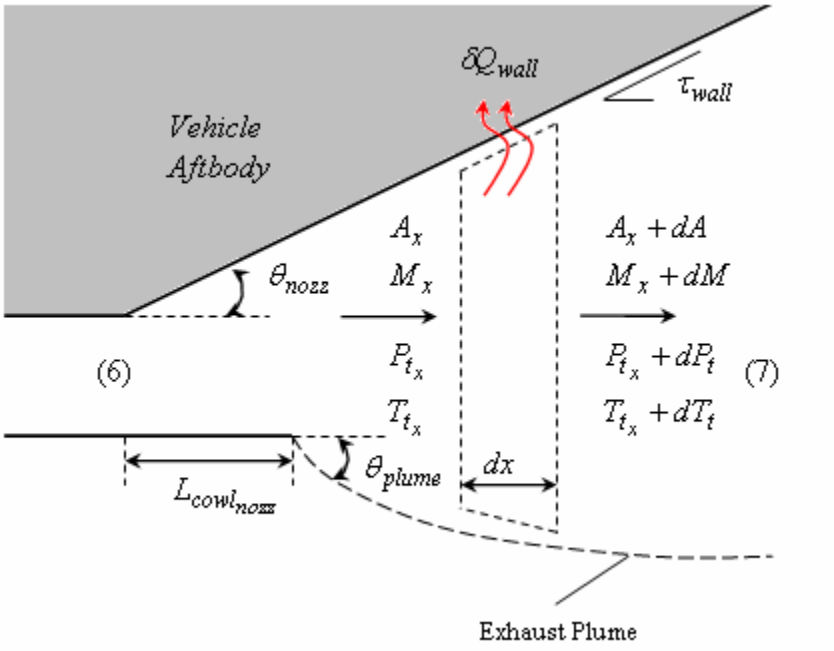

Figure 4-11. Nozzle component schematic including station numbers and other geometric parameters.

The shape of the exhaust plume as seen in Figure 4-11 is determined from the combination of Newtonian and Modified Newtonian theories [63]. The location of the plume 'line' is where, at each step, the exhaust pressure P_x equals the pressure outside the plume, termed P_{outer_x}. The pressure outside the plume is given by

[52] This statement has been substantiated in private discussions with Riggins [58] and through component investigations.

$$P_{outer_x} = P_{cowl}\left[1+\frac{\gamma M_{cowl}^2}{2}C_{p_{com}}\left(\gamma, M_{cowl}, \theta_{plume}\right)\right] \tag{4.66}$$

where the compressible pressure coefficient is defined for the Newtonian and Modified Newtonian theories, respectively, as

$$C_{p_{com}} = 2\sin^2\left(\theta_{plume}\right) \tag{4.67}$$

$$C_{p_{com}} = \frac{2\sin^2\left(\theta_{plume}\right)}{\gamma M_{cowl}^2}\left\{\left[\frac{(\gamma+1)^2 M_{cowl}^2}{4\gamma M_{cowl}^2 - 2(\gamma-1)}\right]^{\frac{\gamma}{\gamma-1}}\left[\frac{2\gamma M_{cowl}^2 - (\gamma-1)}{\gamma+1}\right] - 1\right\} \tag{4.68}$$

It is apparent that the pressure coefficient predicted by the Newtonian theory is a more general approximation and is a function of the plume angle only. Also, in Equations (4.66) to (4.68) the subscript *cowl*[53] refers to the freestream conditions under the cowl and outside the plume.

Matching the inner and outer plume pressures can be a rather troublesome task. At large ratios of P_x/P_{cowl} (encountered in regions close to the combustor exit), the plume angle required (as determined from Equations (4.66)-(4.68), to equate the inner and outer plume pressures becomes larger (sometimes much larger) than 90°. This is deemed undesirable because it inhibits the nozzle solution procedure significantly[54]. Therefore, to correct this difficulty, the plume angle is fixed at 75° when the aforementioned pressure ratio is greater than the ratio that would produce a plume angle greater than 75°. To determine these limiting pressure ratios over various ranges of M_{cowl}, Equation (4.66) is used in conjunction with Equation (4.67) for $\theta_{plume} = 75^\circ$. The Newtonian pressure coefficient is chosen because it is not a function of either the specific heat ratio or M_{cowl}. When P_x/P_{cowl} is less than the limiting pressure ratio, an iterative solution procedure is employed to find the plume angle which equates the inner and outer plume pressures.

[53] These conditions are not the same as that of station 0 because of the oblique shock under the cowl (see Figure 4-1).
[54] In fact, it prohibits the convergence of the plume angle at values of about 90°.

The rate of irreversibility due to the nozzle loss mechanisms is calculated in a manner different from the combustor. An entropy balance is applied over a control volume encompassing the entire nozzle and is written as

$$\dot{S}_{irr_{nozz}} = \dot{m}_{mix}\left(\sum_{1}^{j} y_j s_{j_7} - \sum_{1}^{j} y_j s_{j_6} - R\log\frac{P_7}{P_6}\right) + \frac{\dot{Q}_{wall}}{T_w} \tag{4.69}$$

where the mole fractions of each constituent remain constant throughout the nozzle and the irreversibility is in units of kW/K.

The nozzle component model, like that for the inlet component, calculates the vertical surface forces which will be used by the airframe sub-system for lift prediction. Also, the moment produced by the vertical surface forces is determined with knowledge of the vehicle center of gravity. As a result of the high pressures exiting the combustor, the nozzle, without a cowl extension, produces rather large force and moment values. Therefore, the design decision variable $\%_{cowl\ ext}$ is included to allow a greater flexibility regarding the production of forces and moments. This topic is also touched upon in the airframe sub-system discussion.

4.2 Airframe Sub-system Description and Modeling[55]

The airframe sub-system performs many tasks to determine whether the generated vehicle configuration is acceptable for given flight conditions. One main function is to calculate the external vehicle surface forces (i.e. non-propulsive forces) and determine the total pitching moment as a result of these forces and the propulsive forces. The airframe sub-system must provide a means to trim the pitching moments during all flight conditions. Another main function of this sub-system is to estimate the lift needed from additional planform area, which for this thesis work is a wing. Vehicle volume and weight estimations are also made, both of which play an important role in predicting vehicle trim and wing size. Finally, the airframe sub-system ensures that the thrust required to perform a specified mission is provided.

[55] The airframe sub-system model presented here is the combined effort of the M.S. thesis work of K. M. Brewer at Virginia Tech and me. His work is at present on-going with an anticipated completion date of May 2005.

4.2.1 Vehicle Volume and Center of Gravity Estimation

The determination of the vehicle volume and center of gravity is essential to the computation of pitching moments and vehicle weight. Vehicle volume is calculated by integration of line segments to find the area under the curve and the center of gravity is estimated by dividing the vehicle into a series of 'panels'. A complete hypersonic vehicle sketch (side view only) is provided in Figure 4-12 to supplement the discussion of vehicle volume calculation and to show an example center of gravity position. Figure 4-13 displays the vehicle broken down into 'panels' to provide a simple means of estimating the center of gravity.

Once the forebody and inlet geometry is established, the vehicle volume per unit width can be calculated. As seen in Figure 4-12, six line segments are created, for example, $\overline{12}$, $\overline{13}$, etc.; and the equation for each line segment is determined. Each equation is then integrated over its appropriate 'x' distance to find the area under the line segment. Knowledge of the six areas permits the calculation of vehicle volume per unit width. The mathematical representation of the volume per unit width (i.e. area) is given by

$$\forall_{veh} = \int_{x_1}^{x_2} f_{12}(x)dx - \int_{x_1}^{x_3} f_{13}(x)dx - \int_{x_3}^{x_4} f_{34}(x)dx - \int_{x_4}^{x_5} f_{45}(x)dx - \int_{x_6}^{x_2} f_{62}(x)dx \qquad (4.70)$$

where f_{12}, f_{34}, etc. are the equations of the lines.

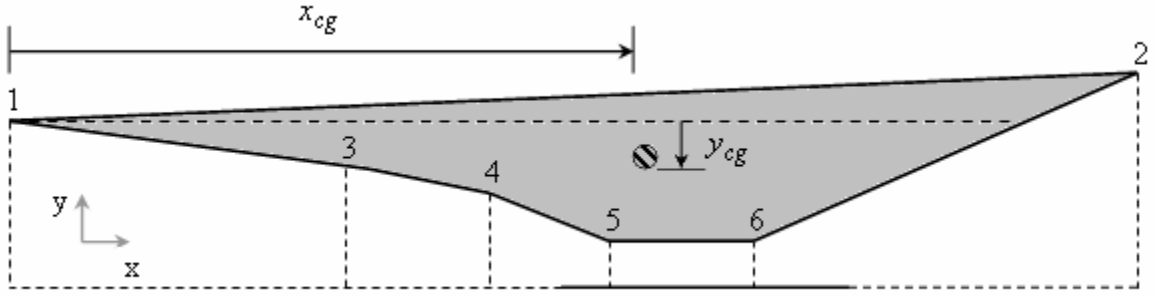

Figure 4-12. Reference points for vehicle volume calculation.

The centroid of the vehicle is determined by a technique known as the *method of composite areas* [64]. Since this analysis assumes a homogeneous distribution of vehicle weight

(fuel evenly distributed throughout body as well), the center of gravity (x_{cg}, y_{cg}) coincides with the centroid of the vehicle. Figure 4-13 displays the five panels (A, B, C, D, E) used in the centroid calculation with each panel being either a triangle or a rectangle. The coordinates of the vehicle center of gravity are defined as

$$x_{cg} = \frac{\sum A_i \bar{x}_i}{A_i} \tag{4.71a}$$

$$y_{cg} = \frac{\sum A_i \bar{y}_i}{A_i} \tag{4.71b}$$

where subscript i represents an individual panel and $\bar{x}, \bar{y}$ define the location of each panels centroid as shown in Figure 4-13 for panel A.

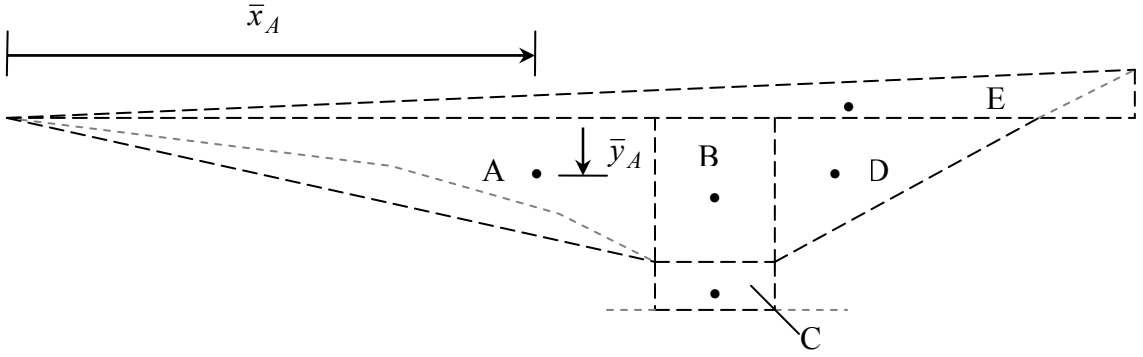

Figure 4-13. Five panels used to estimate the center of gravity. Each panel has its centroid marked by a bullet. The actual vehicle surface is displayed as light, small dashed lines.

4.2.2 Force Accounting and Moment Trim

The force accounting system utilized in this thesis is known as the 'ramp-to-tail' method [21]. A method such as this is used to ensure that all forces are taken into account and no force is 'double-booked' (i.e. counted more than once). There are various other force accounting methods, each possessing their own strengths and weaknesses [49-52]. An airframe/propulsion interface is developed to divide the pressure and shear forces acting on the vehicle surfaces into those charged to propulsion and those charged to the airframe sub-system. Figure 4-14

illustrates all the surface forces acting on the vehicle and shows the airframe surfaces in blue and the propulsion surfaces in red.

As seen in Figure 4-14, the airframe surface forces include both pressure and friction forces whereas the propulsive surface forces are from pressure only[56]. The aerodynamic forces are broken down into x and y-components, depending on the local inclination angle, to predict vehicle lift and drag. Only the y-components of the propulsion forces are needed for lift prediction while the x-components (i.e. drag) are incorporated into the streamthrust difference between propulsion sub-system entrance and exit, i.e. $F_7 - F_1$. Once all surface forces are known, the lift, drag, and thrust of the vehicle can be determined from

$$L_{veh} = \left(\sum F_{p_y} + \sum F_{f_y}\right)\cos\alpha - \left(\sum F_{p_x} + \sum F_{f_x}\right)\sin\alpha \tag{4.72}$$

$$D_{veh} = \left(\sum F_{p_y} + \sum F_{f_y}\right)\sin\alpha + \left(\sum F_{p_x} + \sum F_{f_x}\right)\cos\alpha \tag{4.73}$$

$$T_{veh} = \left(F_7 - F_1\right)\cos\alpha \tag{4.74}$$

where the subscript *f* represents friction, *p* pressure, and the forces are positive in the direction of the reference axis in Figure 4-14. The minus sign is applied to Equation (4.72) because the sum of all y-component forces act in the negative lift direction. However, the sum of all the x-component forces act in the positive drag direction. The lift is calculated in the direction perpendicular to the freestream flow and the drag is calculated in the direction parallel to the freestream flow. The lift and drag directions are not the same as the x and y direction. This can be seen in Figure 4-14 and, hence, the necessity for the cosine and sine terms in Equations (4.72) to (4.74).

All the surface forces shown in Figure 4-14 are assumed to act at the center of the appropriate surface segment. The interior cowl pressure force, occurring in both the inlet and the nozzle, acts at the center of the cowl portion the projects into those components. The streamthrust forces, F_1 and F_7, are assumed to act at the midpoint of the inlet entrance area and the nozzle exit area. The shear forces on the aerodynamic surfaces are determined from

[56] The propulsion shear forces are a much smaller percentage of the total propulsion surface forces than compared to the airframe forces.

$$F_\tau = \frac{1}{2}\rho u^2 C_f A_{surf} \tag{4.75}$$

where local flow properties are used and are considered constant over the entire surface. Also, the skin friction coefficient for the aerodynamic surfaces is fixed at $C_f = 0.001$ [58]. Finally, the vehicle weight acts at the center of gravity computed by Equation (4.71) and the angle-of-attack and vehicle flight angle are needed to compute the x and y-components of the weight force.

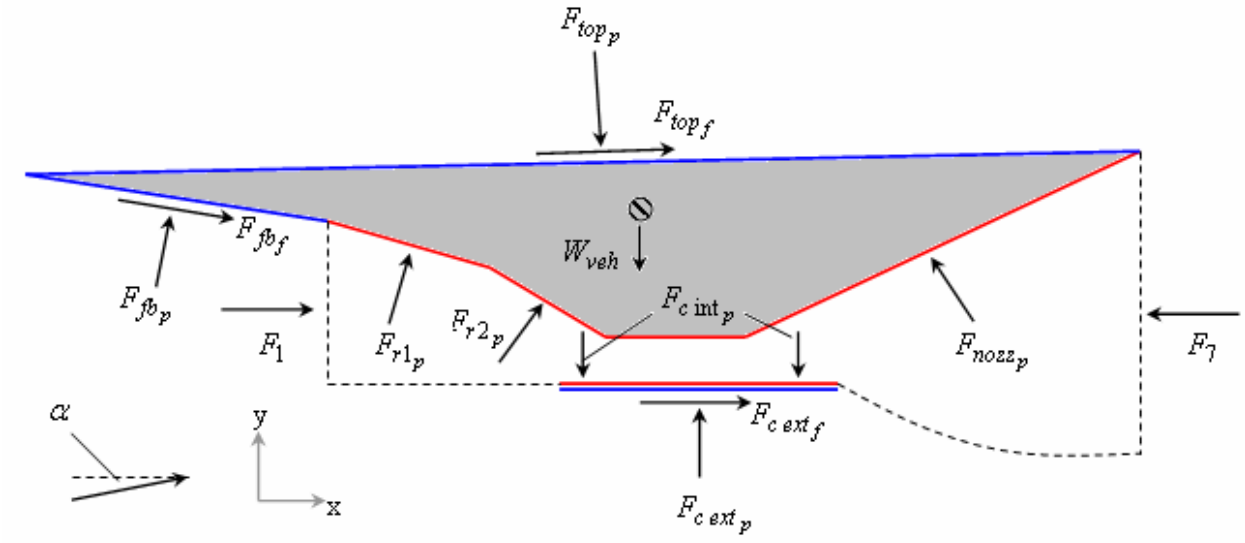

Figure 4-14. Airframe and propulsive forces acting on the hypersonic vehicle.

The propulsion pressure forces are determined, as already noted, in the inlet and nozzle components. The pressure and shear forces on the vehicle upper surface, forebody, and exterior cowl surface are calculated in the airframe sub-system model. The forebody flow properties are obtained in step 1 of the *Inlet Solution Procedure* section of the inlet component discussion. With these flow properties and geometry known, the forebody pressure and friction forces are easily obtained. The flow properties and forces underneath the cowl are obtained in a similar fashion. However, the flow deflection angle is simply equal to the angle-of-attack. Finally, the upper surface flow properties and forces are calculated with knowledge of the angle-of-attack as well as the total capture area and nozzle exit area (measured from the cowl reference line). These two areas permit the calculation of the upper surface deflection angle θ_{top} from simply

geometry. Depending on the magnitudes of α and θ_{top}, the flow either passes through an oblique shock wave or an expansion wave. More specifically, if $\alpha > \theta_{top}$, the freestream flow undergoes a Prandtl-Meyer expansion governed by Equations (3.23) to (3.26) and if $\alpha < \theta_{top}$, the freestream flow passes through an oblique shock wave governed by Equations (3.13) to (3.20). Additionally, if an expansion occurs over the upper surface, then an oblique shock emanates from the vehicle tail to return the flow to its original direction.

The moments resulting from the x and y-components of each force are determined with knowledge of the forces location of action and the center of gravity. Clockwise moments are considered positive and counter-clockwise moments are negative. The moment from the forebody pressure force, for example, and the total pitch moment are given by

$$M_{fb_p} = F_{fb_{p_x}} \left(y_{fb} - y_{cg} \right) + F_{fb_{p_y}} \left(x_{cg} - x_{fb} \right) \tag{4.76}$$

$$M_{pitch} = \sum M_{F_p} + \sum M_{F_f} \tag{4.77}$$

where the total pitch moment must be trimmed (i.e. balanced) to provide stable flight. The pitch moment is balanced in this thesis work by an elevon placed near the rear of the vehicle (discussed in the next section). Note that the vehicle weight does not add to the pitch moment because it is assumed to act at the vehicle's center of gravity. Also, the nozzle moment (and force) is calculated in the nozzle component at each differential step because of the large variation of pressure over the nozzle surfaces, i.e. a more accurate moment calculation is acquired.

The rate of irreversibility produced by the airframe sub-system result from oblique shocks and aerodynamic drag. It is assumed in this analysis that the pressure drag (known as wave drag) is reversible while the viscous dissipation resulting from friction produces the drag irreversibility. The entropy generated by friction drag, given in Equation (4.78), is simply a function of the friction force and the local temperature and velocity [65]. Equation (4.79) provides the total irreversibility generated by airframe sub-system.

$$\dot{S}_{irr_{fric}} = \frac{F_f u}{T} \tag{4.78}$$

$$\dot{S}_{irr_{aero}} = \sum \dot{S}_{irr_{fric}} + \sum \dot{S}_{irr_{shocks}} \tag{4.79}$$

The shock irreversibility is that produced by the forebody oblique shock, exterior cowl oblique shock, upper surface oblique shock, and the tail oblique shock. In calculating this value, the same mass flow rate as that captured by the propulsion sub-system is used. The units of Equation (4.79) are once again kW/K.

4.2.3 Wing and Elevon Details

To approximate the additional lifting surface required and the trim balance moment, fairly simplified wing and elevon models were developed. A wing, assumed to be independent of the vehicle body, is incorporated as the additional lifting surface in this thesis work because it provides a straightforward means for approximating the lift and drag coefficients. In reality, the additional lifting surface may be a blended extension of the vehicle body outboard of the propulsion sub-system (see Chapter 1) and therefore not a true wing. A plan view of the wing and elevon concepts used in this analysis is given in Figure 4-15.

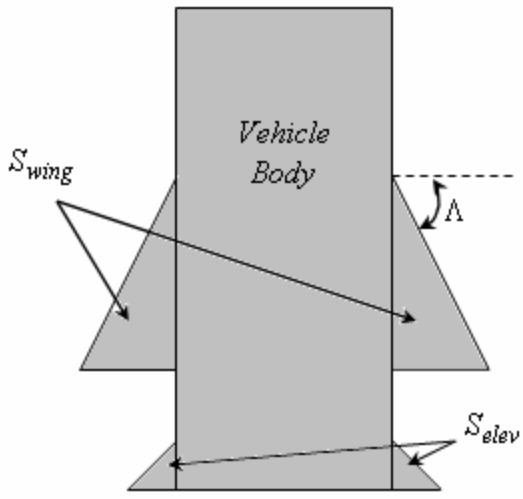

Figure 4-15. Plan view of vehicle showing wing and elevon concepts.

The wing and elevon are assumed to be of a simple delta configuration with a 5% thickness-to-chord ratio (t/c) diamond airfoil cross-section [66, 67]. The wing is attached to the vehicle body at a zero degree inclination angle and is assumed to be positioned such that its

center of pressure is in line with the vehicle center of gravity and, therefore, does not contribute to the vehicle pitching moment. The elevon's center of pressure is assumed to be located two meters from the tail of the vehicle to be able, if necessary, to provide rather large trim balance moments. The diamond airfoils are assumed to be inviscid and, therefore, shock-expansion theory[57] is implemented in the calculation of the lift and drag coefficients. A schematic of the diamond airfoil cross-section is given in Figure 4-16 at some fixed angle-of-attack which, along with the freestream flight conditions, allows the pressure distribution shown in the figure to be calculated.

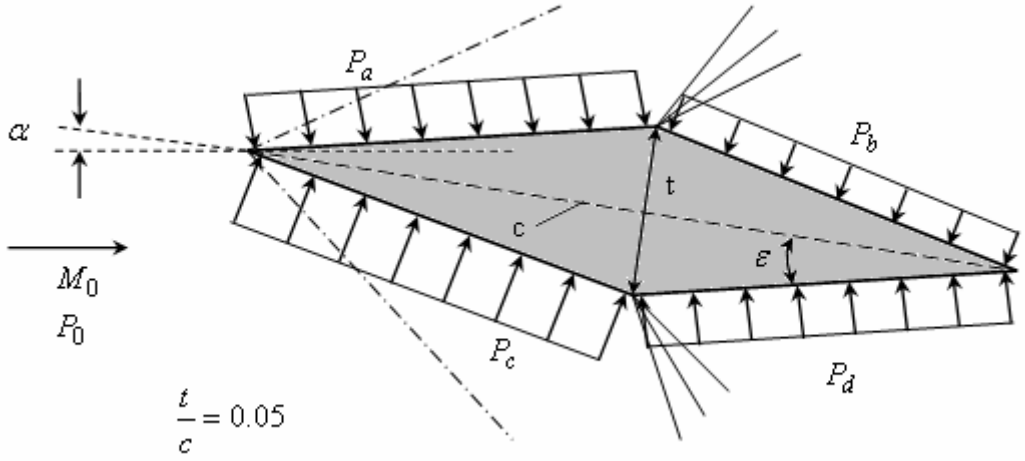

Figure 4-16. Diamond airfoil cross-section used to describe the wing and elevon. A given angle-of-attack and freestream properties produce a pressure distribution as shown. The airfoil thickness and chord length are shown as well.

The freestream flow is initially deflected into itself by an angle $\alpha + \varepsilon$ on the bottom surface of the airfoil, thereby passing through an oblique shock wave. The Mach number and pressure downstream of the shock (*c*) are obtained from the oblique shock relations provided in Chapter 3. The flow is then expanded through an angle 2ε where the Prandl-Meyer expansion relations are used to determine the Mach number and pressure at location *d*. The flow is then either shocked or expanded back to its original direction, depending on the magnitude of the angle-of-attack. The freestream flow can be either initially compressed or expanded on the top surface (a), once again depending on the magnitude of the angle-of-attack. If compressed, the

[57] Shock-expansion theory *exactly* predicts the lift and drag coefficients of inviscid diamond airfoils [3].

flow deflection angle, as seen in Figure 4-16, is equal to the quantity $\varepsilon - \alpha$ and otherwise, the flow expands through the angle $\alpha - \varepsilon$. Like the bottom surface, the flow then expands through an angle 2ε to conditions at *b* and then shocked back to the freestream flow direction. Also like the bottom surface, oblique shock and Prandtl-Meyer relations are used to determine the Mach number and pressure at both *a* and *b*.

Once the pressures at *a*, *b*, *c*, and *d* are determined, the lift and drag per unit span can be calculated and used to determine the lift and drag coefficients for the diamond airfoil. For the condition $\alpha > \varepsilon$, the lift and drag coefficients are given as

$$C_L = \frac{2l}{\gamma M_0^2 c}\left(\frac{P_c - P_b}{P_0}\cos(\alpha+\varepsilon) + \frac{P_d - P_a}{P_0}\cos(\alpha-\varepsilon)\right) \tag{4.80}$$

$$C_D = \frac{2l}{\gamma M_0^2 c}\left(\frac{P_c - P_b}{P_0}\sin(\alpha+\varepsilon) + \frac{P_d - P_a}{P_0}\sin(\alpha-\varepsilon)\right) \tag{4.81}$$

where the chord length *c*, represented by the dashed line in Figure 4-16, is determined from trigonometric relations and is written as

$$c = \sqrt{2}l(1-\cos(\pi - 2\varepsilon))^{1/2} \tag{4.82}$$

Equations (4.80) to (4.82) are developed using the assumption that the maximum airfoil thickness occurs at 50% of the chord length. The term *l* is the length of each of the four surfaces of the diamond airfoil. Equations (4.80) and (4.82) are almost identical for the condition $\varepsilon > \alpha$ with some subtle differences in signs.

Instead of using the flight angle-of-attack for calculation of the lift and drag coefficients, the elevon iterates through a range of positive and negative deflection angles (relative to the freestream) to see if the pitch moment determined by Equation (4.77) can be trimmed. An elevon area needs to be specified to calculate the lift and drag of the elevon, which for this thesis work is given by Equation (4.83) where the control volume requirement $\overline{V}_{elev} = 0.04$ [36].

$$S_{elev} = \frac{\overline{V}_{elev} L_{veh}}{\left(1 - \frac{x_{cg}}{L_{veh}}\right)} \tag{4.83}$$

The calculated lift and drag of the elevon is not in the same direction as the lift and drag of the vehicle and, therefore, it must be resolved into the appropriate direction. The elevon deflection angle is given by the symbol ω.

For all flight conditions considered in this thesis work, the total lift must equal the instantaneous weight of the vehicle, i.e. $L_{total} = W_{veh}$[58]. The total lift is the sum of the lift provided by the vehicle body and that provided by the wing and elevon. After calculation of the vehicle lift from Equation (4.72) and the lift of the elevon at the required deflection angle, the lift needed from the wing is

$$L_{wing} = L_{total} - L_{veh} - L_{elev} \tag{4.84}$$

which can then by used with the dynamic pressure and lift coefficient to determine the wing planform area S_{wing}. Finally, the total drag is given by

$$D_{total} = D_{veh} + D_{wing} + D_{elev} \tag{4.85}$$

which is, once again, in the direction parallel to the freestream velocity. Equation (3.3) is used to obtain the drag of the wing and elevon.

4.2.4 Mass Fractions and Weight Estimation

A simplified approach is applied in this thesis work to estimate the empty mass of the vehicle, the amount of fuel needed for each mission segment, and consequently the overall vehicle weight. This is necessary because of the lack of analytical relations available for hypersonic vehicle weight estimation which is unlike the case for subsonic or supersonic aircraft. The empty mass of the vehicle is determined from an investigation of potential hypersonic vehicle designs presented in [21] and also in [36, 41, 42]. The empty mass of the vehicle is chosen to be $m_e = 5000\ kg$ per unit width for this work, and it is assigned to a vehicle area[59] (i.e. volume per unit width) of $25\ m^2$.

[58] This statement is true for level flight. If the vehicle is at some angle of attack or climb angle, the weight must be resolved into the lift and drag directions. The resolved lift component of weight must then equal the total lift.

[59] This area was determined through an evaluation of different vehicle configurations and was deemed an appropriated average value of the area.

In order to determine the overall vehicle weight at the beginning of the total mission, an estimate must be made of the fuel consumed during each individual mission segment. The fraction of the initial aircraft mass that must be fuel in order to accomplish a given mission segment is known as the *fuel mass fraction* and is defined as [1]

$$\pi_f = \frac{m_i - m_{final}}{m_i} = 1 - \frac{m_{final}}{m_i} \tag{4.86}$$

The ratio m_{final}/m_i is derived for a hypersonic cruise aircraft and a transatmospheric vehicle in [1]. However, the equation presented for the transatmospheric vehicle is not in terms of desired quantities and, therefore, is re-derived to reflect the equation given for the hypersonic cruise aircraft. The fraction of the initial mass remaining at the end of a mission segment for a cruise vehicle and a vehicle that climbs and accelerates are given respectively, as

$$\frac{m_{final}}{m_i} = \exp\left(-\frac{g_0 R}{\eta_o h_{pr} \dfrac{C_L}{C_D}} \right) \tag{4.87}$$

$$\frac{m_{final}}{m_i} = \exp\left(-\frac{\left(\dfrac{u_{final}^2}{2} - \dfrac{u_i^2}{2} \right) + g\left(\dfrac{C_D}{C_L} R + \left(z_{final} - z_i \right) \right)}{\eta_o h_{pr}} \right) \tag{4.88}$$

where η_0 is the overall efficiency (see Equation (6.5)), g_0 is the acceleration of gravity, and the initial and final velocity and elevation as well as the range R are obtained from the definition of the mission segment. However, Equations (4.87) and (4.88) require an estimation of the vehicle lift-to-drag ratio and the overall vehicle efficiency η_o. It is apparent that as engine overall efficiency and lift-to-drag ratio increase, the fuel mass fraction decreases and as range increases the fuel mass fraction increases. Once all the fuel mass fractions are obtained for the desired mission segments, the initial mass (mass at the beginning of the mission) of the vehicle is estimated by

$$m_i = \frac{m_e}{\left(1 - \sum \pi_f\right)} \tag{4.89}$$

which is simply the combination of the empty mass and the fuel mass. Obviously, if the initial mass fraction does not match what is determined at the end of the mission, the mission must be flown again to close the loop.

4.2.5 Airframe Sub-system Constants and Constraints

Like the propulsion sub-systems, the airframe sub-system uses constant values of the specific heat ratio and constant pressure specific heat which are fixed at $\gamma = 1.4$ and $c_p = 1009\ J/kg \cdot K$. Also, as previously mentioned, the skin friction coefficient on the vehicle (not wing or elevon) surfaces is held at $C_f = 0.001$. Finally, the vehicle is assumed to fly at a fairly high constant dynamic pressure trajectory of $q_0 = 85{,}000\ N/m^2$ for the reasons mentioned in Section 3.1 and the vehicle length is set to $L_{veh} = 24\ m$.

One of the main airframe constraints is placed on the minimum and maximum allowable wing planform area. For this work, the vehicle body width is assumed to be 4 *m*, therefore, the total vehicle volume is $96\ m^3$. The minimum planform area is zero (no wing) and the maximum planform area must be less or equal to 10% of the total volume[60], i.e $0\ m^2 \le S_{wing} \le 9.6\ m^2$. Since the wing area is calculated from the required wing lift at all mission segments (i.e. S_{wing} is an operational decision variable), the constraint $L_{total} = W_{veh}$ is guaranteed at all flight conditions.

Another constraint that must be included is the limit on the maximum elevon deflection angle. This is necessary because as $M_0 \to \infty$ or $P_0 \to 0$, the turning angle predicted by Equation (3.23) approaches a finite value of 130.4° [48]. For example, following steps 1 and 2 of Section 3.2.3, an $M_1 = 7$ gives $\nu(M_1) = 91^\circ$ and, therefore, permits only a maximum elevon

[60] The maximum constraint on the wing planform area was set to prevent unrealistically large planform areas when considering the entire three-dimensional vehicle. For example, if a wing planform area of 10% the total volume is needed to provide the remaining vehicle lift on a per unit width basis, then on a three-dimensional basis all the vehicle forces are 4 times as large (including vehicle weight) and consequently 4 times the wing planform area is needed to provide the remaining lift (i.e. 40% of the total volume).

deflection angle of $\omega = 39.4^{\circ}$. As the freestream Mach number increases, the maximum elevon deflection angle decreases. Thus, constraints are placed on the maximum elevon deflection angle as a function of the freestream Mach number to avoid the breakdown of the Prandlt-Meyer relations given in Equations (3.23) and (3.24).

A final constraint is placed on the amount of thrust produced by the vehicle. For cruise missions, the vehicle thrust must equal the total vehicle drag, i.e. $T_{veh} = D_{total}$. For acceleration and climb missions, the vehicle thrust must equal that calculated from Equation (3.1). To balance the thrust and drag or to obtain the desired thrust, iteration of the equivalence ratio (adjusts amount of fuel injected into the combustor) is required. Each time the equivalence ratio is changed a new pitching moment, wing area, and total drag is determined where they must all satisfy individual constraints. As one can imagine, it can be quite difficult (if not impossible) or time consuming to exactly balance the thrust and drag or obtain the desired thrust. Therefore, this work uses a simplified approach to solving this problem. An initial equivalence ratio is set to allow the calculation of the vehicle thrust and total drag. If $T_{veh} > D_{total}$, the equivalence ratio is decreased by increments of $\phi = 0.1$ until $D_{total} > T_{veh}$, then the equivalence ratio is increased by increments of $\phi = 0.02$ until once again $T_{veh} > D_{total}$. At this point the thrust and drag are considered balanced. If initially the $D_{total} > T_{veh}$, the equivalence ratio is first increased and then decreased in the same manner. The same approach applies in determining the necessary thrust for acceleration and climb except now comparisons are made between the vehicle thrust and the thrust predicted by Equation (3.1). This process is referred to as the *throttling* of the thrust and in doing so, the equivalence ratio is limited to the range $0 \le \phi \le 2.0$ with the upper limit due to the hydrogen self-ignition criterion [54].

Chapter 5

Synthesis/Design Optimization Problem Definition and Strategy

In order to make strides towards achieving the thesis objectives set forth in Chapter 1, it is quite evident that individual component analyses and single point optimizations (i.e. at a fixed Mach number) will be required. However, to further demonstrate the utility of exergy methods for determining hypersonic vehicle configurations, a complete hypersonic mission should be specified. Therefore, this chapter presents the overall syntheis/design task at hand and discusses the optimization approach that was implemented to achieve this design task.

5.1 Problem Definition

The synthesis/design optimization problem proposed here the integrated synthesis/design optimization of the two sub-systems presented in Chapter 4 and their associated components, all of which are part of a hypersonic airbreathing vehicle concept. The airframe and propulsion sub-systems are the only two sub-systems considered, as opposed to the several optimized by Rancruel [26] and Rancruel and von Spakovsky [27-29], because there is currently insufficient information in the literature in regards to the other sub-systems that will be incorporated into hypersonic airbreathing vehicles. Nonetheless, these are the two main sub-systems of a hypersonic vehicle, providing the necessary lift and thrust to carry out a desired mission; and, therefore, they are sufficient for performing preliminary analyses and optimizations as well as demonstrating theory.

The mission is the set of conditions under which the hypersonic vehicle must be synthesized/designed. The mission was developed in joint collaboration with Dr. D. Moorhouse [68] at the Air Force Research Lab (AFRL) at Wright Patterson Air Force Base in order to

demonstrate the ability of the hypersonic vehicle to perform cruise and accelerations over a rather large range of Mach numbers. It is *emphasized* that this is a purely arbitrary, empirical mission defined to exercise the methodology of this thesis work. A general description of the overall mission is displayed in Figure 5-1 along with a more detailed description in Table 5-1. The mission has a total of 7 different mission segments consisting of a combination of cruises, climbs, accelerations/decelerations as well as a turn. Only the hypersonic spectrum of flight is considered in this mission; modeling of the hypersonic vehicle at subsonic, supersonic, and transition from supersonic to hypersonic is not considered. To do so would require modeling of a dual-mode scramjet engine as well as many other complexities and considerations associated with hypersonic vehicles at these flight regimes.

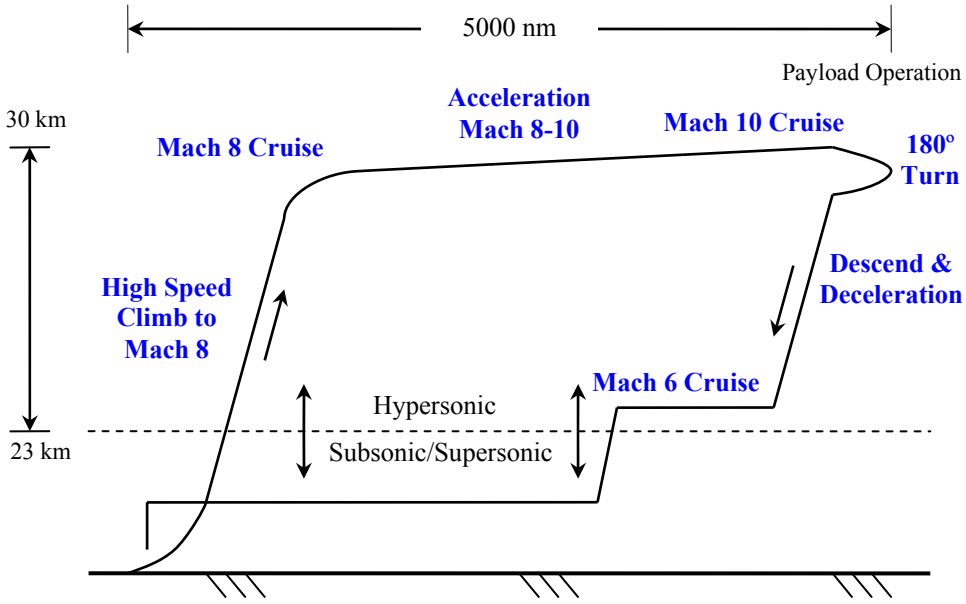

Figure 5-1. Mission profile by segment.

As seen in Figure 5-1 and Table 5-1, the high speed climb to Mach 8 begins at Mach 6 for this work and is considered the lower limit of hypersonic flight. For all climb and acceleration (or descend and decelerate) mission segments, the flight Mach number (consequently the freestream flight properties) is taken to be the average of the initial and final Mach numbers for that segment. The elevation range shown in Figure 5-1 corresponds to that determined by the constant dynamic pressure trajectory of $q_0 = 85{,}000\ N/m^2$ throughout the mission.

Table 5-1. Mission specifications.

Segment	Description
1	Accelerate and climb from Mach 6 to Mach 8, $t \leq 90$ s
2	Mach 8 cruise for 1500 nm
3	Accelerate and climb from Mach 8 to Mach 10, $t \leq 90$ s
4	Mach 10 cruise for 2000 nm
5	Perform a 180º, 2g sustained turn at Mach 10
6	Descend and decelerate to Mach 6 flight conditions
7	Mach 6 cruise for 1000 nm

Before attempting to optimize a hypersonic vehicle over the complete mission described in Figure 5-1 and Table 5-1, single flight Mach number optimizations for cruise and accelerating vehicles will be performed to ensure the component models described in Chapter 4 are functioning properly. Additionally, a partial mission comprised of three mission segments will be optimized before the entire mission[61] to make certain a solution can be found, primarily because of the high non-linearity between sub-systems and strict constraints required by the vehicle. This partial mission will also be useful to ensure that all the necessary parameters are passed from mission segment to mission segment, to give some idea of the time required for optimization, and ultimately to debug and correct any problems encountered in the models or optimization process. Finally, this partial mission will be able to demonstrate the applicability of exergy measures in hypersonic vehicle configuration optimization.

5.2 Optimization Technique

Prior to the optimization of any type of system, complete engineering system models must be developed which typically begins with the selection of a number of degrees of freedom (decision variables) represented by parameters which will be varied within acceptable limits during the optimization process. These independent decision variables, hereby represented by a vector $\vec{x}$, are then used to create two systems of equations to represent the model of the system, i.e.

[61] Note that only the individual mission segments and the partial mission comprised of three mission segments are used in this thesis work. The entire mission will be utilized in the thesis work of K. M. Brewer [62] scheduled for completion in May 2005.

$$\vec{H} = \begin{Bmatrix} \vec{h}_1(\vec{x}) \\ \vec{h}_2(\vec{x}) \\ \vec{h}_3(\vec{x}) \\ \vdots \\ \vec{h}_n(\vec{x}) \end{Bmatrix} = 0 \text{ and } \vec{G} = \begin{Bmatrix} \vec{g}_1(\vec{x}) \\ \vec{g}_2(\vec{x}) \\ \vec{g}_3(\vec{x}) \\ \vdots \\ \vec{g}_n(\vec{x}) \end{Bmatrix} \leq 0 \tag{5.1}$$

The vector of equality constraints $\vec{H}$ is composed of sub-vectors $\vec{h}_i$ each of which mathematically describes a phenomenon or set of phenomena (e.g., those in the inlet or combustor) usually within the realm of a particular discipline. The elements of the sub-vectors $\vec{h}_i$ are known as the *state* equations. The vector of inequality constraints $\vec{G}$ represents natural or artificial limitations imposed upon the system. [26]

With engineering system and sub-system models in hand, optimization subject to a desired set of constraints can now be performed. The system and sub-system models describe the set of nonlinear constraints implemented in the formulation of the optimization problem. The optimization problem is generally expressed as

$$\text{Minimize or Maximize a function } f(\vec{x}) \tag{5.2}$$

with respect to $\vec{x}$ and subject to the following equality and inequality constraints:

$$\vec{H}(\vec{x}) = 0 \tag{5.3}$$

$$\vec{G}(\vec{x}) \leq 0 \tag{5.4}$$

All equality constraints are active by definition whereas an inequality constraint $g_j \leq 0$ is active if $g_j = 0$. The function $f(\vec{x})$ is called the objective function. Three different objective functions are used for vehicle synthesis/design optimization in this thesis work, namely, the overall efficiency (Equation (6.5)) which is based on 1st Law considerations only, the rate of exergy destruction (Equation (6.3)), and the rate of exergy destruction plus the rate of exergy fuel loss (Equation (6.6)).

As a whole, the hypersonic vehicle system described in this thesis work can be viewed as an energy conversion system. Unfortunately, energy conversion system models have a number

of characteristics which make them difficult to optimize. A few reasons for these difficulties are presented by Leyland and are given as follows [69]:

1. Energy conversion system models are highly non-linear and, therefore, relatively robust optimization tools must be used to optimize them.
2. Energy conversion system models often have a number of integer variables and even combinatorial[62] ones which cause the model to become discontinous and disjoint. Therefore, the optimal surface does not have smooth derivates (the optimal surface has jumps in it) and there are several completely different feasible regions, each having its own "global" optimum and with no easy route for passing from one region to another.
3. From the viewpoint of an optimization algorithm, energy conversion system models must often be treated as 'black boxes' – a set of parameters are presented as inputs and the black box provides a number of outputs. Thus, derivatives of the outputs with respect to the inputs and any extra information about the form of the model are usually not available.

If standard nonlinear programming techniques such as gradient-based methods (which are based on assumptions of continuity in the optimal surface) are used to optimize such systems, they will be insufficient and in most cases find a relative optimum closest to the starting point (i.e. a local optimum).

To combat the aforementioned problems, a number of methods have been developed by means of specialized search schemes. These types of algorithms specialize in performing a complete search of the entire synthesis/design space and as a consequence are referred to as global search algorithms [26]. One of the most popular and most developed methods for global searches are Evolutionary Algorithms (EAs), also referred to as Genetic Algorithms (GAs).

An Evolutionary Algorithm is implemented in this work as the means of optimization. The remainder of this section briefly discusses EAs, then describes the specific EA used in this work, and finally a simple test problem is presented to demonstrate the EAs operation.

5.2.1 Evolutionary Algorithms (EAs)

Evolutionary Algorithms are based on the principles of genetics and Darwin's theory of natural selection. The basic elements of natural genetics – crossover, mutation, and selection –

[62] For example, choosing which members of a set of possible components should be used.

are used in the genetic search procedure. The EA begins with an initial set of solutions, referred to as the population, and the solutions from that population are used along with the aforementioned operations to create a new population that will hopefully be 'better' than the old population. This process is continuously repeated with the ultimate goal of obtaining the global optimum.

Leyland [68] provides a brief discussion of the terminology used in EAs which essentially describes how they operate. A population of individuals (possible solutions to the problem) is evolved toward the solution of an optimization problem by means of operations (mentioned above) on the population which produce new individuals and also by removing unpromising individuals from the population. The population evolves toward a better solution essentially by how the operators act on the population and how the individuals are removed from the population. As previously noted, crossover and mutation are two natural genetic processes. Crossover involves selecting two (or more) individuals from a population and creating a child (or children) that is some way resembles it parents (selected individuals). The parents can be chosen from the better parts of the population to ensure the children reflect the best of the current population. The 'better' parts of the population are determined from the fitness of an individual, i.e. the more suitable they are the better chances they have of reproducing. The fitness can often be a direct reflection of an individuals objective function value. Diversity – the spread of a population in the search space- is a characteristic of the population which assures that the algorithm does not converge too quickly and get trapped in a local (non-global) optimum.

Generational, elitist, and steady-state EAs are three ways an individual can be removed from a population. The population is processed a generation at a time in generational EAs, i.e. a number of children equal to the size of the population is generated and completely replace the existing population. In elitist EAs, the generation structure is generally retained, however, a few of the very best individuals in the population are also retained from generation to generation. Finally, steady-state EAs remove the generation structure of the algorithm and individuals are added to and removed from the population as necessary; often based upon some form of elitism.

In general, properly conditioned EAs are robust optimizers that will solve most classes of problems and, if given enough time, will find a good solution to almost any problem. Additionally, EAs require no supplementary knowledge of the solution space (i.e. derivatives) and require no initial 'guess' of the decision variables, whereas gradient-based methods do

require knowledge of derivatives and a 'baseline' set of decision variables values. Since EAs work with a population of potential solutions, a single optimization run can return a range of solutions, illustrating either a range of separate choices in a multi-modal problem or illustrating a trade-off between objectives in a multi-objective problem [69]. One drawback to EAs is that they tend to be computationally expensive (i.e. require long convergence times) and an optimization problem, if it is not difficult to solve, can be solved quicker by gradient-based methods; provided, of course, that it can solve it at all which oftentimes is not the case. Another possible drawback to EAs is that multiple runs of the same optimization problem will often result in different solutions to the problem due to the random nature of the search process. This, however, can be overcome to a large extent by coupling the EA to a gradient-based method which takes the solution developed by the EA and converges it towards the "global" solution. This is the approach which was used in Munoz and von Spakovsky [32] and in Rancruel and von Spakovsky [27, 28] with great success. Unfortunately, due to software integration and license issues, it was not possible to couple the two types of optimization algorithms in this thesis work.

5.2.2 MooLENI Evolutionary Algorithm

The optimization tool implemented in this work is MooLENI, or more specifically, the queueing multi-objective optimizer (QMOO). QMOO is an EA developed by Geoff Leyland and Adam Molyneaux at the Laboratoire d'Energetique Industrielle (Laboratory of Industrial Energy Systems, LENI) at the Ecole Polytechnique Federale de Lausanne (EPFL). QMOO was developed at LENI for the optimization of energy conversion system problems.

QMOO is a steady-state EA; individuals are added to the population when they are ready and are removed from the population when they are found lacking. QMOO is extremely elitist – it has a single population that contains only the best individuals found thus far. Therefore, QMOO converges rapidly but has trouble preserving diversity. To preserve diversity, QMOO divides the population into groups in parameter space and then allows these groups to evolve somewhat independently. QMOO also uses cluster analysis techniques to identify separate local optima simultaneously and to also give it a higher chance of finding the global optimum. Additionally, QMOO uses an algorithm flexible queue-based structure which makes it easy to parallelize. Finally, QMOO is a rapid and robust optimizer that requires little tuning to the specific problem at hand.

To obtain a more detailed description of the QMOO algorithm, acquire more information of evolutionary algorithms, or to see various applications of QMOO, the reader is referred to the doctoral dissertation of Geoff Leyland [69].

5.2.3 QMOO Test Problem

To demonstrate the operation of QMOO, a rather simple test problem is conducted using a rather complex objective function. The test problem used here is known as the Woods function and is considered an appropriate function when testing, for example, the robustness and speed of algorithms of this nature. The optimization problem is defined as follows:

$$\text{Minimize } f(\bar{x}) = 100\left(x_2 - x_1^2\right)^2 + (1-x_1)^2 + 90\left(x_4 - x_3^2\right)^2 + (1-x_3)^2$$
$$10.1\left[(x_2-1)^2 + (x_4-1)^2\right] + 19.8(x_2-1)(x_4-1) \qquad (5.5)$$

$$\text{where } -50 \le x_1, x_2, x_3, x_4 \le 50 \qquad (5.6)$$

It is apparent from a quick examination of the Woods function that the minimum value of $f(\bar{x})$ is 0 when $x_1 = x_2 = x_3 = x_4$. QMOO was executed three times for the Woods test problem and was discontinued when the objective function value became less than $f(\bar{x}) = 10^{-5}$. The results of the three optimizations are given in Table 5-2 and a contour plot of the Woods function is given in Figure 5-2 to display the optimal region. QMOO performed quite well in optimizing the Woods function: however, it did require a varying amount of function evaluations to arrive below the above limit. The optimizations took approximately 30 seconds to 1 minute on a 2.79 GHz Pentium 4 processor with 512 MB of RAM.

Table 5-2. Woods function optimization results.

Run	Evaluations	$f(x)$	x_1	x_2	x_3	x_4
1	15,000	4E-6	1.0004	1.0008	0.9995	0.9992
2	11,700	8E-6	0.9999	0.9997	1.0000	1.0003
3	3,500	8E-6	1.0002	1.0003	1.0002	1.0003

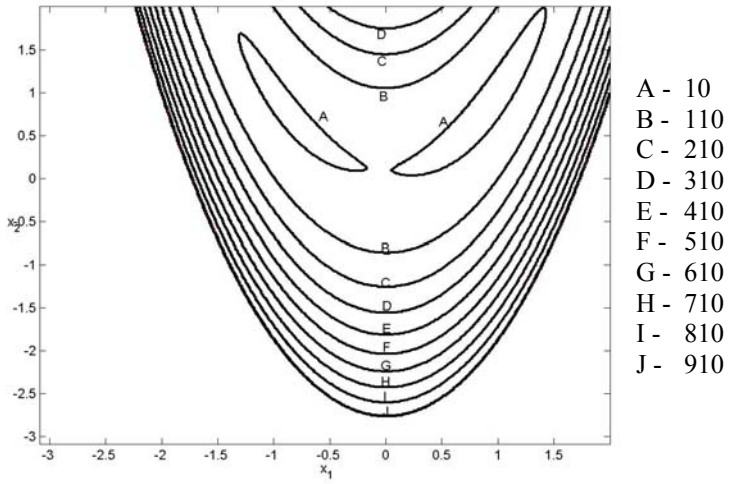

Figure 5-2. Woods function contour plot with $x_3 = x_4 = 1$.

5.3 Design Problem Simulation and Coupling to EA

The mathematical models (component models) for this work are coded using MATLAB software and make extensive use of function m-files in the programming. The optimization software MooLENI is also coded in MATLAB. A single simulation of the hypersonic vehicle model on a 2.79 GHz Pentium 4 processor with 512 MB of RAM requires anywhere from 10 to 30 seconds to complete depending on whether an accelerator or cruise vehicle is being throttled.

The hypersonic vehicle model and QMOO are coupled such that the optimizer generates values of the decision variables and then passes them to the vehicle model where, if all constraints are satisfied, an objective function value is calculated and passed back to the optimizer[63]. If a constraint is violated anywhere throughout the hypersonic vehicle model, the objective function is set to an extreme value so that the optimizer recognizes that the combination of decision variables is undesirable. The 7 design decision variables implemented in this work are $X_{fb}, X_{cowl}, X_{ramp1}, L_{comb}, \theta_{fb}, \theta_{nozz}, and\ \%_{cowl}$ and the 2 operational decision variables which vary from one mission segment to another are $\alpha\ and\ S_{wing}$ (refer to the component models for descriptions). The limits placed upon the design and operational decision

[63] Note that the objective function is the only value passed to the optimizer, i.e. the optimizer has knowledge of only the decision variable values and the corresponding objective function values.

variables during the optimizations conducted in this thesis work are presented in Tables 5-3 and 5-4.

Table 5-3. Design decision variables and limits.

Decision Variables	Imposed Limits
X_{fb}	$0.35L_{veh} \le X_{fb} \le 0.65L_{veh}$
X_{cowl}	$0.45L_{veh} \le X_{cowl} \le 0.77L_{veh}$
X_{ramp1}	$0.02L_{veh} \le X_{ramp1} \le 0.33L_{veh}$
L_{comb}	$0.02L_{veh} \le L_{comb} \le 0.33L_{veh}$
θ_{fb}	$1^\circ \le \theta_{fb} \le 6^\circ$
θ_{nozz}	$8^\circ \le \theta_{nozz} \le 18^\circ$
$\%_{cowl}$	$0 \le \%_{cowl} \le 0.25$

Table 5-4. Operational decision variables and limits.

Operational Variables	Imposed Limits
α	$0.1^\circ \le \alpha \le 5^\circ$
S_{wing}	$0 \le S_{wing} \le 9.6$

The wing planform area is allowed to vary over the mission (from one segment to another) because initial optimization runs with a fixed planform area (determined from the first mission segment) resulted in no solutions even after 1 million function evaluations. The need for the wing planform area as an operational variable is most likely attributed to: (a) a hypersonic vehicle may need a morphing wing structure to successfully fly a mission or (b) more exact methods are required to predict surface forces (i.e. lift and drag).

Chapter 6

Results and Discussion

This chapter first presents the results of a preliminary analysis using exergy methods for optimal combustor length prediction. Next a number of individual hypersonic vehicle component investigations were conducted to gain insights into the hypersonic vehicle and its relation to exergy destruction. The results of those investigations are presented and discussed following the preliminary analysis. This is followed by the presentation of the propulsion sub-system optimization results which are given along with a fixed geometry propulsion sub-system analysis in order to investigate the trends of the propulsion system operating at different flight Mach numbers. Finally, individual mission segment optimizations as well as partial mission (a three segment mission) optimizations are presented and discussed, specifically looking at the use of exergy measures in the optimization of hypersonic vehicle configurations.

6.1 Preliminary Analysis Using Exergy Methods

As a first investigation into the usefulness of exergy methods for hypersonic vehicle synthesis/design, the simple design problem proposed by Riggins [9, 12] and previously discussed in Section 2.2.1 is examined. The objective of this problem is to determine the optimal combustor length of a scramjet engine which provides the best performance (i.e. thrust). The simple scramjet engine along with some parameter values used in this problem are shown Figure 6-1. The scramjet engine is comprised of an isentropic inlet and nozzle (both of the same area ratios) and a constant cross-sectional area combustor where Rayleigh heat addition takes place and there is relatively high skin friction. The heat released into the flow is some fraction of the total energy expended ($\Delta Q_{exp end}$) determined from an exponential combustion efficiency schedule (a function of combustor length). An optimal combustor length can be determined

because there is some point in which the additional heat release associated with additional combustor length is negated by the friction associated with that additional combustor length.

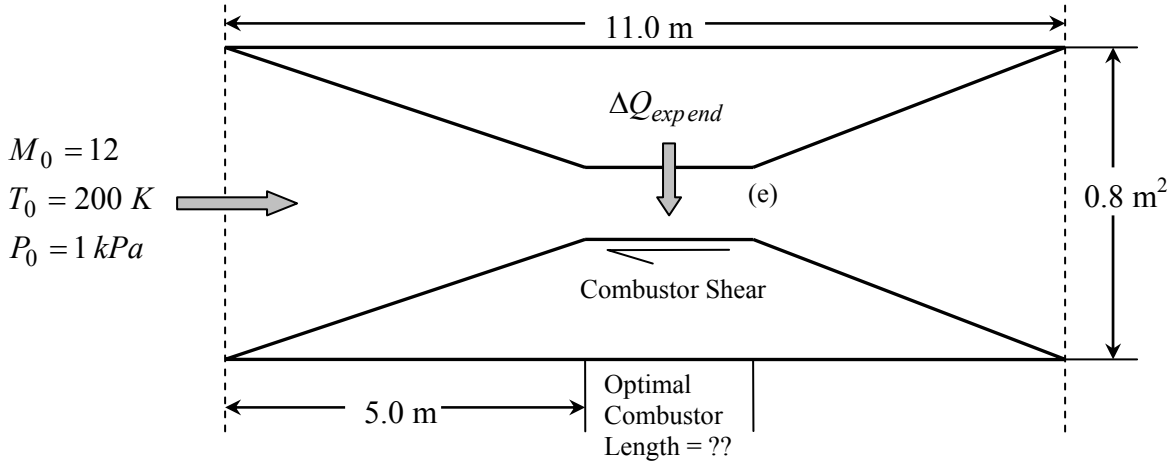

Figure 6-1. Optimal combustor length design problem

In the work done by Riggins [9, 12], a rational exergy efficiency based on earlier work by Curran and Murthy [23] and a thrust-potential based engine effectiveness were both used to predict the optimal combustor length to the above problem. It was shown that the rational exergy efficiency significantly over-predicted the optimal combustor length[64] and produced much less thrust. In this investigation, the optimal combustor length predicted by the engine effectiveness was compared to the optimal combustor length predicted by the thermodynamic effectiveness which is based upon both the 1st and 2nd Laws of thermodynamics. The thrust-potential-based engine effectiveness $\eta_{ee}(x)$ and the thermodynamic efficiency $\varepsilon(x)$ are defined respectively, as

$$\eta_{ee}(x) = \frac{\dot{m}u_e(x) + P_e(x)A_e - (\dot{m}u_0 + P_0 A_0)}{\dot{m}u_{e_{ideal}} + P_{e_{ideal}} A_e - (\dot{m}u_0 + P_0 A_0)} \tag{6.1}$$

[64] As noted in Chapter 2, the rational efficiency proposed by Curran and Murthy [23] is more appropriate for stationary engines than for aerospace engines. In fact, it is completely inappropriate for the latter.

$$\varepsilon(x) = 1 - \frac{T_0 s_{irr}(x)}{\delta Q_{release}(x)\left(1 - \frac{T_0}{T_t(x)}\right)} \tag{6.2}$$

where the term $\dot{m}u + PA$ is the streamthrust. In Equation (6.2) the entropy generated is a result of friction and Rayleigh heat addition and the heat released is once again determined from a combustion efficiency schedule. In this same equation, the denominator of the ratio on the right is the work or exergy equivalent form of the heat released. The engine effectiveness at a given station is defined as the ratio of the net engine thrust assuming an isentropic expansion process to the nozzle exit area to the net ideal engine thrust [9, 12]. The thermodynamic effectiveness is a measure of the work (exergy) required by the actual process to the largest work (exergy) available from the energy source for the process [24].

A one-dimensional code was developed to model the design problem making use of isentropic flow relations, total temperature and pressure relations (Equations (3.11) and (3.12)), and the one-dimensional governing equations (Equations (3.5) to (3.8)). The flow properties predicted by the equations in this model were in good agreement with the flow properties predicted by a model developed by Riggins [58]. A comparison of the flow properties throughout the scramjet engine with a 1.0 m length combustor ($5 < x < 6$) is made between the two models in Table 6.1.

The good agreement of these properties allows an exact prediction of the optimal combustor length using the engine effectiveness as suggested by Riggins [9, 12]. Figure 6-2 shows that the engine effectiveness predicts an optimal combustor length of $L_{comb_{opt}} = 0.46\ m$ with a corresponding thrust of 5950 N. Figure 6-2 also shows that the thermodynamic effectiveness described by Equation (6.2) very nearly predicts the same optimal combustor length and thrust. The optimal combustor length is found to be $L_{comb_{opt}} = 0.44\ m$ using the thermodynamic effectiveness and the thrust is 5948 N. This result demonstrates, as an initial investigation, that exergy methods may indeed have some promise in hypersonic vehicle synthesis/design and furthermore demonstrates the inappropriateness of the rational exergy efficiency proposed by Curran and Murphy.

Table 6.1 Comparison of optimal combustor models.

	Riggins Model Based on η_{ee}					Thesis Model Based on ε		
x (m)	M	T (K)	P (N/m^2)	u (m/s)	M	T (K)	P (N/m^2)	u (m/s)
0	11.97	200	1000	3400	12	200	1000	3402.3
5.0	6.22	679	70900	3255.4	6.26	674.4	70417	3259.2
6.0	1.72	4346	647223	2283	1.73	4342	645804	2288.3
11.0	5.12	1107	5496	3423	5.11	1115.2	5541	3423.9

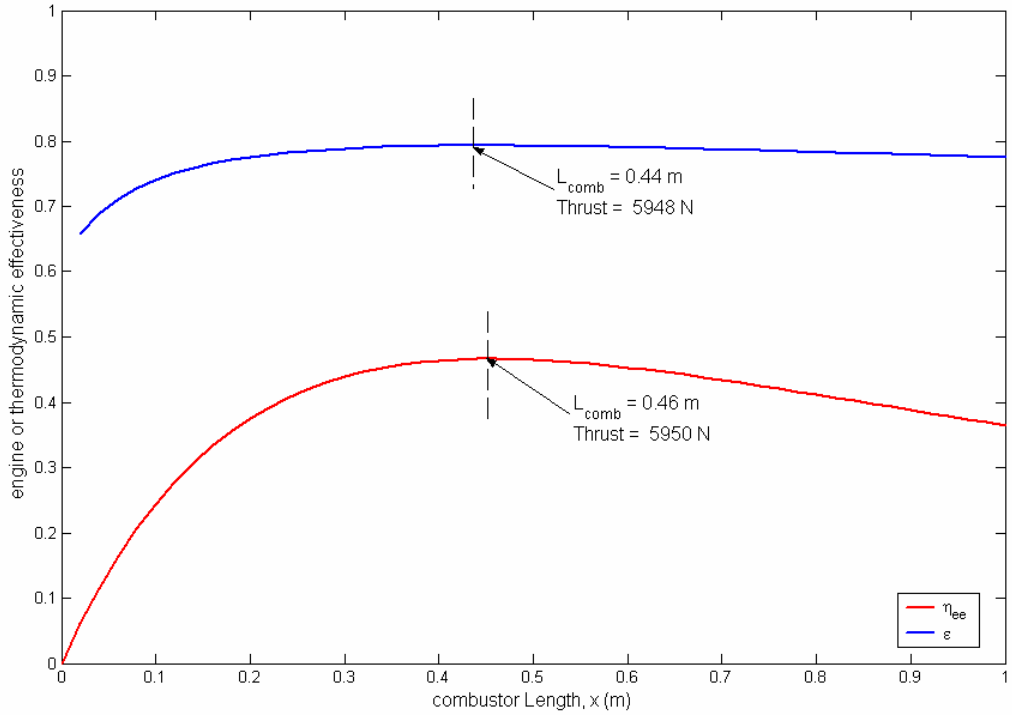

Figure 6-2. Optimal combustor lengths predicted by engine and thermodynamic effectiveness.

6.2 Hypersonic Vehicle Component Parametric Studies

An assortment of hypersonic vehicle component investigations were conducted to provide insights into the relationship between the design decision variables and the rate of exergy destruction and thrust as well as other performance measures. The rate of exergy destruction is directly proportional to the rate of entropy generation (i.e. irreversibility) and is given by the Gouy-Stodola theorem as

$$\dot{E}x_{des} = T_0 \dot{S}_{irr} \tag{6.3}$$

where the proportionality factor T_0 is simply the "dead state" (environment) absolute temperature[65] [65]. It is worth mentioning that the results presented in this section are a reflection of the methods chosen to model each component and, therefore, different hypersonic vehicle models may produce varying results. However, this does not undermine the fact that much knowledge can be gained from these parametric studies.

Specific thrust[66] versus specific exergy[67] destruction as a function of the design decision variables is plotted in Figures 6-3 to 6-5. For these trade studies, the flight Mach number and the design Mach number were fixed at 9, i.e. no energy exchange with the freestream flow occurred. Table 6-2 displays the values of the design decision variables used in these studies as well as the respective ranges over which they were varied. The ranges of the the forebody deflection angle and the first ramp length were limited to those specified in Table 6-2 in order to avoid violating the constraints imposed upon the inlet component, i.e. minimum/maximum inlet exit Mach number, minimum inlet exit pressure, etc. The forebody length and cowl position were not varied because: (a) it was difficult to find a range for which these variables, in combinations with each other and the other inlet design decision variables, satisfied all inlet constraints (with the remaining design decision variables fixed) and (b) no observable trends occurred when these variables were varied in conjunction with each other or another inlet design decision variable.

Table 6-2. Design decision variable fixed values and ranges for component audits.

Design Variable	X_{fb}	X_{cowl}	X_{ramp1}	θ_{fb}	α	θ_{nozz}	L_{comb}	$\%_{cowl}$
Fixed Value	8.4	13.5	2.75	2.0	1.0	18.0	0.5	0.125
Range	—	—	2.7 – 3.5	1.75 – 6.25	—	8.0 – 18.0	0.5 – 1.5	0 – 0.25

[65] Once again it is noted that the "dead state", from a thermodynamic point of view, does not have to "float" for aerospace applications because the "dead state" is only a reference state which means that the value of "exergy" as any thermodynamic property can only be determined in relative terms, i.e. relative to a reference state.
[66] Specific thrust is the thrust divided by the mass flow rate of air.
[67] Specific exergy destruction is the rate of exergy destruction divided by the mass flow rate of air.

Figure 6-3 displays the effect that the forebody angle and first ramp length have on the specific thrust and the specific exergy destruction of the propulsion sub-system. In this figure, the point of greatest temperature and pressure ratio and lowest inlet exit Mach number occurs at $\theta_{fb} = 6.5, X_{ramp1} = 3.5$ and the point of smallest temperature and pressure ratio and largest inlet exit Mach number occurs at $\theta_{fb} = 1.75, X_{ramp1} = 2.7$. It is apparent that, at a fixed θ_{fb}, an increase in X_{ramp1} produces an increase in specific thrust and an appreciable increase in specific exergy destruction. Figure 6-3 also shows that at the longest X_{ramp1}, an increase in θ_{fb} results in a decrease in specific exergy destruction. However, as X_{ramp1} becomes smaller, the affect of a decrease in specific exergy destruction from an increase in θ_{fb} becomes less (even to the point where an increase in specific exergy destruction occurs). Finally, Figure 6-3 reveals: (a) two different geometries produce that same specific thrust; however, one destroys more specific exergy than the other and (b) the geometry producing the largest specific thrust does not produce the largest specific exergy destruction.

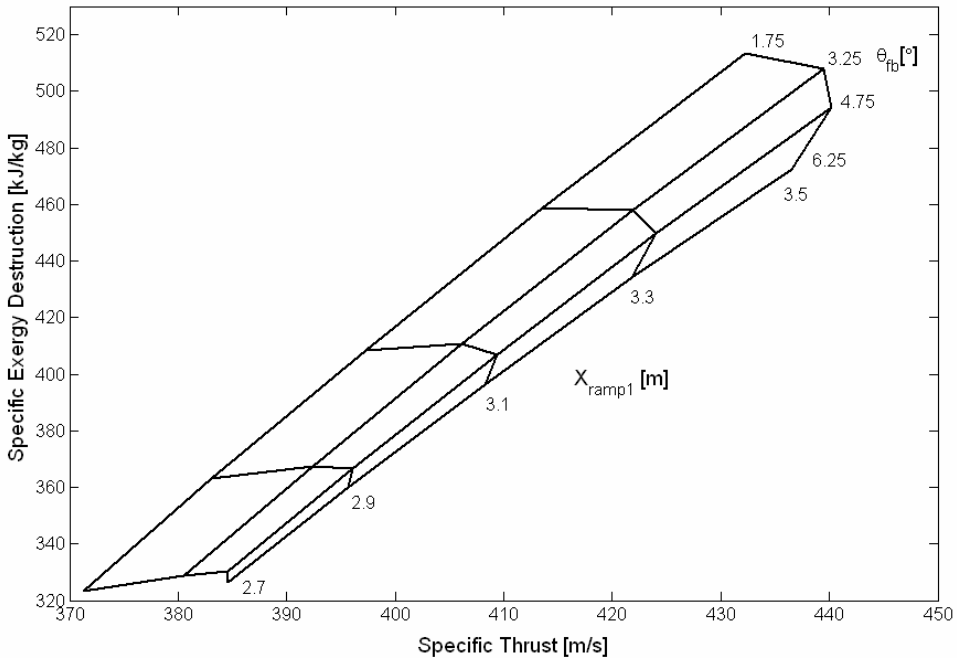

Figure 6-3. Specific exergy destruction versus specific thrust for a range of ramp lengths and forebody angles with the fixed design decision variables values listed in Table 6-2.

Figures 6-4 and 6-5 demonstrate the effects of combustor length, nozzle expansion angle, and percent cowl on the specific thrust and propulsion sub-system specific exergy destruction. As one would expect, an increase in L_{comb} causes a substantial increase in the specific exergy destruction. In addition, an increase in L_{comb} (for a given θ_{nozz}) produces an increase in specific thrust because a longer combustor permits a more complete combustion which, in turn, allows for greater expansion through the nozzle (since the Mach number is closer to 1). Therefore, from the standpoint of Figure 6-4, it appears beneficial to have the shortest combustor and the largest θ_{nozz} to produce a given specific thrust. Also, from these figures, it is apparent that θ_{nozz} and $\%_{cowl}$ have minimal influence on the propulsion system specific exergy destruction. A larger θ_{nozz} produces a larger specific thrust while a smaller $\%_{cowl}$ produces a larger specific thrust. Although it may seem best to operate the vehicle without any cowl extension into the nozzle, an extension may be needed to help reduce the large nozzle surface forces and moments inflicted upon the vehicle. This trend is shown in Figure 6-6 where the larger cowl extensions act to counterbalance the surface forces and moments.

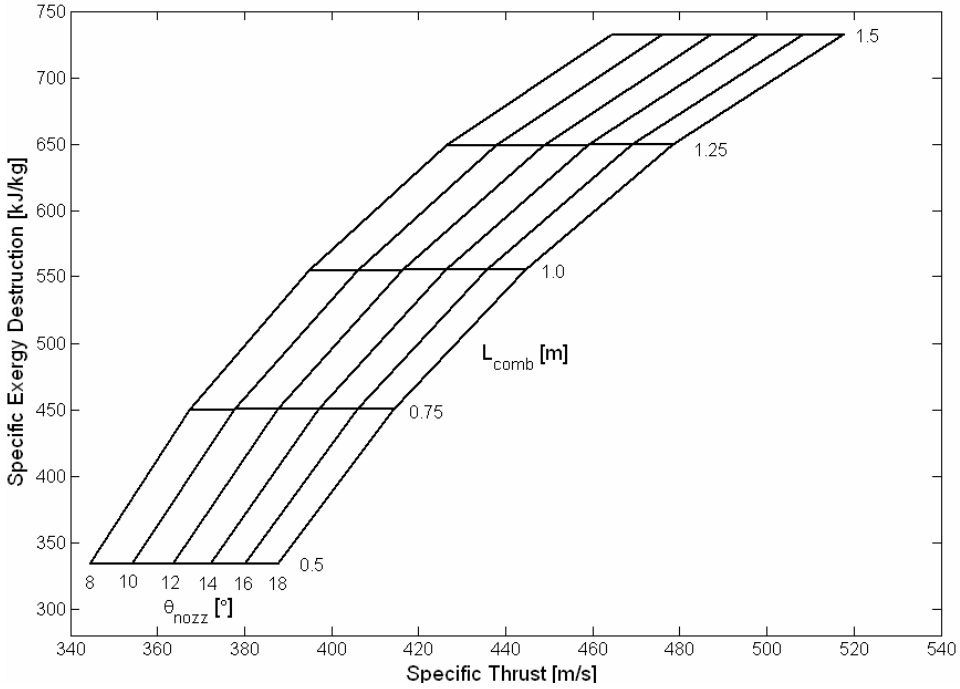

Figure 6-4. Specific exergy destruction versus the specific thrust for range of combustor lengths and nozzle expansion angles with the fixed design decision variable values listed in Table 6-2.

The inlet compression efficiency and inlet kinetic energy efficiency are plotted with the specific exergy destruction as a function of forebody angle and ramp length in Figures 6-7 and Figure 6-8. Kinetic energy efficiency and compression efficiency are defined in Equations (3.30) and (3.31), respectively. From examining Figure 6-7, it appears that at a given θ_{fb}, it would be more reasonable to have a smaller X_{ramp1} because there is not much gain in compression efficiency with a longer X_{ramp1} while there is a rather large increase in specific exergy destruction. Of course, this all depends on the thrust demands of the hypersonic vehicle (refer to Figure 6-3).

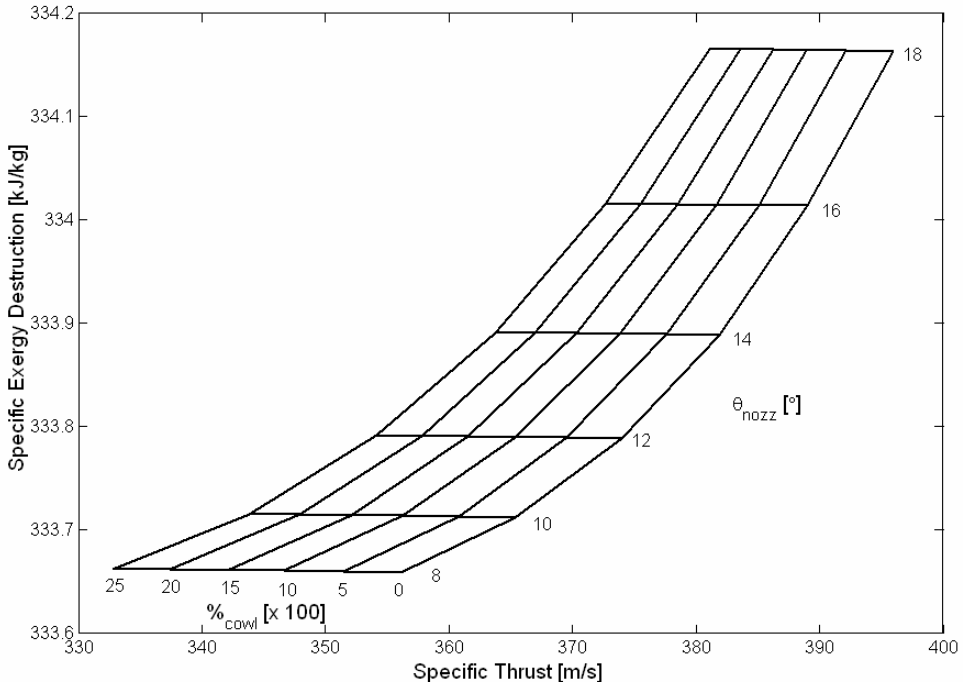

Figure 6-5. Specific exergy destruction versus the specific thrust for a range of nozzle expansion angles and percent cowl lengths with fixed design decision variable values listed in Table 6-2.

Figure 6-8 also reveals that a smaller X_{ramp1} for a given θ_{fb} is more desirable in terms of kinetic energy efficiency. Also, shown in Figure 6-8 is the fact that at $\theta_{fb} = 3.25^{\circ}$ the largest kinetic energy efficiency occurs for all ramp lengths. Although the scale depicted for the kinetic energy efficiency may seem inconsequential, small changes in the kinetic energy efficiency represent rather appreciable changes in inlet performance. A conclusion to be drawn from Figures 6-3 and 6-7 is that for certain required vehicle specific thrust the combination of the

smallest X_{ramp1} and the largest θ_{fb} that can produce the required specific thrust is most desirable to minimize the specific exergy destruction and maximize the compression efficiency.

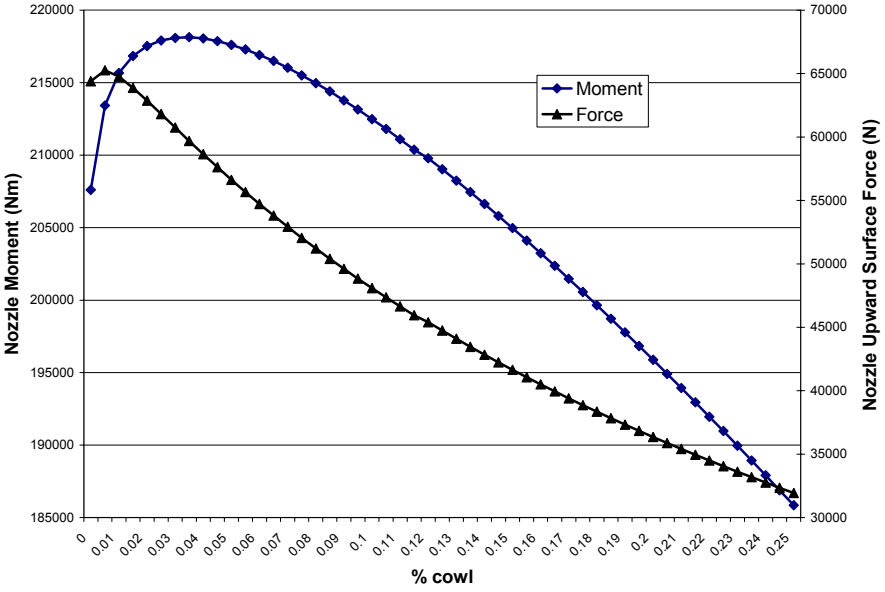

Figure 6-6. The effect of design decision variable $\%_{cowl}$ on nozzle upward surface force and nozzle moment.

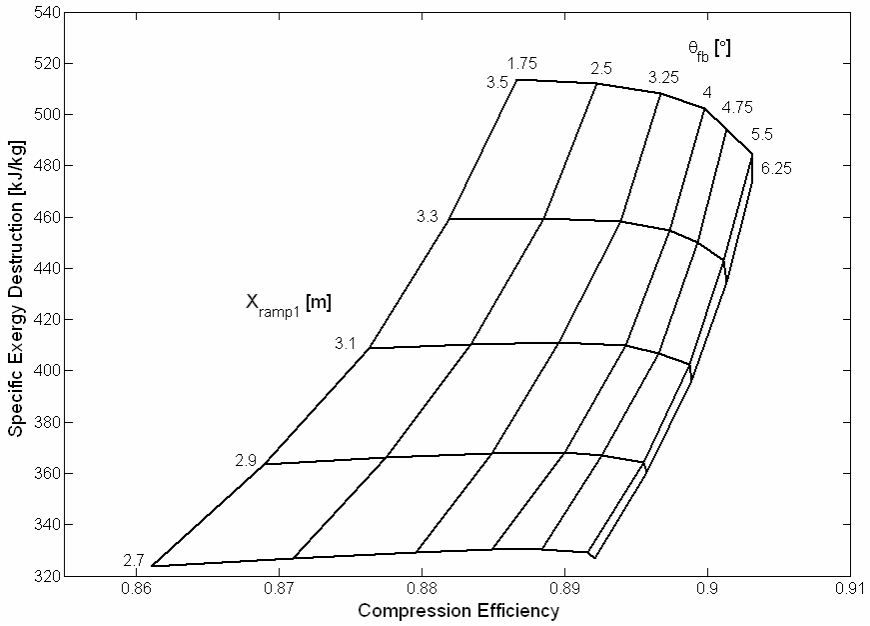

Figure 6-7. Specific exergy destruction versus the compression efficiency for a range of ramp lengths and forebody angles with the fixed design decision variable values listed in Table 6-2.

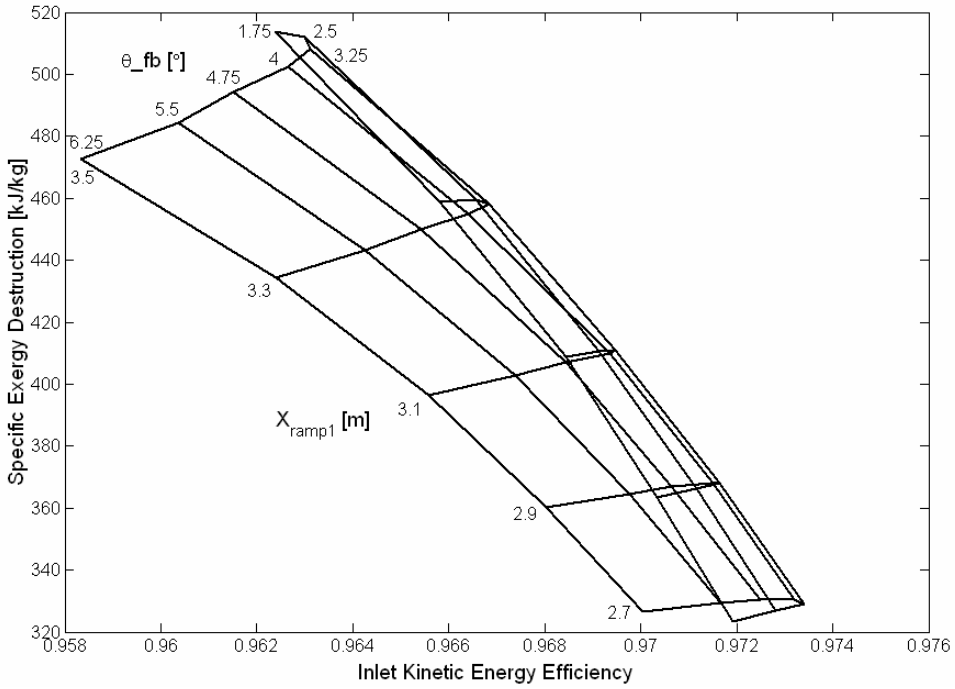

Figure 6-8. Specific exergy destruction versus the kinetic energy efficiency for a range of ramp lengths and forebody angles with the fixed design decision variable values listed in Table 6-3.

A final component parametric study investigated the effects of combustor entrance temperature and pressure on the loss mechanisms in the combustor. A fixed combustor length and height were implemented in this study as well as a fixed equivalence ratio of $\phi = 0.8$. The temperature and pressure were varied over the following ranges:

$$1000\ K \le T_5 \le 2000\ K \qquad 60{,}000\ N/m^2 \le P_5 \le 400{,}000\ N/m^2$$

Figure 6-9 shows the rate of exergy destroyed by the four combustor irreversible loss mechanisms: friction due to wall and injector drag, heat transfer across a finite temperature difference, the mixing of air and fuel, and non-equilibrium incomplete combustion. It is shown that the rate of exergy destruction is a strong function of the combustor entrance pressure P_5 for all four irreversible loss mechanisms and that the rate of exergy destruction is only a slight function of combustor entrance temperature T_5 for all loss mechanisms except heat transfer. The rate of exergy destruction essentially increases linearly with P_5 for friction, mixing, and non-equilibrium losses. However, the rate of exergy destruction due to heat transfer increases rapidly with both increasing temperature and pressure. Therefore, the largest rate of exergy

destruction due to heat transfer occurs at the highest combustor entrance temperature and pressure (as expected from the combustor wall heat loss model of Section 4.1.2). Figure 6-9 also reveals that non-equilibrium incomplete combustion losses are by far the most dominant loss mechanism and heat transfer losses destroy the least rate of exergy.

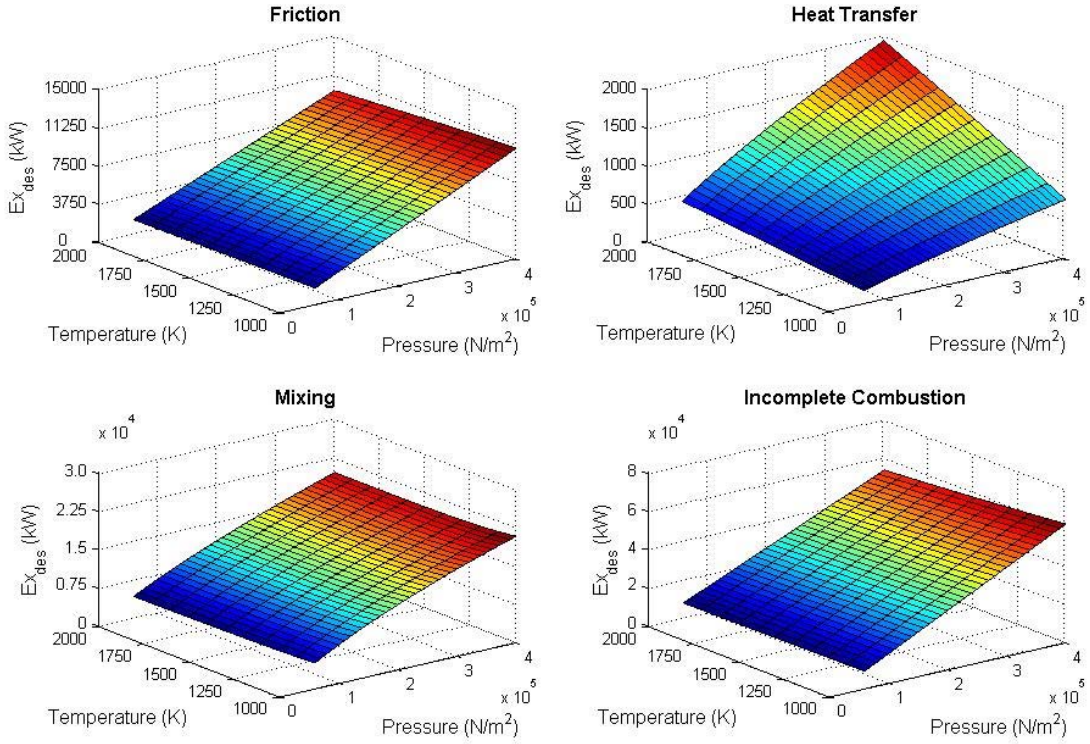

Figure 6-9. Rate of exergy destroyed by combustor loss mechanisms at M_5 = 3.2 and over a range of combustor entrance temperatures (T_5) and pressures (P_5). Molecular weights and specific heat ratio are fixed.

The results shown in Figure 6-9 are for a combustor entrance Mach number of $M_5 = 3.2$. The aforementioned process was repeated for combustor entrance Mach numbers of $M_5 = 2.7$ *and* 3.7 as well and produced results exactly similar to those shown in Figure 6-9 except that magnitude of the exergy destruction rates varied (smaller at 2.7, larger at 3.7).

As mentioned in Section 4.1.2, the combustor model developed for this thesis does not include the affects of molecular weight changes and specific heat ratio changes as more fuel is being burned. Therefore, it was deemed important to account for molecular weight and specific heat ratio changes in the combustor model in order to make comparisons of the flow properties

and irreversibilities with the combustor model that does not consider these changes. In order to account for molecular weight and specific heat ratio changes and also their affects on the flow properties, the mole fractions of each constituent in Equation (4.23) were calculated at each combustor differential step and two additional terms were added to Equations (4.28) to (4.30) (refer to [43]).

The above parametric study was repeated with molecular weight and specific heat ratio changes in the combustor model for the same combustor geometry, equivalence ratio, and combustor entrance ranges of temperature and pressure. The results of this study are shown in Figure 6-10 where exergy destruction rates are once again plotted versus temperature and pressure.

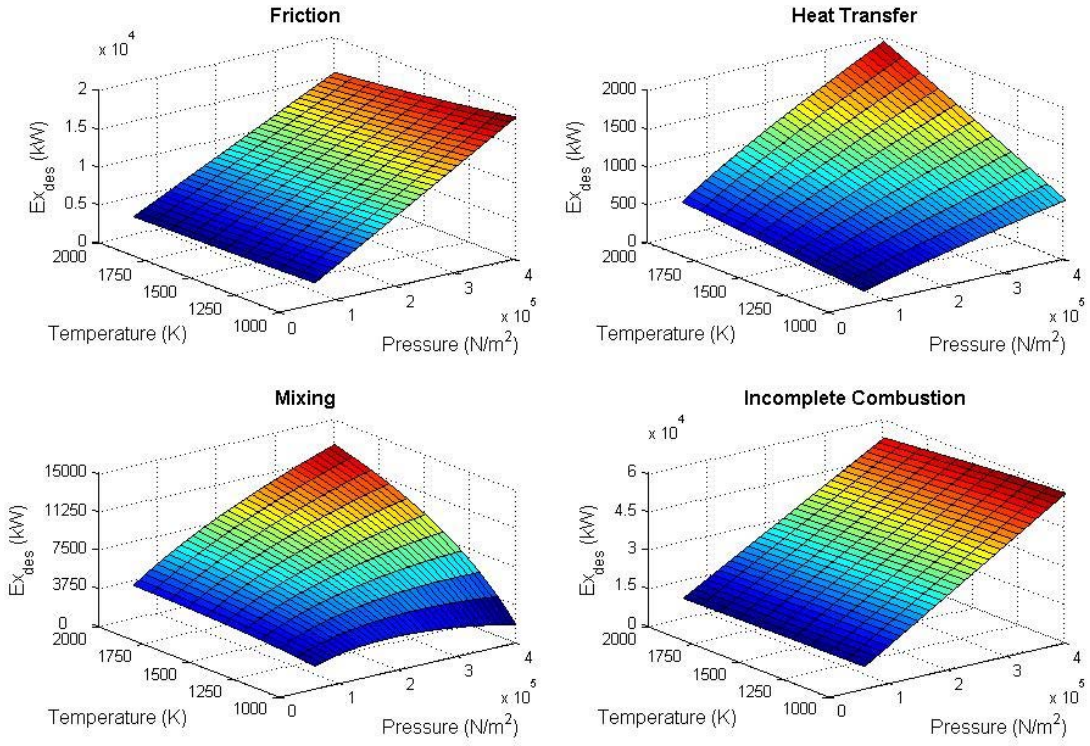

Figure 6-10. Rate of exergy destroyed by combustor loss mechanisms at M_5 = 3.2 and over a range of combustor entrance temperatures (T_5) and pressures (P_5). Molecular weight and specific heat ratio changes are included in the combustor model.

As shown in Figure 6-10, the rates of exergy destruction due to friction and non-equilibrium incomplete combustion increase linearly with pressure and are only slightly affect by

temperature. This happens to be the same trend previously depicted in Figure 6-9 for friction and non-equilibrium incomplete combustion losses. It appears from a comparison of Figures 6-9 and 6-10 that accounting for molecular weight and specific heat ratio changes results in an increase in frictional losses and decrease in mixing losses. It can also be seen from a comparison of these two figures that heat transfer exergy destruction rates are identical for both combustor models. This is once again attributed to the combustor wall heat loss model utilized in this work. Finally, Figure 6-10 reveals that exergy destruction rates due to fuel/air mixing are affected significantly by the inclusion of molecular weight and specific heat ratio changes in the combustor model. At higher combustor entrance temperatures, the trend is essentially the same as that shown in Figure 6-9; but as T_5 decreases an increase in P_5 tends to have a less significant affect on the exergy destruction rates. In fact, at a low T_5 there is not much difference in exergy destruction rates for mixing at low or high P_5.

To further investigate this issue, three sets of combustor entrance properties (station 5) were applied to a constant geometry and constant equivalence ratio combustor in order to observe the influence molecular weight and specific heat ratio changes had on combustor exit flow properties (station 6) and irreversibilities (i.e. entropy generation). The results of this investigation are displayed in Table 6-3 where combustor B accounts for molecular weight and specific heat ratio changes in the model. It can be seen that for all three sets of combustor entrance conditions there are appreciable differences in the exit properties of the two combustor models. From Table 6-3 it appears that a larger combustor entrance pressure results in a larger difference between the exit pressures for combustors A and B. It is also evident from Table 6-3 the modifications applied to combustor model B result in significant changes to the entropy generation rates from friction and mixing and these changes become more pronounced as the combustor entrance Mach number increases. Combustor model B has only slight differences in entropy generation rates due to non-equilibrium combustion compared to combustor model A and there is no difference in entropy generation rates due to heat transfer between the two models. In the end, combustor model B predicts about 5-10% smaller entropy generation rates than combustor model A. Also, it can be concluded that a longer combustor for model B is needed to obtain relatively similar combustor exit flow properties as determined from combustor model A.

Table 6-3. Combustor affects due to molecular weight/specific heat ratio changes.

	Station	Comb. A	Comb. B	Comb. A	Comb. B	Comb. A	Comb. B
M	5	2.5	2.5	3.2	3.2	3.9	3.9
	6	1.171	1.660	1.567	2.009	1.751	2.241
T (K)	5	1700	1700	1400	1400	1100	1100
	6	3222.8	2816.8	3089.4	2733.2	3020.5	2614.6
P (N/m^2)	5	300000	300000	225000	225000	150000	150000
	6	895240	558950	692880	482760	561720	389360
u (m/s)	5	1995	1995	2318	2318	2504	2504
	6	1288.1	1889.9	1693.9	2252.7	1882.7	2460.1
Irreversibilities S_{irr} (kW/K)	Friction	18.07	31.396	30.079	50.452	36.794	61.769
	HT	4.294	4.294	4.305	4.305	3.452	3.452
	Mixing	64.742	40.659	72.952	38.272	74.01	30.235
	Inc. Comb.	181.79	177.17	184.99	180.09	161.72	155.63

The accuracy achieved with combustor model B is not without drawbacks. Each combustor computation took approximately 0.5 seconds longer for combustor model B on a single AMD Athlon 2.08 GHz processor with 992 MB of RAM. This doesn't present much of a problem for single point analysis. However, it may cause an additional computational burden during optimizations because of the sheer number of runs (discussed shortly) and also because of the throttling process of the vehicle.

6.3 Scramjet Engine Only Optimizations and Study

A study of a fixed geometry scramjet engine was conducted over a range of flight Mach numbers in order to gain insights into the operation of the scramjet engine and the exergy destruction of the propulsion sub-system components. This study investigated both a scramjet engine that implemented energy exchange (see Section 4.1.1) with the freestream flow to maintain the shock-on-lip condition and a scramjet engine with no energy exchange which accounted for mass flow spillage at Mach numbers below the design value.

An approximation was utilized to determine that last streamline captured by the inlet and calculate the mass flow spillage. First, the sum of the forebody and two ramp angles was averaged to obtain an average flow angle. Next, a line was traced forward from the cowl lip at the average flow angle until it intersected the forebody oblique shock (refer to Figure 3-15). Finally, the area A_0 was calculated which ultimately allowed for the calculation of the mass flow spillage.

The scramjet engine used in this study operated at an equivalence ratio of $\phi = 0.8$ and a design Mach number of $M_{design} = 9$. Additionally, the flight Mach number range was $M_0 = 7\ to\ 11$. The results of the analysis of the scramjet engine with and without energy exchange are given in Table 6-4 and Figures 6-11 and 6-12.

Table 6-4. Scramjet engine with and without energy exchange.

	M_0	M_5	T_5 (K)	P_5 (N/m^2)	Thrust (N)	$\dot{m}_{air}$ (kg/s)	Spillage (kg/s)	$Q^{\leftarrow}$ (J/kg)
Energy Exchange	7	3.458	688.4	132130	92577	159.13	—	-61751
	8	3.458	899.9	132080	68951	139.12	—	-33083
	9	3.458	1141.6	131760	53061	123.22	—	0
	10	3.458	1413.8	130160	41993	109.38	—	37504
	11	3.458	1716.3	129960	34444	99.128	—	79430
No Energy Exchange	7	3.133	808.4	106540	60758	108.81	50.32	—
	8	3.343	953.3	114140	54921	113.5	25.26	—
	9	3.458	1141.6	131760	53061	123.22	—	—
	10	3.726	1259.6	115210	41795	109.38	—	—
	11	3.952	1392.2	104250	33810	99.128	—	—

The combustor entrance Mach number, temperature, and pressure for both the scramjet engine with and without energy addition are given in Table 6-4. It shows that the scramjet engine with energy exchange ($\dot{Q}^{\leftarrow}$) maintains the same M_5 for all flight Mach numbers (due to the same inlet shock structure) and allows a small variation in P_5. This may be beneficial

from the standpoint that a scramjet combustor could be designed to operate for specific entrance conditions. The scramjet engine that permits mass flow spillage has an appreciable variation in both M_5 and P_5 over the flight Mach number range but has a much smaller variation in T_5 in comparison with the scramjet engine with energy exchange.

Table 6-4 also shows that at flight Mach numbers below the design value there are significant losses in thrust due to mass flow spillage (which is approximately 30% of the maximum capture value at $M_0 = 7$). However, at $M_0 = 7$ *and* 8 there is power required to operate some 'device' in order to exchange the required $\dot{Q}^{\leftarrow}$ which could negate some of the additional thrust power achieved by using this device. For example, the thrust power at $M_0 = 7$ for the scramjet with energy exchange is $P_{thrust} = 193{,}856\ kW$ and equals $P_{thrust} = 127{,}227\ kW$ for the scramjet without energy exchange. At this flight Mach number, the additional amount of fuel required to operate this device is calculated from

$$\dot{m}_f ex_f = \dot{m}_{air} 2Q^{\leftarrow}\left(1 - \frac{T_0}{T_{0b}}\right) \tag{6.4}$$

where the exergy content of hydrogen fuel is $ex_f = 116{,}575\ kJ/kg$ and it is assumed in Equation (6.4) that twice as much energy is needed to operate the device as that being exchanged with the flow (for illustration purposes). Therefore, the power required to operate the device is determined to be $P_{device} = 12{,}467\ kW$. One can, thus, be concluded that even though power is needed to operate the device there is still a rather large benefit in terms of thrust power produced for the scramjet engine with energy exchange.

At flight Mach numbers above the design value there is not much gain in thrust using the energy exchange (while the device consumes power). However, this analysis did not account for effects on the combustor from shock ingestion. Therefore, it may or may not be beneficial to utilize energy exchange with the freestream flow at flight Mach numbers above the design value.

Figures 6-11 and 6-12 display the specific exergy destruction of each of the propulsion sub-system components for the fixed geometry scramjet with and without $\dot{Q}^{\leftarrow}$. The specific exergy destruction of the inlet remains relatively constant over the flight Mach number range for the scramjet with $\dot{Q}^{\leftarrow}$. The specific exergy destruction of the inlet is smaller without $\dot{Q}^{\leftarrow}$ than

with $\dot{Q}^{\leftarrow}$ below the design Mach number and is larger without $\dot{Q}^{\leftarrow}$ than with $\dot{Q}^{\leftarrow}$ above the design Mach number.

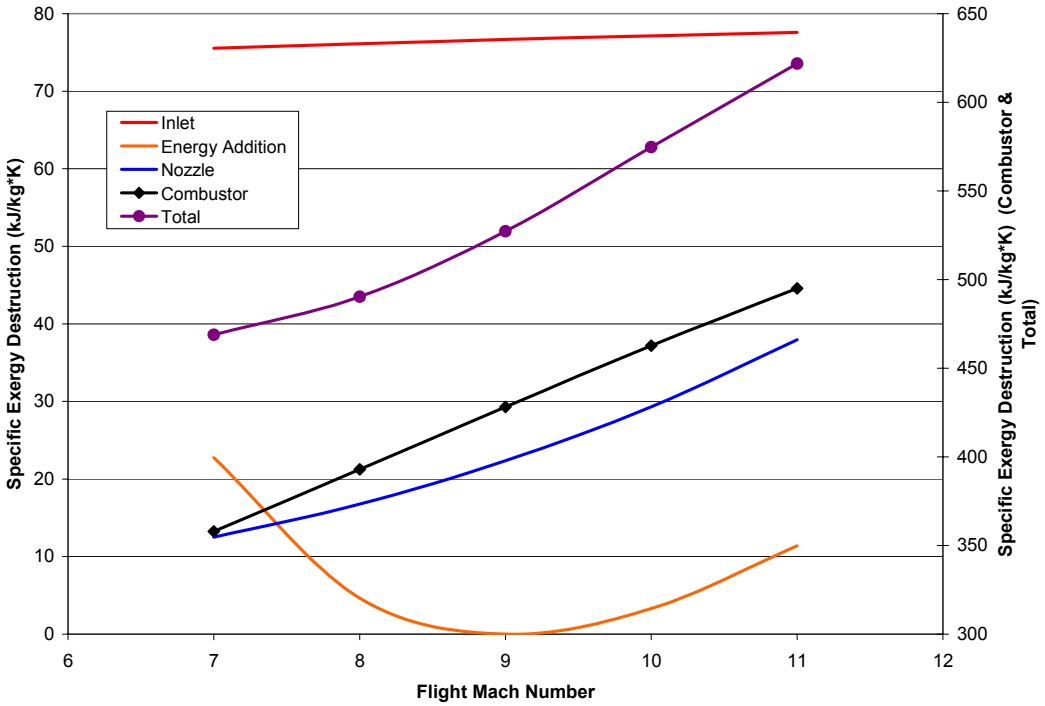

Figure 6-11. Specific exergy destruction of the propulsion sub-system components over a range of flight Mach numbers. Energy exchange included in the propulsion sub-system.

The hypersonic vehicle propulsion system (i.e. scramjet engine) was optimized at flight Mach numbers of $M_0 = 6, 8, 10, and\ 12$ and a fixed angle of attack of $\alpha = 0^\circ$ and equivalence ratio of $\phi = 0.7$. These optimizations were performed to investigate if any decision design variable or other parameter trends exist between optimal scramjet engines at different flight Mach numbers. The objective function maximized in these optimizations was the vehicle overall efficiency, defined as

$$\eta_o = \frac{Tu_0}{\dot{m}_f h_{pr}} \tag{6.5}$$

which is a standard 1st Law based efficiency and is an indicator of how well the engine uses the energy originally deposited in the fuel tanks [1]. The vehicle overall efficiency is often further broken down into a thermal and propulsive efficiency[68] defined by [1]

$$\eta_o = \eta_{th} \cdot \eta_p = \frac{(1+f)\frac{u_7^2}{2} - \frac{u_0^2}{2}}{fh_{pr}} \cdot \frac{Tu_0}{\dot{m}_{air}\left\{(1+f)\frac{u_7^2}{2} - \frac{u_0^2}{2}\right\}} \tag{6.6}$$

where f is the fuel/air ratio, u_0 is the freestream velocity, and u_7 is the velocity exiting the engine. Also, note that these optimizations assume that the design Mach number is equivalent to the flight Mach number.

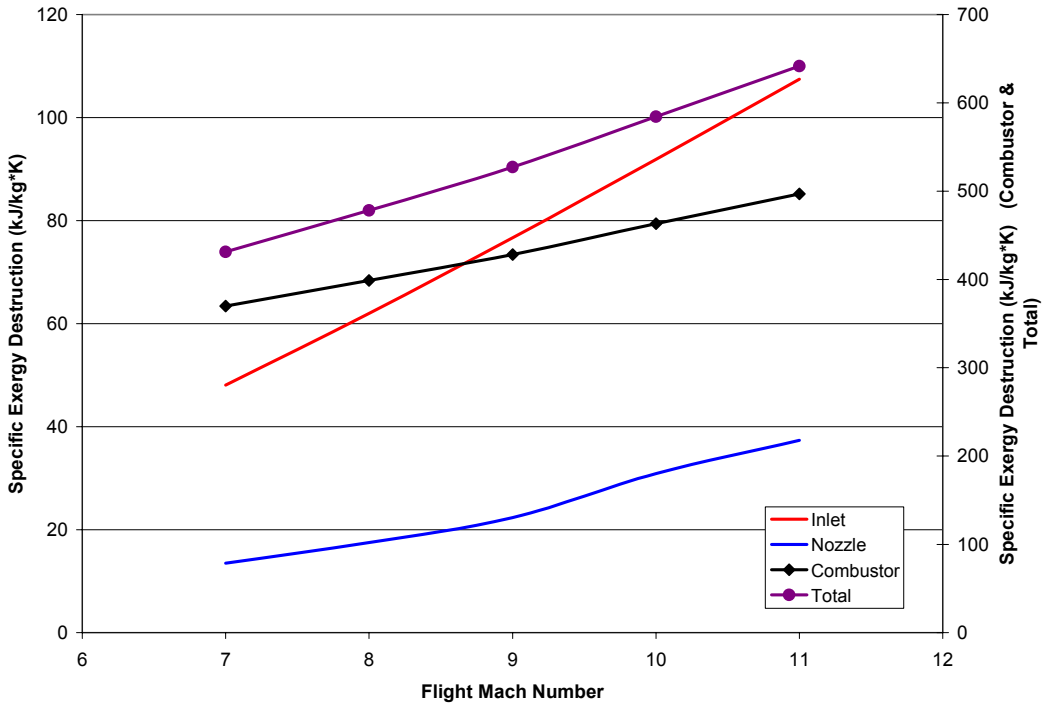

Figure 6-12. Specific exergy destruction of propulsion system components over range of flight Mach numbers. No energy exchange in propulsion system.

[68] Thermal and propulsive efficiency calculations are only given in this section. They are not given in the last two sections of this chapter because when the airframe was incorporated into the optimizations unreasonable values were obtained for these to efficiencies. This was assumed to be a result of the fact that Equation (6.6) is not completely applicable to this work (see derivation of Equation (6.6) in [1]) and possibly due to the vehicle throttling method.

Anywhere from three to five optimization runs were made for each flight Mach number depending on the precision of the objective function values. All optimizations were run to 40,000 function evaluations which took a few hours per run on a 2.79 GHz Pentium 4 processor with 512 MB of RAM. In general, per flight Mach number, each optimization resulted in relatively the same objective function value. However, the values of the design decision variables for a given Mach number were not the same for each optimal solution. An example of this is shown in Table 6-5 for the optimal Mach 10 solutions. The conclusion form this table is that there are most likely quite a few configurations that produce relatively the same objective function value (the inverse of Equation (6.5)). This implies that, for engine only optimizations, the optimizer does a fairly good job of arriving at a solution in a region more than likely near the global optimum but has trouble arriving exactly at it. This is not surprising since it is the nature of EAs to get close but not exactly there. Thus, it would be beneficial to couple a gradient-based method to the evolutionary algorithm to assist in arriving at the global optimum.

Table 6-5. Optimal Mach 10 scramjet configurations.

Run	Obj. Fun.	X_{fb}	X_{cowl}	X_{ramp1}	θ_{fb}	θ_{nozz}	L_{comb}	$\%_{cowl}$
1	1.6225	8.4730	13.208	2.8042	3.3705	18.000	1.2080	0.0059
2	1.6049	8.5737	12.864	2.5221	5.0793	17.985	1.1000	0.0005
3	1.6274	8.5120	13.169	3.2046	4.8805	18.000	0.7267	0.0014

Nonetheless, a comparison of the optimal scramjet engines was made to investigate trends and differences of design decision variables, other parameters, and exergy destruction rates. To make a fair comparison, it was assumed that the global optimum was the minimum objective function value for each flight Mach number. The results of the optimizations are shown in Table 6-6 and Figures 6-13 and 6-14.

Table 6-6 lists the optimal values of the design decision variables for the optimal scramjet engine at all four flight Mach numbers. Also listed in this table are the inlet length, overall efficiency, thrust, contraction ratio, and air mass flow rate (listed in this order in Table 6-6). Some noticeable trends for the optimal scramjet engines are as follows:

1. As M_0 increases, X_{fb} increases slightly and both X_{cowl} and X_{ramp1} decrease rather substantially (relative to its overall magnitude). Consequently, these trends result in a

decrease in inlet length (X_{inlet}) as M_0 increases. In fact, not only does the inlet length become smaller as flight Mach number increases, the entire inlet itself becomes much smaller. This can be seen in Appendix A where the optimal scramjet engine inlets at each M_0 are drawn.

2. As M_0 increases, both θ_{fb} and CR increase significantly in order to compress the higher Mach number flow to acceptable combustor entrance conditions.

Table 6-6. Optimal design decision variables and parameters for optimal scramjet engines.

	Mach Number	**6**	**8**	**10**	**12**
	Obj. Function	3.3948	1.9894	1.6049	1.4840
Design Decision Variables	X_{fb}	8.4005	8.4924	8.5737	8.7359
	X_{cowl}	16.285	13.633	12.865	12.154
	X_{ramp1}	4.4432	3.0330	2.5222	1.9822
	θ_{fb}	1.8772	2.8273	5.0794	5.3887
	θ_{nozz}	17.942	17.811	17.985	17.993
	L_{comb}	1.2519	1.1418	1.1000	1.0500
	$\%_{cowl}$	0.0001	0.0003	0.0005	0.0002
Other Parameters	X_{inlet}	17.769	14.442	13.444	12.622
	η_o	0.2942	0.5026	0.6243	0.6738
	η_{th}	0.2603	0.4692	0.5659	0.5888
	η_p	1.1304	1.0716	1.1033	1.1443
	Thrust (N)	120430	79902	61681	40882
	CR	9.6109	15.599	25.403	31.699
	$\dot{m}_{air}$ (kg/s)	296.61	154.91	121.15	89.895

3. L_{comb} decreases slightly as M_0 increases (discussed more shortly). Therefore, this trend along with the trends mentioned in 1. result in an increase in nozzle size as M_0 increases.

4. The design variables θ_{nozz} and $\%_{cowl}$ are essentially at their maximum and minimum allowable values, respectively, for all flight Mach numbers. This is because the combination of these two variables, as mentioned, produces the largest thrust (refer to Figure 6-5).

5. Even though the overall efficiency η_o increases with increasing M_0, the thrust produced by the engine decreases significantly. This is mainly the direct result of the high mass flow rates at the low Mach numbers. Also, notice that there is an extreme jump in η_o from the optimal Mach 6 engine to the optimal Mach 8 engine. The low η_o at Mach 6 is believed to be a direct reflection of the fact that Mach 6 is sometimes considered the lower end of the scramjet operating range. Not shown in Table 6-6 is the fact that as the flight Mach number increases, the optimal scramjet engine operates at a higher combustor Mach number, pressure, and temperature. Since differential changes in these properties in the combustor are larger at higher combustor entrance conditions, a smaller combustor length is needed as M_0 increases in order to slow the flow down to its minimum allowable value (essentially Mach 1).

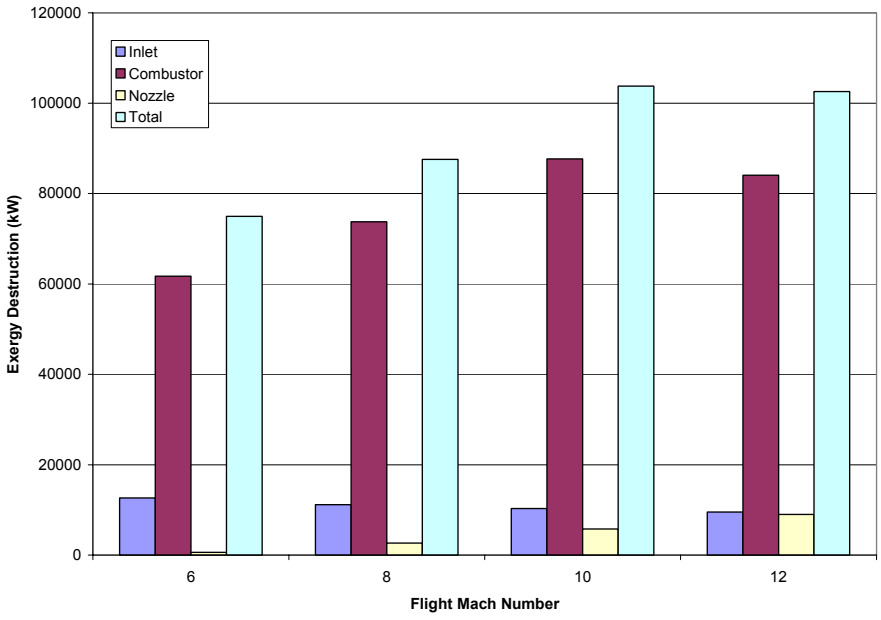

Figure 6-13. Rate of exergy destruction of the propulsion sub-system components for each of the optimal flight Mach number scramjet engines.

The exergy destroyed by each propulsion sub-system component for all four optimal scramjet engines is displayed in Figure 6-13. Figure 6-14 is a more detailed breakdown of Figure 6-13 where the exergy destroyed by each of the propulsion sub-system irreversible loss mechanisms is shown[69]. Figure 6-13 shows that the exergy destroyed by the inlet component decreases as the flight Mach number increases. This is what one would expect because the inlet decreases in size with increasing M_0. The nozzle component shows a trend opposite to that of the inlet, i.e. nozzle exergy destruction increases with flight Mach number. This is also as expected because not only does the nozzle increase in size as M_0 increases but the nozzle heat loss rate also increases. Finally, Figure 6-13 shows that, in general, the combustor and total exergy destruction both increase as M_0 increases up to Mach 10. However, this could just be a result of the assumptions made in this investigation. Even though combustor length decreases slightly as M_0 increases, the combustor exergy destruction should be expected to increase because of operating at a larger Mach number, pressure, and temperature (refer to Figures 6-9 and 6-10).

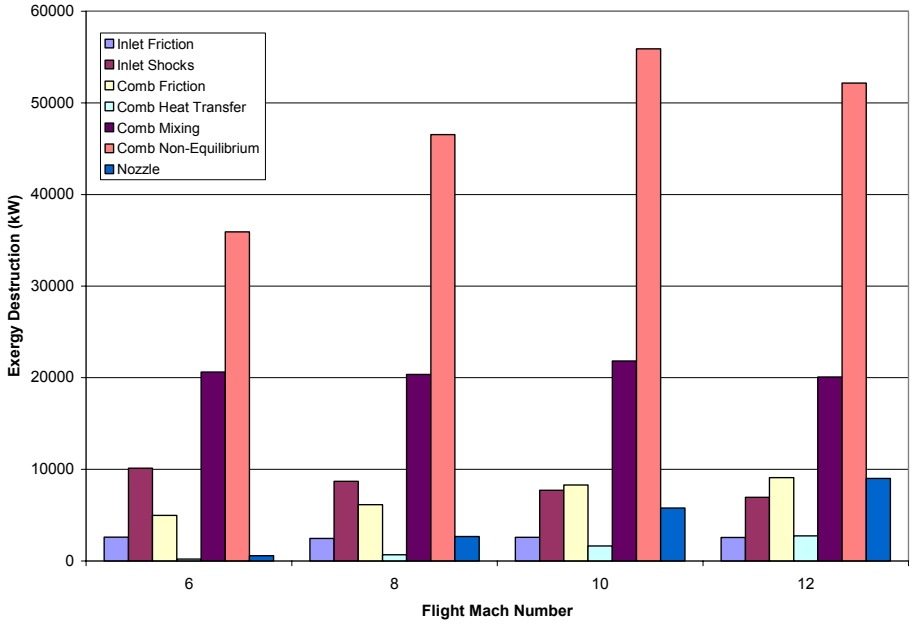

Figure 6-14. Exergy destruction due to individual loss mechanisms for each of the optimal flight Mach number scramjet engines.

[69] The nozzle losses are not, in this case, broken down into heat transfer and friction losses. Refer to Section 4.1.3 for an explanation of the nozzle irreversibility calculation.

A final propulsion sub-system study completed for this work (and the most recent study for this thesis work) was a comparison of the optimal scramjet engines determined from two different objective functions. One objective function utilized in this investigation is the overall efficiency given by Equation (6.5) which is maximized (or its inverse minimized). The second optimization problem is

$$\text{Minimize } f(\vec{x}) = \dot{E}x_{des} + \dot{E}x_{fuel_{loss}} \tag{6.7}$$

where the second term on the right hand side of Equation (6.7) is the lost rate of exergy in unburned fuel out the back of the vehicle (due to mixing losses). The purpose of the two optimizations is to determine which objective function produces an engine (propulsion sub-system) which consumes the least amount of fuel.

To make a justifiable comparison between these two objective functions, the engine was required to produce 70,000 N of thrust. Therefore, this analysis allowed for throttling of the equivalence ratio in order to provide the required thrust (explained in Section 4.2.5). Additionally, the analysis was conducted for a flight Mach number of $M_0 = 8$ and an angle-of-attack of $\alpha = 0^\circ$. A few optimization runs were made for both objective functions and the optimal solution was simply the solution with the lowest objective function value. Each optimization was run until it appeared to have converged[70] to a solution which typically took anywhere from 15,000-30,000 function evaluations. This resulted in computational times of approximately 10-15 hours on a 2.79 GHz Pentium 4 processor with 512 MB of RAM.

The results of this analysis are given in Table 6-7 where the design decision variables are shown along with the engine operating mass flow rate of fuel, the equivalence ratio, and the vehicle volume produced by this engine. For this thesis work, Equation (6.5) is referred to as a 1st Law based objective function and Equation (6.7) as a 1st/2nd Law based objective function[71]. Table 6-7 reveals that there are similarities between the design variables determined from the optimization of the 1st and 1st/2nd Law objective functions. In fact, these similarities result in two vehicles with almost identical volumes. Additionally, the two optimizations produced engines

[70] The optimizations were stopped if the objective function value did not change for a few thousand evaluations.
[71] In reference to the 1st and 2nd Laws of Thermodynamics.

that both operate at the same equivalence ratio and consume almost the same amount of fuel (about a 1.5% difference between the two).

Table 6-7. Energy and exergy based optimizations for a scramjet engine with fixed thrust.

Obj. Function	X_{fb}	X_{cowl}	X_{ramp1}	θ_{fb}	θ_{nozz}
1st Law	8.6114	13.652	2.9049	4.6026	17.066
1st/2nd Law	8.4019	13.895	3.1784	4.5669	17.549
	L_{comb}	$\%_{cowl}$	$\dot{m}_f$ (kg/s)	ϕ	$\forall_{veh}$ (m^2)
1st Law	1.1148	0.0016	2.6363	0.5	26.039
1st/2nd Law	1.1523	0.0113	2.6754	0.5	26.025

The results of this analysis show that exergy methods possess the ability to determine the optimal scramjet engine, i.e. the scramjet engine that consumes the least amount of fuel to produce a required thrust. This can be concluded because the 1st Law objective function directly minimizes $\dot{m}_f$ (the numerator is a fixed constraint in this analysis) and the 1st/2nd Law objective function produces effectively the same fuel flow rate. It is also reasonable to conclude that if the optimizer used work were coupled to an effective gradient-based search algorithm which could focus in more precisely on the "global" optimum given the results of the EA for both objective functions that the objective functions would produce fuel consumption rates ever closer to each other. This is because the maximum power (ideal power) the engine is capable of producing is equal to the sum of the thrust power, exergy destruction rate, and fuel exergy loss rate, i.e.

$$\dot{m}_f ex_f = P_{thrust} + \dot{E}x_{des} + \dot{E}x_{fuel_{loss}} \tag{6.8}$$

Since the thrust power is a fixed constraint, minimization of the exergy destruction rate and exergy loss rate ultimately minimizes the fuel flow rate required to produce the necessary thrust.

An advantage of using the exergy-based measure given by Equation (6.7) for this problem is that a detailed breakdown of all of the losses produced by each of the propulsion sub-system loss mechanisms (for example, see Figure 6-14) can be used to provide insight into where the largest improvements in engine performance can be realized. These improvements in engine performance (by reduction of certain losses) ultimately allow a smaller mass flow rate of fuel to

be consumed to produce a fixed thrust. The vehicle overall efficiency provides no such insights as to where improvements in the engine can be made to further reduce the amount of fuel being consumed to produce the fixed thrust.

6.4 Single Mission Segment Optimizations and Partial Mission Optimizations

Single mission segment (i.e. single Mach number) optimizations and a partial mission (consisting of three contiguous mission segments) optimization were performed for three different objective functions. These optimizations were performed utilizing the entire hypersonic vehicle model, i.e. propulsion sub-system and airframe sub-system. The single mission segment optimizations correspond to each of the three segments (i.e. legs) of the partial mission. The partial mission implemented for this thesis is given in Table 6-8. This partial mission was deemed sufficient for verifying the proper operation of all the models and to seek solutions to all three of the objectives[72].

Table 6-8 shows that single mission segment optimizations were conducted for Mach 8 and Mach 10 cruise and Mach 8-10 acceleration where the flight Mach number is taken to be $M_0 = 9$. Both cruise mission segments required that $T = D$ and the acceleration mission segment required a certain thrust determined from Equation (3.1). The hypersonic vehicle was required to have a fuel mass fraction of $\pi_f = 0.15$ for the single segment cruise optimizations and a fuel mass fraction of $\pi_f = 0.10$ for the single segment acceleration optimizations[73]. Additionally, the hypersonic vehicle operated at a design Mach number of $M_{design} = 9$ for all single segment optimizations.

The two objective functions initially used to optimize all three single mission segments were the vehicle overall efficiency and the total rate of exergy destruction, given by Equations (6.5) and (6.3), respectively. The vehicle overall efficiency was maximized and the total rate of exergy destruction was minimized for all optimizations. A third objective function implemented in these optimizations was that defined by Equation (6.7) (for reasons to be discussed shortly).

---

[72] As noted earlier a complete mission (see Figure 5-1) will be presented at the completion of the thesis work of K. M. Brewer anticipated for May 2005.

[73] These two fuel mass fractions are arbitrarily chosen for this analysis.

Table 6-8. Partial mission specifications.

Segment	Description
0	Mach 8 cruise for 1000 nm
1	Accelerate and climb from Mach 8 to Mach 10, $t \leq 90$ s
2	Mach 10 cruise for 1000 nm

Several runs[74] of the optimizer were performed for the each of the single segments using the two initial objective functions. Only two runs of the optimizer were performed for both the Mach 10 cruise segment and the Mach 8-10 acceleration segment using the objective function defined by Equation (6.7) (due to time constraints). Once again, the minimum (or maximum, depending on objective function) objective function value for each of the single segments was assumed to be the "global" optimum for comparison and analysis purposes.

All of the single segment optimizations were carried out on a 2.79 GHz Pentium 4 processor with 512 MB of RAM. It took anywhere from 50,000-800,000 function evaluations for the optimizer to find an initial feasible solution (i.e. a solution that does not violate any constraints), which in of itself many hours[75]. Once a feasible solution was found, the optimizations were carried out until the objective function did not change for at least 30,000 function evaluations[76]. A complete optimization of a single mission segment (one run of the optimizer) typically took a day and a half. Unlike that for the propulsion sub-system optimizations, each optimization run of a single segment did not produce relatively the same objective function value, especially for the optimization of η_o. It was concluded that the optimizer for some of these runs was more than likely getting stuck at a local optimum. As mentioned earlier, the coupling of a gradient-based method to the optimizer could alleviate this problem. However, it was also concluded with some confidence that the lowest optimum value of each objective function found for these single mission segment optimizations was either a "global" optimum or a very good local optimum.

The results of single segment optimizations for all three objective functions are shown in Tables 6-9 and 6-10. More specifically, Table 6-9 reveals the optimal values of the design

[74] Usually 3-5 runs depending on the precision of the objective function values.
[75] This problem was to be due to the fact that the optimizer generates random numbers to 16 significant digits.
[76] It is possible but not probable that many evaluations later the optimizer may find a better solution. However, numerous tests revealed no evidence of this. Additionally, excessive computational times would occur for many more function evaluations.

decision variables (i.e. optimal vehicle configurations) determined by each objective function and Table 6-10 displays values of calculated parameters such as exergy destruction rates, mass flow rates, wing planform areas, vehicle volumes, etc. (parameters of interest).

Table 6-9. Design variable values for single segment optimizations.

Mach #	Obj. Funct.	X_{fb}	X_{cowl}	X_{ramp1}	θ_{fb}	α	θ_{nozz}	L_{comb}	$\%_{cowl}$
8	η_0	8.5303	12.619	2.4418	2.5501	1.7227	17.512	0.8933	0.0207
	$\dot{E}x_{des}$	8.4284	14.313	3.1839	1.0000	0.9547	15.524	0.5000	0.0736
8-10	η_0	8.6716	13.616	3.2772	1.4914	1.2096	17.999	0.9451	0.0009
	$\dot{E}x_{des}$	8.4101	13.441	2.7657	1.0365	2.2349	17.335	0.5007	0.0860
	$\dot{E}x_{des} + \dot{E}x_{fuel_{loss}}$	8.5617	12.603	2.6580	1.0000	1.1521	12.8238	0.8802	0.2432
10	η_0	8.4094	11.969	2.4620	1.7887	1.2450	15.842	0.7017	0.0136
	$\dot{E}x_{des}$	8.5113	14.267	3.0703	1.2493	0.9818	16.057	0.5003	0.2272
	$\dot{E}x_{des} + \dot{E}x_{fuel_{loss}}$	8.4127	13.265	3.2994	1.0577	1.7537	15.537	0.7775	0.2019

Table 6-9 shows that all optimizations resulted in vehicles in which the forebody length is relatively close to its minimum allowable value of $X_{fb} = 8.4$. In addition, the cowl position always fell within 50-60% of the total vehicle body length. Optimal vehicle configurations tend to have relatively small forebody deflection angles and angles-of-attack and rather large expansion angles (in most cases). One significant finding in these optimizations and shown in Table 6-9 is that minimization of the total rate of exergy destruction (Equation (6.3)) always resulted in a vehicle with a combustor length essentially at its minimum allowable value of $L_{comb} = 0.5$. This obviously occurred because the combustor component exergy destruction rates dominate the exergy destruction rates of the other components and because the shortest combustor ultimately destroys the lease amount of exergy (this topic is revisited shortly since it points to a deficiency in Equation (6.3) as the objective function). Another interesting result of the optimizations shown in Table 6-9 is that optimal hypersonic vehicle configurations at these

flight Mach numbers have rather short combustors in terms of percent vehicle length (usually less than 5% of L_{veh})[77].

To obtain a better picture of the differences in the vehicle configurations predicted by each of the objective functions, side portraits of the vehicle at each Mach number and for each objective function are provided in Appendix B. For all the figures, the optimal vehicle determined by the objective function η_0 is plotted in blue. For Figures B-1, B-2, and B-4, the optimal vehicle determined by the objective function $\dot{E}x_{des}$ is plotted in red. The optimal vehicle determined by the objective function $\dot{E}x_{des} + \dot{E}x_{fuel_{loss}}$ is plotted in red in Figures B-3 and B-5. It can be seen from Figures B-1 and B-4 that the objective functions η_0 and $\dot{E}x_{des}$ produce much different Mach 8 and Mach 10 cruise vehicles. The cruise vehicles determined from the optimization of $\dot{E}x_{des}$ tend to be much more slender and have larger inlets and smaller nozzles. The accelerator vehicle configurations are very similar for these two objective functions. Figure B-5 shows that minimization of $\dot{E}x_{des} + \dot{E}x_{fuel_{loss}}$ results in a more slender vehicle as well when compared to the vehicle predicted by maximization of η_0. In addition, the accelerator vehicles determined from η_0 and $\dot{E}x_{des} + \dot{E}x_{fuel_{loss}}$ are fairly different (unlike the case between η_0 and $\dot{E}x_{des}$).

In the end, the optimal hypersonic vehicle configurations determined from minimization of exergy destruction rates (Equation (6.3))or exergy destruction and exergy fuel loss rates (Equation (6.7)) are smaller, more slender vehicles than optimal vehicles predicted by maximization of the vehicle overall efficiency (Equation (6.5)). In addition, the center of gravity of all the vehicles is more or less in the same location. These two statements are verified in the figures in Appendix B and in Table 6-10.

Table 6-10 shows that short combustor lengths predicted by the exergy destruction objective function resulted in a vehicle that consumes a considerable amount of more fuel for all three single segments (this trend was also verified to occur for the partial mission). This was due to the fact that the shorter combustors did not produce any significant combustion; and, therefore, to produce appreciable thrust, the engine had to operate at higher equivalence ratios

[77] This was true for all other optimization runs as well.

(even though the vehicles were smaller and more slender and less thrust was needed to balance the drag or obtain the required thrust). Again, all of this points to a deficiency in Equation (6.3) as the objective function.

Table 6-10. Calculated optimal parameter values for single mission segment optimizations.

Mach #		8		8-10			10		
Obj. Funct.		η_0	$\dot{E}x_{des}$	η_0	$\dot{E}x_{des}$	$\dot{E}x_{des} + \dot{E}x_{fuel_{loss}}$	η_0	$\dot{E}x_{des}$	$\dot{E}x_{des} + \dot{E}x_{fuel_{loss}}$
$\dot{m}_{air}$ **(kg/s)**		121.82	119.56	105.20	95.084	92.460	84.700	96.134	84.944
$\dot{m}_f$ **(kg/s)**		0.6438	0.7021	1.8533	2.6801	1.6288	0.6963	0.9032	0.6983
ϕ		0.18	0.2	0.6	0.96	0.6	0.28	0.32	0.28
S_{wing} **(m²)**		5.4834	0.0507	0.5028	0.0002	0.5025	9.2679	0.0097	0.0082
ω **(°)**		3.8000	4.8500	4.8800	4.7300	2.9100	4.8800	5.8200	4.8300
Exergy Destruction (kW)	**Inlet**	9544.9	8377.1	9597.0	6380.7	9590.0	9337.6	6712.7	7909.4
	Comb.	29467	16853	60714	23235	54782	32670	20575	32521
	Nozzle	2251.5	1001.3	3912.4	2001.3	3939.7	5069.3	1838.9	3918.8
	Aero*	9635.1	8320.1	9568.2	9587.1	9450.0	10652	9801.06	10094
	Nrg*	563.02	552.61	0	0	0	277.33	314.77	278.1
	Total	51461	35104	83792	41203	75737	58007	39242	54722
$\forall_{veh}$ **(m²)**		26.171	18.750	23.966	22.856	18.351	24.052	19.735	21.081
x_{cg} **(m)**		13.640	13.634	13.742	13.974	13.269	13.690	13.648	13.633
y_{cg} **(m)**		-0.0112	-0.2744	-0.0764	0.0645	-0.1537	0.1235	-0.2668	-0.0607
η_o		0.4732	0.2015	0.5794	0.3780	0.5073	0.4422	0.1810	0.2886
$\dot{E}x_{fuel_{loss}}$		1515.8	23974	26951	213238	24891	2098.2	39064	2812.2
Thrust (N)		15212	7061.5	47493	44812	36549	12217	6487.6	7997.2

***** Nrg refers to the the rate of exergy destruction resulting from the energy exchange with the inlet component flow. Aero refers to the airframe sub-system.

A breakdown of the exergy destruction rates of each component or sub-system (along with that due to energy exchange) is given in Table 6-10. The table reveals that, in comparison with the η_0 objective function, the objective function $\dot{E}x_{des}$ did produce vehicles with smaller

components/sub-system exergy destruction rates. In fact, the total exergy destruction rates were approximately 32% less for the optimal $\dot{E}x_{des}$ cruise vehicles and almost 50% less for the optimal $\dot{E}x_{des}$ accelerator (compared to the optimal η_0 vehicles). For the optimal η_0 cruise vehicles, however, the fuel exergy loss rates were only about 5% of the optimal $\dot{E}x_{des}$ vehicles and for the optimal η_0 accelerator, the fuel exergy loss rates were approximately 13% of the optimal $\dot{E}x_{des}$ vehicle.

A comparison of the results of the η_0 and $\dot{E}x_{des}$ optimizations provides much insight with the conclusion that minimization of the exergy destruction rate is simply insufficient in determining a hypersonic vehicle configuration that consumes the least amount of fuel to produce the thrust for a given mission. It was recognized that not only is minimization of the exergy destruction rate desirable, but so is minimization of the fuel exergy loss rate in unburned fuel and, therefore, must be included in the objective function.

Table 6-10 reveals that minimization of $\dot{E}x_{des} + \dot{E}x_{fuel_{loss}}$ resulted in a Mach 10 cruise vehicle that consumes essentially the same amount of fuel as the optimal η_0 Mach 10 cruise vehicle. The sum of the exergy destruction and exergy loss for the optimal $\dot{E}x_{des} + \dot{E}x_{fuel_{loss}}$ vehicle is only about 4% less than that for the optimal η_0 vehicle. Further investigation of Table 6-10 reveals that the optimal η_0 vehicle produces substantially more thrust power (at Mach 10, $u_0 = 3023.2\ m/s$) than the optimal $\dot{E}x_{des} + \dot{E}x_{fuel_{loss}}$ vehicle. The previous two statements along with Equation (6.8) point to the fact that the optimal η_0 vehicle should actually consume more fuel than the optimal $\dot{E}x_{des} + \dot{E}x_{fuel_{loss}}$ vehicle. The fuel mass flow rates predicted by Equation (6.8) and using the values from Table 6-10 are $\eta_0 \Rightarrow \dot{m}_f = 0.7410\ kg/s$ and $\dot{E}x_{des} + \dot{E}x_{fuel_{loss}} \Rightarrow \dot{m}_f = 0.6143\ kg/s$. These flow rates[78] compared to those for $\dot{m}_f$ in Table 6-10 show that the fuel mass flow rate determined by the hypersonic vehicle model does not always correspond exactly to that required in Equation (6.8). It is understood that these discrepancies are probably due to a number of things such as assumptions made in component

[78] The tabulated mass flow rates are the mass flow rates required to produce the thrust power and overcome the rates of exergy destruction and fuel exergy loss listed in Table 6-10, i.e. these mass flow rates are more representative of the truth.

models, vehicle throttling methods, inexact prediction of the irreversibilities, etc. However, these discrepancies do not undermine the comparison of these two optimal vehicles and, if anything, substantiate the fact the optimal $\dot{E}x_{des} + \dot{E}x_{fuel_{loss}}$ vehicle consumes less fuel at Mach 10 cruise.

A comparison is also made in Table 6-10 between the optimal accelerator vehicles determined from the vehicle overall efficiency and the exergy destruction and exergy fuel loss objective functions. Table 6-10 shows that the optimal $\dot{E}x_{des} + \dot{E}x_{fuel_{loss}}$ accelerator has lower exergy destruction rates and fuel exergy loss rates as well as smaller thrust power production. Consequently, this vehicle consumes an appreciable less amount of fuel (about 12% less) than the optimal overall efficiency vehicle. For the accelerator vehicle, the sum of the exergy destruction and fuel exergy loss for the optimal $\dot{E}x_{des} + \dot{E}x_{fuel_{loss}}$ vehicle is approximately 10% less than that for the optimal η_0 vehicle. Once again using Table 6-10 along with Equation (6.8) (at Mach 9, $u_0 = 2712.1\, m/s$), the mass flow rates for the two objective functions are $\eta_0 \Rightarrow \dot{m}_f = 1.9728\, kg/s$ (6.5% larger than in the Table 6-10) and $\dot{E}x_{des} + \dot{E}x_{fuel_{loss}} \Rightarrow \dot{m}_f = 1.6324\, kg/s$ (0.2% larger than in the Table 6-10). This again further emphasizes the fact that the optimal $\dot{E}x_{des} + \dot{E}x_{fuel_{loss}}$ accelerator consumes less fuel than the optimal η_0 vehicle .

A few other interesting results can be seen in Table 6-10. For example, the table shows that using either of the exergy objective functions results in a vehicle requiring almost no additional planform area to provide the necessary vehicle lift whereas the vehicle overall efficiency objective function sometimes results in a vehicle with considerable planform areas. It also appears that for all the optimal vehicles, the elevon deflection angle is rather minimal and the center of gravity of the vehicles tend to be along the vehicle reference axis at a location almost always near 57% of L_{veh}. Finally, it is shown that cruise vehicles operate at rather low equivalence ratios.

After analyzing the results of the single segment optimizations it can be concluded that minimization of the exergy destruction and fuel exergy loss rates minimizes the amount of fuel consumed by a hypersonic vehicle for a given mission beyond that which maximization of the

vehicle overall efficiency achieves. It can further be concluded from these analyses that the acceleration segment of the partial mission will most likely dictate the vehicle design because this is where the largest rates of exergy destruction and fuel exergy loss occur.

Lastly, a three-dimensional solid model for a typical Mach 10 hypersonic cruise vehicle is given in Figure 6-15 to provide a clearer image of the hypersonic vehicle configurations implemented in this thesis work.

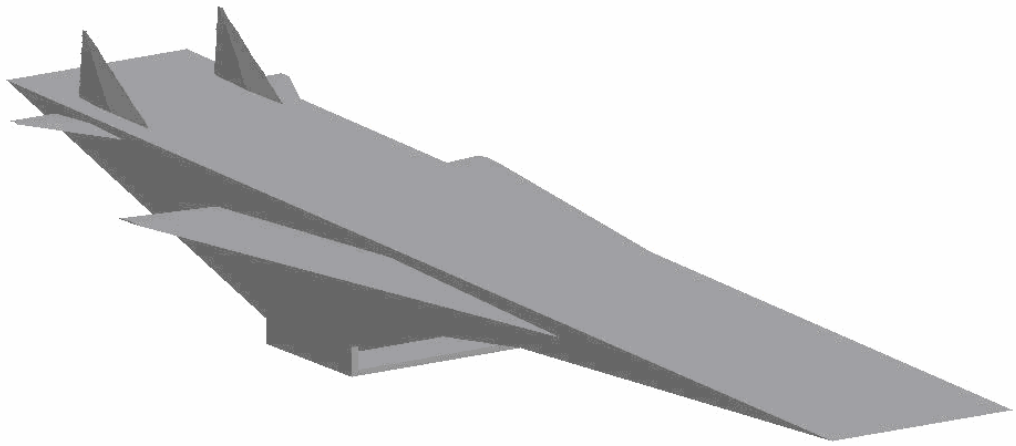

Figure 6-15. 3D CAD representation of a typical Mach 10 hypersonic cruise vehicle.

With the partial mission defined in Table 6-8, an estimation was made of the initial total mass (empty mass + fuel mass) of the hypersonic vehicle using Equations (4.86)-(4.89). In determining the fuel mass fractions for each mission segment, the initial and final velocity and elevation were determined from knowledge of the constant dynamic pressure trajectory. Also, prediction of the estimated fuel mass fractions required estimation of the vehicle overall efficiency and lift-to-drag ratio of the vehicle. For this analysis, the vehicle average overall efficiency and lift-to-drag ratio were estimated to be $\eta_0 = 0.35$ and $L/D = 4.0$ over the whole mission. Based on these values, the fuel mass fractions for each of the mission segments are given in Table 6-11. In addition to these fuel mass fractions, a fuel mass fraction of $\pi_f = 0.06$ was added to the vehicle to represent some amount of fuel that is required to return the vehicle to its origin (or destination). Therefore, it is evident that for this partial mission analysis, the

hypersonic vehicle requires an estimated 30.69% of its initial mass to be fuel. Once a vehicle volume is determined, the estimated initial mass of the vehicle can be calculated[79].

Table 6-11. Mission segment fuel mass fractions.

Segment	Fuel Mass Fraction, π_f
0	0.1025
1	0.0419
2	0.1025
$\sum_{0}^{2} \pi_f$	0.2469

At the end of each mission segment, the mass flow rate of fuel required for that segment is known. Therefore, with knowledge of both the mission segment time and fuel flow rate, the mass of the vehicle at the end of each mission segment can be determined. This updated vehicle mass becomes the mass for the next mission segment. At the end of the mission, the amount of fuel needed to complete the mission is known and can be compared to the initial prediction. Realistically, if there is an appreciable percent difference between the initial prediction and the calculated value, the mission would be re-run with the same vehicle but now using the calculated total fuel mass fraction. This iterative process would be repeated until convergence. However, to reduce the computational burden, this method was not incorporated for this thesis work. The consequences of doing so are discussed following Table 6-15 below where a comparison of the initial total fuel mass fraction and the calculated total fuel mass fraction will be given in the mission results.

All of the partial mission optimizations were carried out on a single AMD Athlon 2.08 GHz processor with 992 MB of RAM. It took anywhere from 200,000 function evaluations to sometimes over 1 million function evaluations to find an initial feasible solution. Once an initial feasible solution was found, the optimizations were carried out until the objective function value did not change for several thousand evaluations. However, the optimizations were only discontinued at this point if the objective function had already progressed through a series of minimizations. Usually less than 20,000 function evaluations were conducted once an initial

[79] Note that the empty mass of the vehicle is scaled based upon the vehicle volume. See Section 4.2.4.

feasible solution was found[80]. This was because computational times became quite excessive. The first few thousand evaluations, once an initial solution was found, proceeded relatively quickly. However, as more and more feasible solutions were discovered, the computational times became much larger. Typically, after 8,000 function evaluations past the initial feasible solution, computational times became around 9-12 hours per 1,000 evaluations. For this reason, the optimizations were ended if the objective function value did not change for several thousand evaluations.

Optimizations were once again conducted using the same three objective functions as in the single segment optimizations. The results of the mission optimizations are given in Tables 6-12, 6-13, and 6-14. Table 6-12 presents the optimal design decision variables, Table 6-13 the operational decision variable values in each of the mission segments, and Table 6-14 displays other optimal parameter values which were deemed pertinent to the following discussion. Results are presented for the $\dot{E}x_{des}$ objective function in all three tables to further emphasize its inability to provide more desirable configurations, i.e. it predicts instead shorter combustor lengths and larger fuel consumption rates. Consequently, further comparisons with the other two objective functions are not included in the remaining discussion.

It can be seen that, as with the optimal single mission segment vehicles, the optimal mission vehicles have forebody lengths that are relatively close to the minimum value and the cowl position falls within the same range described earlier. The optimal mission vehicles also have small forebody angles and seem to require, in general, small nozzle expansion angles when optimized for a mission. Table 6-12 shows that the optimal $\dot{E}x_{des} + \dot{E}x_{fuel_{loss}}$ vehicle has a substantially larger combustor length and nozzle cowl extension than the optimal η_0 vehicle. Some of these traits can be seen in Appendix C where the optimal η_0 vehicle is plotted in blue and the optimal $\dot{E}x_{des} + \dot{E}x_{fuel_{loss}}$ vehicle is plotted in red. It is shown that the optimal $\dot{E}x_{des} + \dot{E}x_{fuel_{loss}}$ vehicle is more slender and has a slightly larger inlet and a smaller nozzle. Since the vehicle is more slender, the vehicle volume is less (length the same), and it consequently has a smaller empty mass as shown in Table 6-14.

[80] The optimizations progressed much more rapidly for the mission than for the single segment.

Table 6-12. Optimal design decision variable values for the partial mission.

Objective Function	X_{fb}	X_{cowl}	X_{ramp1}	θ_{fb}	θ_{nozz}	L_{comb}	$\%_{cowl}$
η_0	8.4371	13.186	3.2913	1.2179	15.835	0.6385	0.0010
$\dot{E}x_{des}$	8.5021	13.667	2.7605	1.0017	15.889	0.5067	0.0115
$\dot{E}x_{des} + \dot{E}x_{fuel_{loss}}$	8.8604	13.959	3.2978	1.0176	14.106	0.8240	0.1610

Table 6-13 shows that the optimal η_0 vehicle fly's at larger angles-of-attack throughout the mission. It also shows that the optimal η_0 vehicle requires much larger planform areas to provide the necessary lift at each mission segment. It is concluded from these results and the results of the single mission segment optimizations that the optimal vehicles have small angles-of-attack because of their influence on the performance of the inlet component.

Table 6-13. Optimal operational decision variable values for the partial mission.

Objective Function	α			S_{wing}		
	0	1	2	0	1	2
η_0	1.7724	1.2	0.9	7.2033	5.7615	9.3670
$\dot{E}x_{des}$	1.4453	0.8	0.8	7.6983	9.2350	0.4869
$\dot{E}x_{des} + \dot{E}x_{fuel_{loss}}$	1.1933	0.4	0.3	0.7908	3.2372	0.5065

Table 6-14 reveals that the optimal $\dot{E}x_{des} + \dot{E}x_{fuel_{loss}}$ vehicle consumes less fuel at each of the mission segments in comparison to the optimal η_0 vehicle. It consumes approximately 6%, 17%, and 2% less for mission segments 0, 1, and 2, respectively, and for the entire mission it consumes about 6.5% less (70 kg). Table 6-14 also shows that both optimal vehicles require a larger mass flow rate of fuel than that which is being injected into the combustor to cool the combustor and nozzle surfaces (a result of larger heat loads at higher Mach numbers) for the Mach 10 cruise segment. The additional 6% of initial vehicle weight carried during the mission provides enough extra fuel to allow the necessary cooling for both vehicles. It is apparent that vehicle cooling requirements are a serious hypersonic vehicle synthesis/design consideration.

Table 6-14. Calculated optimal parameter values at each segment of the partial mission.

Obj. Funct.	η_o			$\dot{E}x_{des} + \dot{E}x_{fuel_{loss}}$			$\dot{E}x_{des}$		
Segment	0	1	2	0	1	2	0	1	2
$\dot{m}_{air}$ (kg/s)	109.35	96.875	86.004	115.67	102.47	90.961	111.91	99.138	88.005
$\dot{m}_f$ (kg/s)	0.5779	2.3892	0.7070	0.5434	1.9856	0.6944	0.7228	2.7943	0.8269
$\dot{m}_{f_{need}}$ (kg/s)	0.5012	0.7416	0.9995	0.4996	0.7473	0.9997	0.1998	0.2942	0.3917
m_{empty} (kg)	4374.4			3568.6			4093.5		
m_{fuel} (kg)	445.50	215.03	433.1	418.91	178.70	425.39	556.21	251.49	506.56
ϕ	0.18	0.84	0.28	0.16	0.66	0.26	0.22	0.96	0.32
Exergy Destruction (kW) — Inlet	10372	9251.9	8267.1	10411	9286.2	8296.9	7950.2	7091.6	6336.2
Exergy Destruction (kW) — Comb	24540	48843	30544	25121	52162	31638	17306	22535	19833
Exergy Destruction (kW) — Nozzle	2403.5	4215.1	4161.2	1836.2	3255.9	3229.5	1098.8	1821.0	1947.5
Exergy Destruction (kW) — Aero*	8669.9	9420.1	10171	8504.7	9302.4	9874.7	8534.7	9343.4	9915.9
Exergy Destruction (kW) — Nrg* Nose	505.42	15.282	128.28	534.64	44.161	111.66	517.25	24.824	157.92
Exergy Destruction (kW) — Nrg* Ramp	0	50.931	97.277	0	120.61	132.51	0	71.299	63.704
Exergy Destruction (kW) — Total	46492	71794	53368	46409	74173	53284	35407	40889	38254
$\dot{E}x_{fuel_{loss}}$ (kW)	2018.4	97165	4697.6	1515	53687	3922.4	23935	228780	33461
Thrust (N)	12748	50511	10521	7845.2	39996	5666.0	9174.4	46302	7520.9
η_o	0.4418	0.4779	0.3750	0.2892	0.4554	0.2056	0.2545	0.3747	0.2295
$\forall_{veh}$ (m^2)	21.872			17.843			20.467		
$\pi_{f_{calc}}$	0.0815	0.0393	0.0792	0.0912	0.0389	0.0926	0.1029	0.0465	0.0937

* Nrg refers to the rate of exergy destruction resulting from the energy exchange with the inlet component flow. Aero refers to the airframe sub-system.

The values of the thrust power (at Mach 8, $u_0 = 2402.5\, m/s$) and rates of exergy destruction and fuel exergy loss given in Table 6-14 were once again used in conjunction with Equation (6.8) to calculate the mass flow rate of fuel required to supply the thrust power and overcome exergy destruction rates and fuel exergy loss. These calculated mass flow rates are compared to the model mass flow rates for both optimal vehicles in Table 6-15. It is apparent that once again there are some discrepancies in these values but, if anything, only substantiate the conclusions already drawn.

Table 6-15. Vehicle optimal fuel mass flow rate comparison.

Segment	$\dot{E}x_{des} + \dot{E}x_{fuel_{loss}}$		η_0	
	Calculated $\dot{m}_f$	Model $\dot{m}_f$	Calculated $\dot{m}_f$	Model $\dot{m}_f$
0	0.4998	0.5434	0.6045	0.5779
1	1.9475	1.9856	2.5437	2.3892
2	0.5529	0.6944	0.6836	0.7070

Table 6-14 also shows that the optimal $\dot{E}x_{des} + \dot{E}x_{fuel_{loss}}$ vehicle has less rates of exergy destruction in only the nozzle component and the airframe sub-system only in comparison with the optimal η_0 vehicle. In fact, the optimal $\dot{E}x_{des} + \dot{E}x_{fuel_{loss}}$ vehicle has a larger rate of exergy destruction during the acceleration segment and only slightly lower rates of exergy destruction during both cruise segments. However, the rates of fuel exergy loss for the optimal $\dot{E}x_{des} + \dot{E}x_{fuel_{loss}}$ vehicle are approximately 25%, 45%, and 17% less for segments 0, 1, and 2, respectively. It is worth noting that even though the sum of the exergy destruction and fuel exergy loss rates are smaller for the optimal $\dot{E}x_{des} + \dot{E}x_{fuel_{loss}}$ vehicle, it still is less efficient transforming energy in the fuel tank to useful propulsive work.

For the partial mission analysis, minimizing the rates of exergy destruction and fuel exergy loss produce a more optimal vehicle in terms of fuel consumption than maximizing the vehicle overall efficiency. This is because the vehicle overall efficiency is only concerned with production of vehicle thrust and does not account for the additional degrees of freedom of the airframe sub-system (see [70]). The exergy-based measure does account for the degrees of freedom of the airframe by calculating the rates of exergy destruction produced by external aerodynamic surface shear forces. Since all the vehicle losses are determined in terms of a common metric (i.e. exergy destruction rates), the losses occurring in the vehicle sub-systems and components can be compared to identify the location of where the largest improvements in vehicle performance can be made.

Tables 6-16 and 6-17 show the effectiveness of the optimizations performed using the η_0 and $\dot{E}x_{des} + \dot{E}x_{fuel_{loss}}$ for the partial mission. More specifically, these tables show a comparison of the initial solution found by the optimizer and the final optimal solution for both objective

functions (as given in Table 6-14). Table 6-16 reveals that the for $\dot{E}x_{des} + \dot{E}x_{fuel_{loss}}$ objective function significant decreases in the fuel consumption rates and fuel exergy loss rates have been accomplished through optimization and appreciable decreases in exergy destruction rates have occurred as well. Table 6-17 shows that for the η_0 objective function fuel mass flow rates decreased substantially and the vehicle overall efficiency increased significantly at each mission segment.

Table 6-16. Comparison of initial feasible vehicle and final optimal vehicle using the exergy objective function.

Objective Function		$\dot{E}x_{des} + \dot{E}x_{fuel_{loss}}$	
		Initial Value	**Final Value**
Obj. Funct. Value		368764	232990
$\dot{m}_f$ **(kg/s)**	0	0.8184	0.5434
	1	3.0613	1.9856
	2	1.0012	0.7473
$\dot{E}x_{fuel_{loss}}$ **(kW)**	0	9108.3	1515
	1	152900	53687
	2	16439	3922.4
$\dot{E}x_{des_{total}}$ **(kW)**	0	53691	46492
	1	76533	74173
	2	60089	53284

Table 6-17. Comparison of initial feasible vehicle and final optimal vehicle using the overall efficiency objective function.

Objective Function		η_o	
		Initial Value	**Final Value**
Obj. Funct. Value		3.5720	2.317
$\dot{m}_f$ **(kg/s)**	0	0.7156	0.5779
	1	2.7241	2.3892
	2	0.8898	0.7070
η_o	0	0.2608	0.4418
	1	0.3771	0.4779
	2	0.2020	0.3750

It can be seen it Table 6-14 that the actual total fuel mass fraction (sum of segments 0, 1, and 2) is less than that predicted in Table 6-11 for both vehicles (10% less for the optimal $\dot{E}x_{des} + \dot{E}x_{fuel_{loss}}$ vehicle and 20% less for the optimal η_0 vehicle). Therefore, the iterative process described earlier would be beneficial for obtaining more exact values in Table 6-14. This iterative process could have some impacts on the final results shown in Table 6-14

depending on the magnitude of the difference between the actual fuel mass fraction and the estimated fuel mass fraction. Impacts such as larger/smaller planform areas could conceivably require larger/smaller thrust requirements which ultimately influence fuel consumption rates. However, even a 10% error (or possibly more) like that encountered in this thesis work may only slightly influence the planform size and, consequently, may produce no change in the fuel consumption rates (due to the throttling process used in this thesis work). Nonetheless, the iterative process is worth considering for future mission optimizations.

Finally, a number of simplifications were made to the sub-system and component models to achieve the desired objectives within the context of one-dimensional analysis and as a result of computational restrictions. This thesis work strived towards the development and presentation of theory (i.e. demonstration of methodology) and not the prediction of 'exact' vehicle operating conditions, parameter values, etc. Therefore, the reader should take caution when considering the conclusions and some of the parameter values presented in the tables with respect to real hypersonic vehicles.

Chapter 7

Conclusions

A number of conclusions can be drawn from the various parametric studies and optimizations performed as well as from the work that led up to the production of the results in Chapter 6. The main conclusions derived from the results of this research are summarized as follow:

1. Hypersonic aircraft systems are highly dynamic, integrated vehicles which are subjected to a wide array of flight conditions. Sufficiently accurate physical, thermodynamic, and aerodynamic models are required to predict the performance of these systems over the flight spectrum with any confidence. Sufficiently accurate models were developed for this thesis work which permitted good predictions of performance as well as of irreversibilities due to the various hypersonic vehicle system loss mechanisms.

2. The evolutionary algorithm (EA) optimization software utilized in this thesis work had a number of benefits and drawbacks. The EA required no initial guess of the design decision variables and possessed the ability to optimize the large-scale hypersonic vehicle mission problem. However, long computational times, which, of course, are the nature of the EA optimization approach, occurred for both single mission segment and partial mission optimizations, suggesting that more computational power may be needed in the future. Furthermore, re-optimizing only sometimes repeated the previous solution sufficiently well to validate it as the best to be found. As previously mentioned, this particular problem can be alleviated to a large extent through the coupling of a gradient-based method with the evolutionary algorithm, i.e. by feeding the final solution of the EA to the gradient-based method so that it can use this solution as its initial point and zoom in on what is thought to be the "global" solution.

3. Scramjet engine investigations show that as expected the combustor component is the one with the largest rates of exergy destruction. Consequently, the design of the combustor component requires a great deal of attention, especially focusing on providing efficient mixing and burning at high flow velocities. It was shown that the combustor irreversible loss mechanisms are largely affected by combustor entrance properties and, therefore, an inlet must provide desirable conditions to the combustor over a large range of flight conditions.

4. Optimizations on a fixed-geometry scramjet engine only were conducted over a range of Mach numbers in order to determine the effects of maintaining the shock-on-lip condition at design and off-design through energy exchange with the free stream at two-points prior to the entrance of the engine inlet. These results were then compared with the performance of the same engine without energy exchange. The results seem to indicate that even with a device which provides or extracts energy from the free stream at an efficiency of only 50%, that the benefits in terms of thrust gain are quite substantial over those for an engine without such a device.

5. Optimizations were performed for the propulsion sub-system only at a number of flight Mach numbers using the overall vehicle efficiency as the objective function. These optimizations revealed a number of trends, most notably, a decrease in the inlet component size as the flight Mach number increased and a rather large increase in the overall vehicle efficiency as the flight Mach number increased. Another result of these optimizations was an appreciable increase in the rate of exergy destruction as the flight Mach number increased from Mach 6 to Mach 12.

6. An exergy-based method (i.e. the thermodynamic effectiveness) was shown to be able to predict essentially the same optimal combustor length as a thrust-based measure (i.e. the engine effectiveness) in terms of thrust production. The application of this exergy-based method to the design optimization of a hypersonic propulsion sub-system *only* resulted in a scramjet engine configuration that consumed the least amount of fuel to maintain a *given thrust*. Thus, minimization of the rate of exergy destruction due to the irreversible loss mechanisms present in the engine and the rate of fuel exergy loss due to incomplete mixing gave a scramjet configuration that effectively consumed the same amount of fuel

as a scramjet that was optimized for minimum fuel usage. The use of a gradient-based method coupled to the EA would have only further confirmed this result by producing identical fuel consumption rates for the two optimal engines.

7. Single mission segments and a partial, three-segment mission were optimized for three different objective functions; namely, the overall vehicle efficiency, η_0, the rate of exergy destruction $\dot{E}x_{des}$, and the rate of exergy destruction plus fuel exergy loss $\dot{E}x_{des} + \dot{E}x_{fuel_{loss}}$. It was shown for both single mission segment optimizations and the partial mission optimization that $\dot{E}x_{des}$ produced undesirable optimal configurations because of its tendency to arrive at a vehicle configuration with the smallest allowable combustor length. However, adding the rate of fuel exergy loss to the rate of exergy destruction, i.e. $\dot{E}x_{des} + \dot{E}x_{fuel_{loss}}$, resulted in an optimal vehicle for the partial mission that consumed less fuel than the optimal partial mission vehicle determined from the η_0 optimization. In fact, a 6.5% smaller amount of fuel was consumed by the optimal $\dot{E}x_{des} + \dot{E}x_{fuel_{loss}}$ vehicle in comparison with the optimal η_0 vehicle. It was further concluded that a larger savings in fuel consumption more than likely will be realized when these two objective functions are evaluated for a more complete mission (e.g., the one given in Figure 5.1).

8. This thesis work presented one of the *first* known totally integrated hypersonic vehicle concept optimizations throughout a hypersonic mission. An exergy-based measure produced a more optimal vehicle in terms of fuel consumption than a standard hypersonic vehicle performance measure (the vehicle overall efficiency). This is because the overall efficiency is only concerned with thrust production and does not consider the additional degrees of freedom of the airframe sub-system. The exergy-based measure does account for the airframe sub-system degrees of freedom through calculation of surface shear force exergy destruction rates. Additionally, quantifying all the vehicle losses in terms of rate of exergy destruction provides a common metric for the vehicle designer to identify where the largest improvements in vehicle performance can be made which ultimately result in a lower amount of fuel consumption.

Appendix A

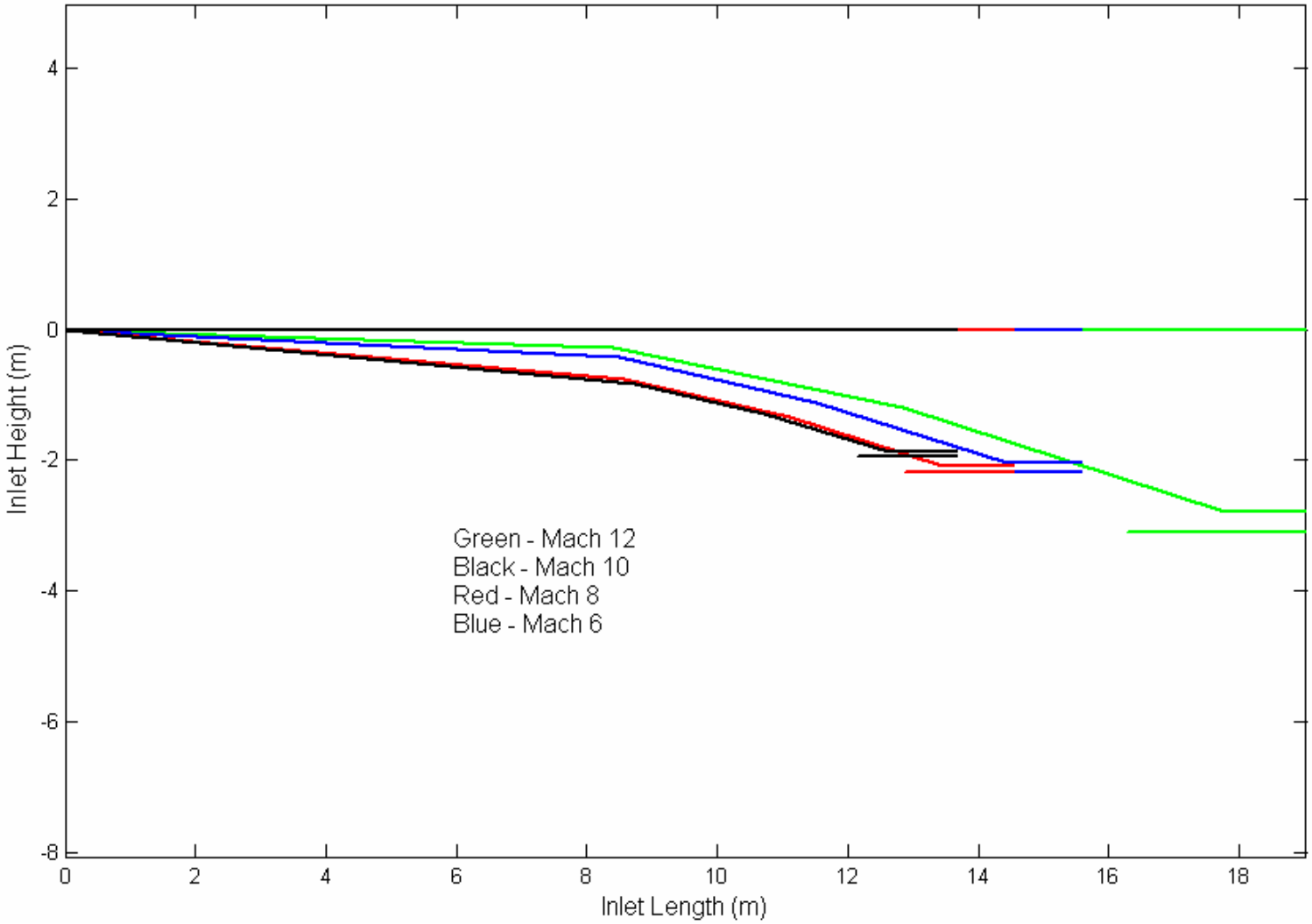

Figure A-1. Optimal inlet component configurations for the scramjet engine (propulsion sub-system) only optimizations.

Appendix B

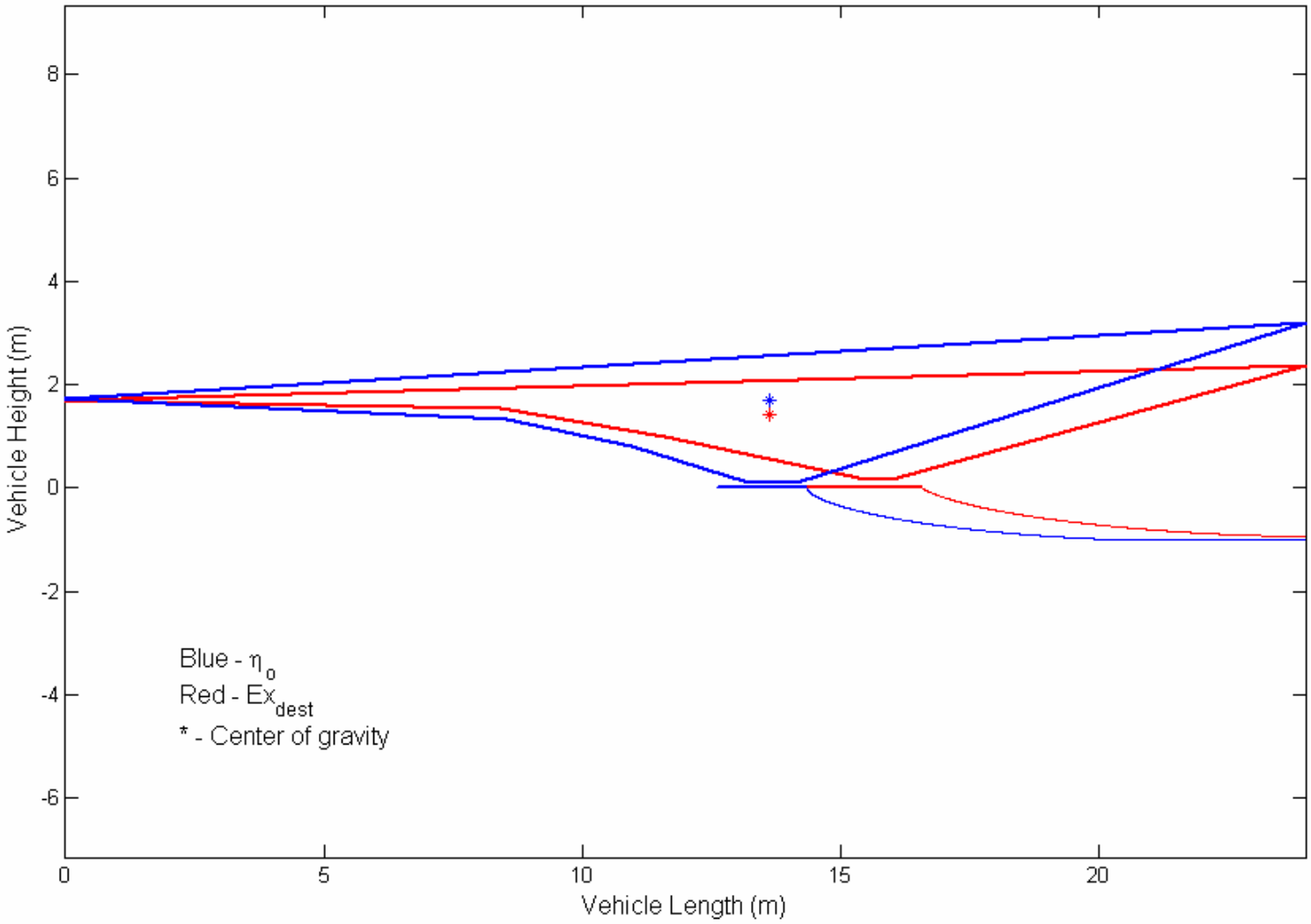

Figure B-1. Optimal Mach 8 cruise vehicles for the single segment optimizations using the objective functions η_o and Ex_{dest}. Both the vehicle plumes and centers of gravity are shown in the figure.

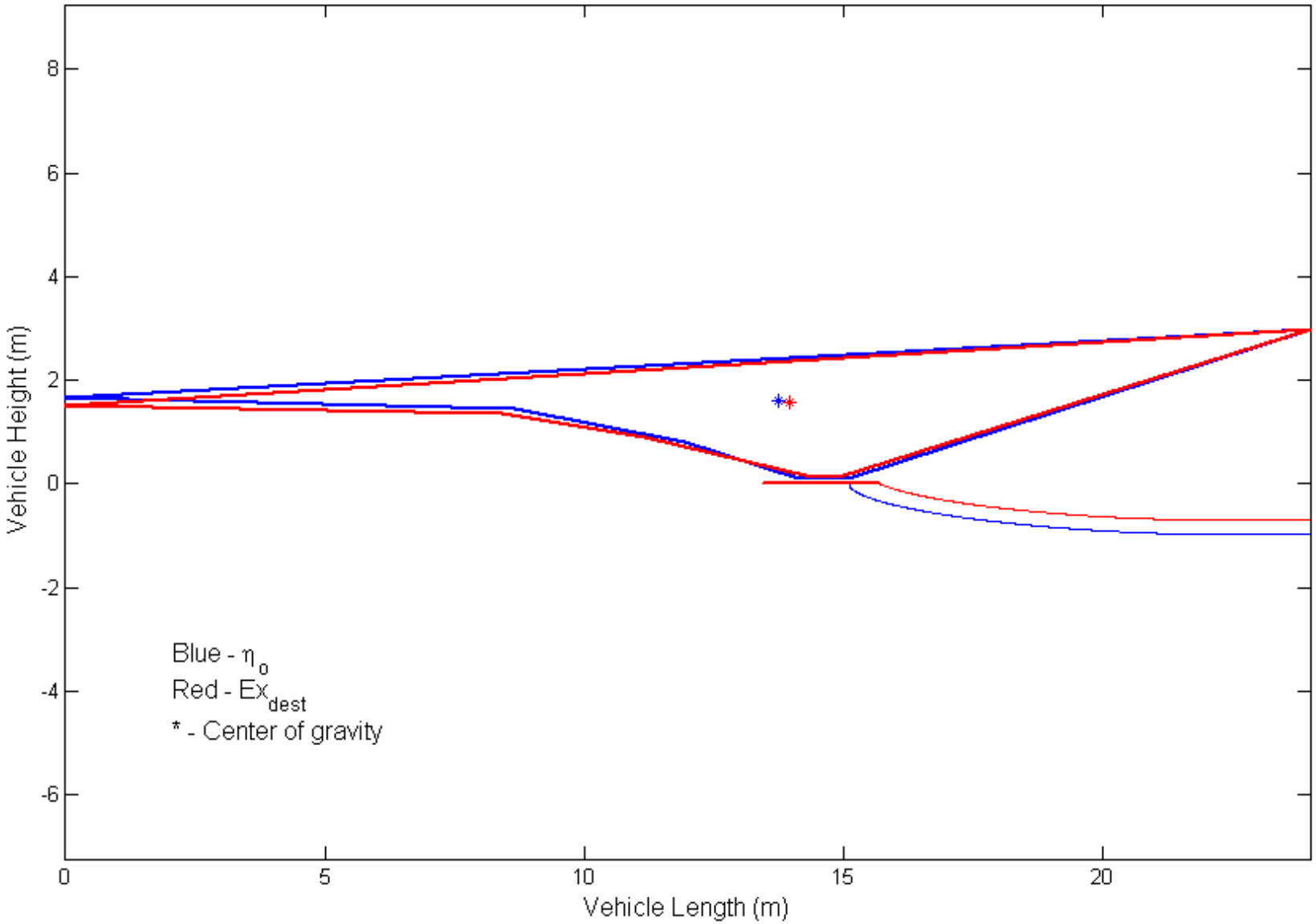

Figure B-2. Optimal Mach 8-10 accelerator vehicles for the single segment optimizations using the objective functions η_o and Ex_{dest}. Both vehicle plumes and centers of gravity are shown in the figure.

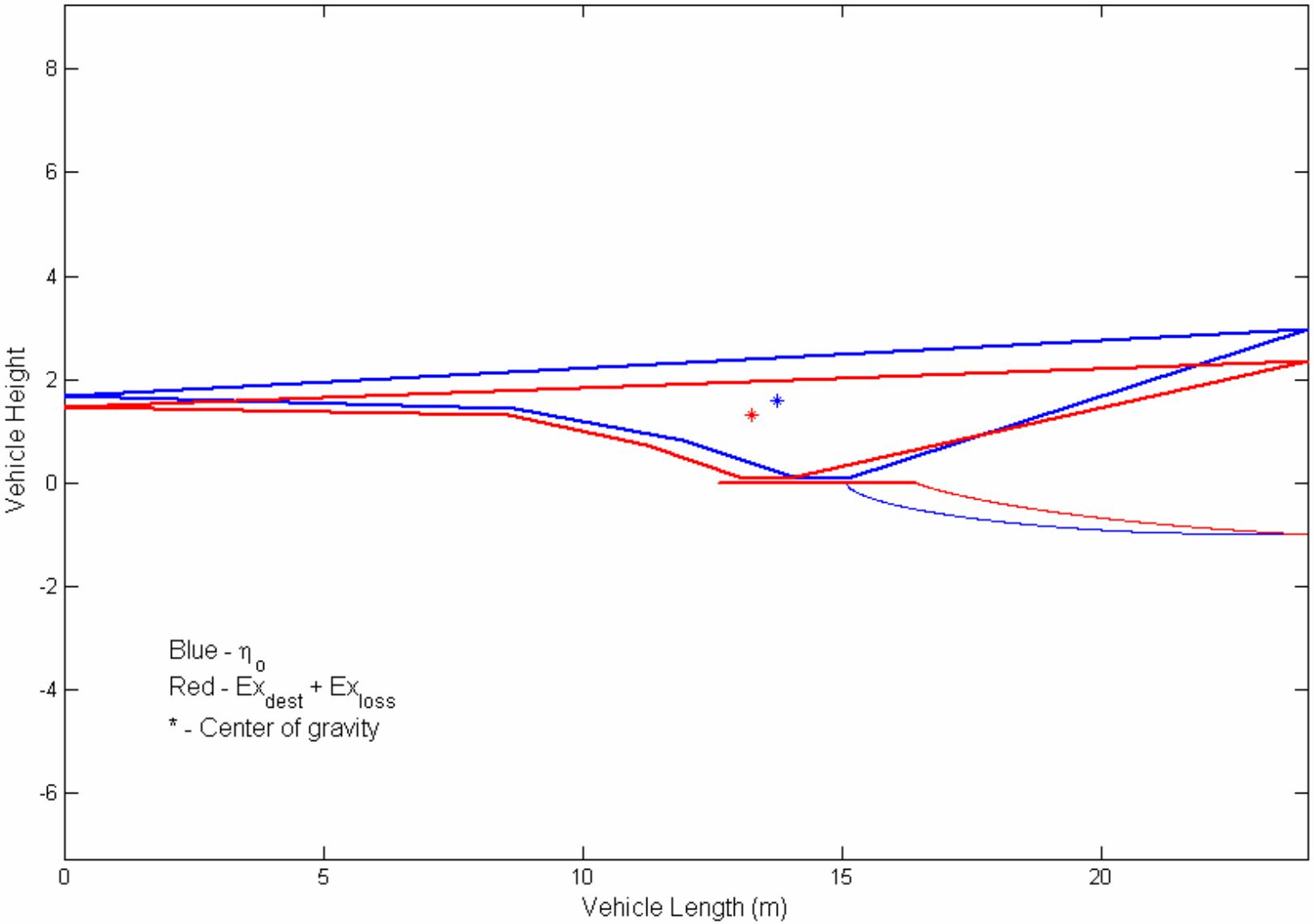

Figure B-3. Optimal Mach 8-10 accelerator vehicles for the single segment optimizations using the objective functions η_o and $Ex_{dest} + Ex_{loss}$. Both vehicle plumes and centers of gravity are shown in the figure.

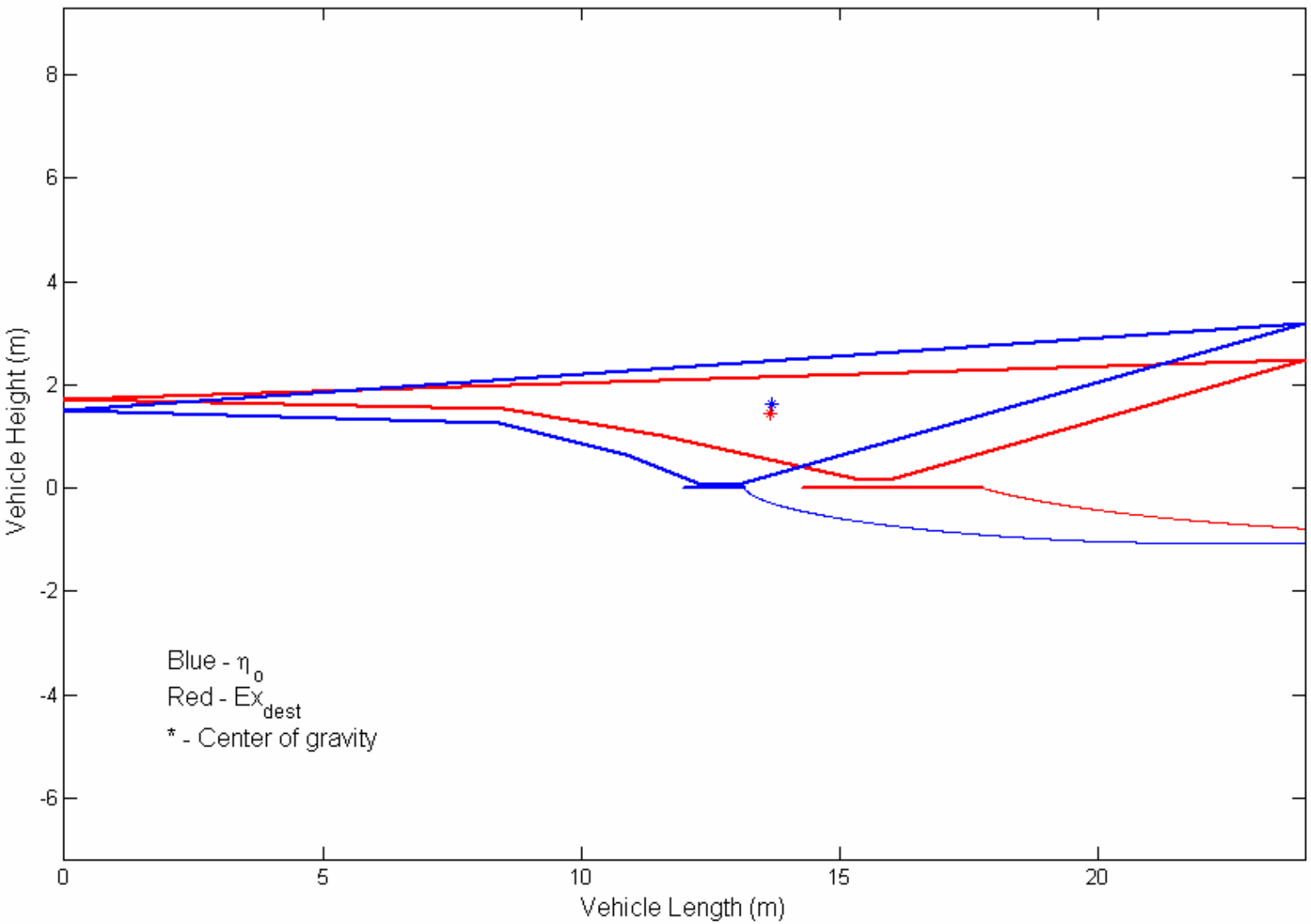

Figure B-4. Optimal Mach 10 cruise vehicles for the single segment optimization using the objective functions η_o and Ex_{dest}. Both vehicle plumes and centers of gravity are shown in the figure.

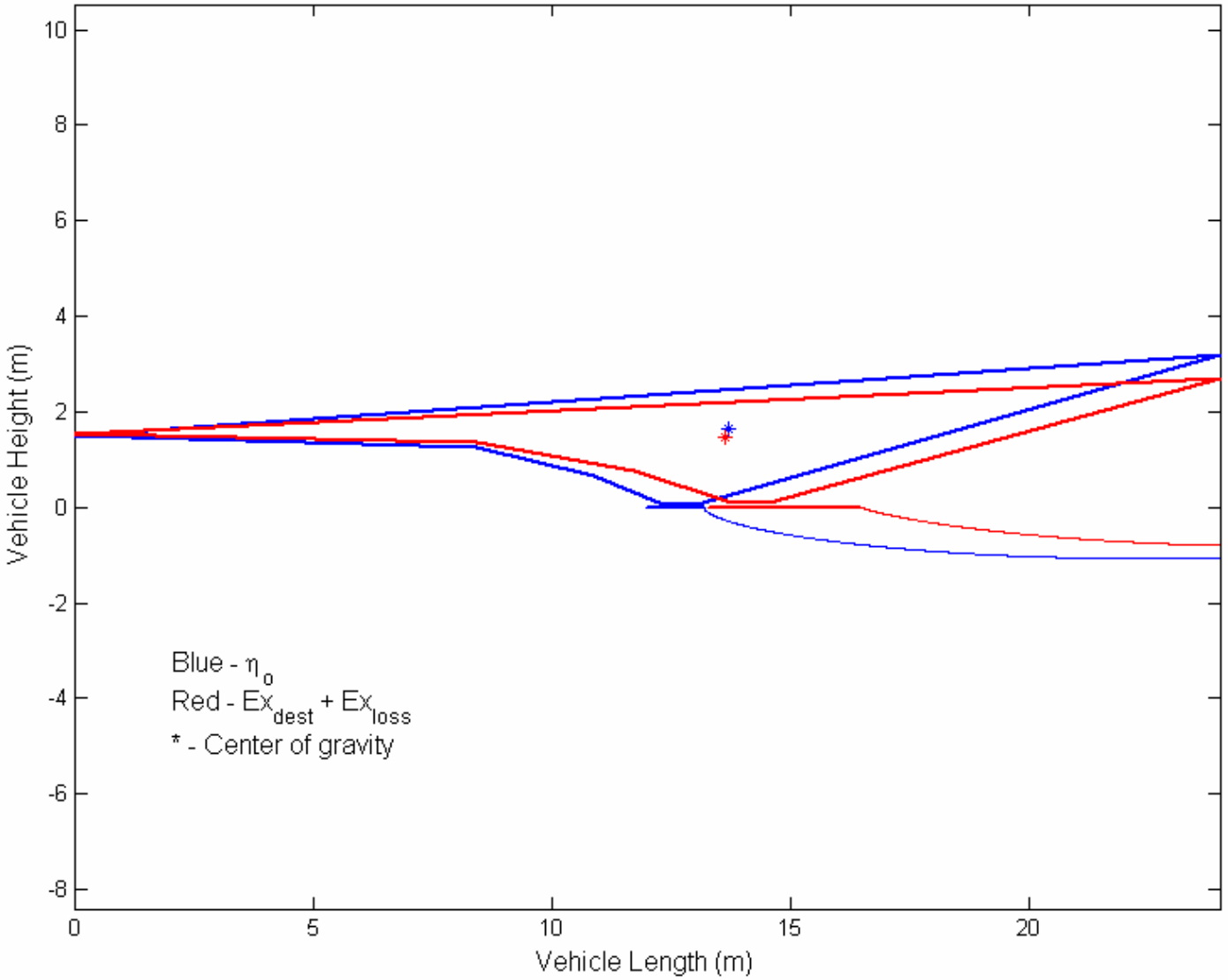

Figure B-5. Optimal Mach 10 cruise vehicles for the single segment optimization using the objective functions η_o and $Ex_{dest} + Ex_{loss}$. Both vehicle plumes and centers of gravity are shown in the figure.

Appendix C

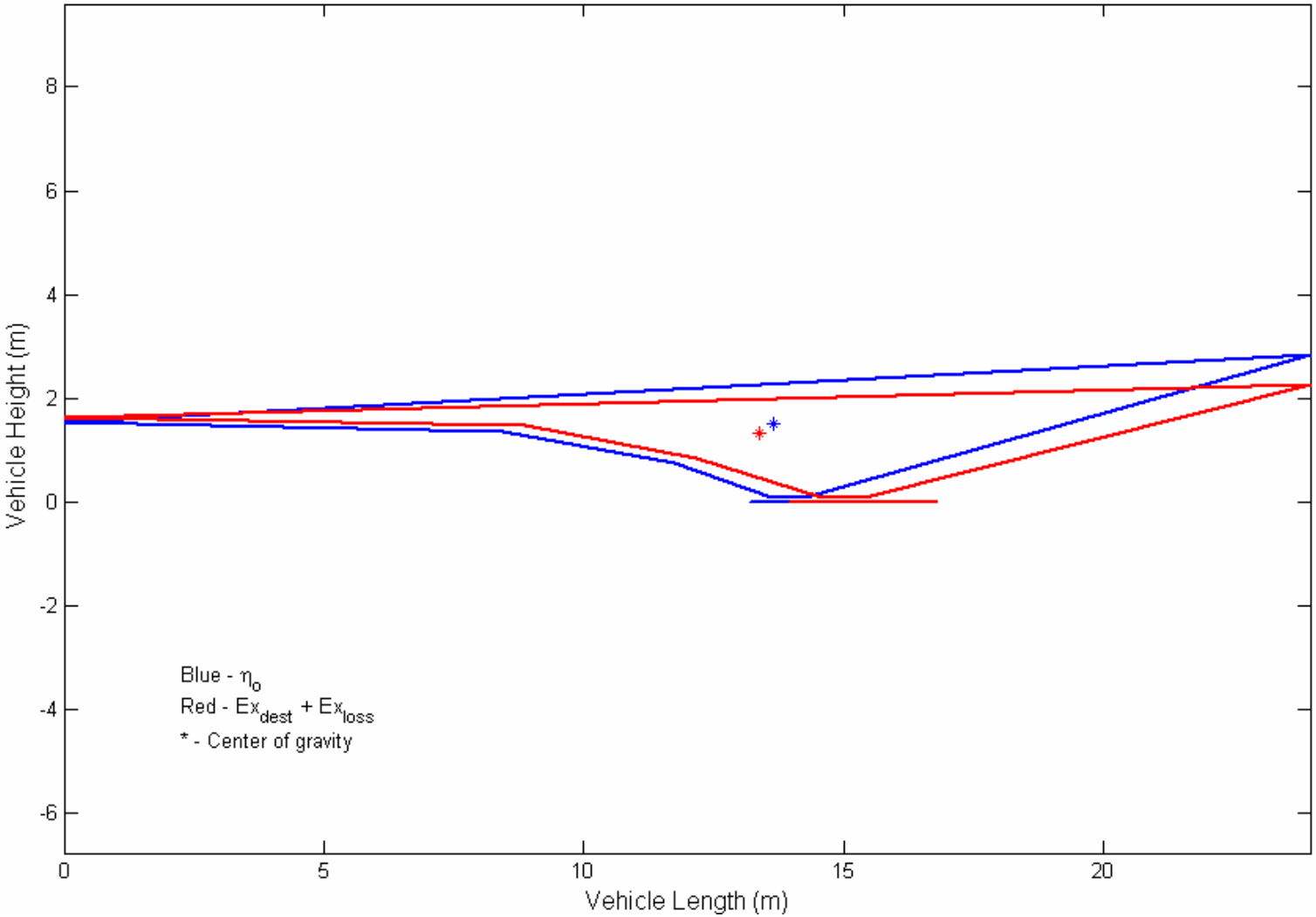

Figure C-1. Optimal partial mission vehicles for objective functions η_o and $Ex_{dest} + Ex_{loss}$.

References

[1] Heiser, W. H., and Pratt, D. T., *Hypersonic Airbreathing Propulsion*, AIAA, Inc., Washington, D.C., 1994.

[2] Anderson Jr., J. D., *Hypersonic and High Temperature Gas Dynamics*, AIAA, Inc., Reston, VA, 1989.

[3] Anderson Jr., J. D., *Fundamentals of Aerodynamics*, 3rd Edition, McGraw-Hill, New York, 2001.

[4] Moorhouse, D. J., "Proposed System-Level Multidisciplinary Analysis Technique Based on Exergy Methods", *Journal of Aircraft*, Vol. 40, No. 1, January-February 2003.

[5] Moorhouse, D. J., and Suchomel, C. F., "Exergy Methods Applied to the Hypersonic Vehicle Challenge", AIAA Paper No. 2001-3063, 2001.

[6] Moorhouse, D. J., Hoke, C. M., and Prendergast, J. P., "Thermal Analysis of Hypersonic Inlet Flow with Exergy-Based Design Methods", *International Journal of Applied Thermodynamics*, Vol. 5, No. 4, December 2002.

[7] Camberos, J. A., and Moorhouse, D. J., "Modeling Aerospace Vehicle Systems Based on Minimum Exergy Destruction", First International Conference on Grand Challenges for Modeling and Simulation, draft version.

[8] Camberos, J. A., "Quantifying Irreversible Losses for Magnetohydrodynamic (MHD) Flow Simulation", AIAA Paper 2003-3647, 2003.

[9] Riggins, D. W., "High-Speed Engine/Component Performance Assessment Using Exergy and Thrust-Based Methods", NASA Contractor Report 198271, 1996.

[10] Riggins, D. W., McClinton, C. R., and Vitt, P. H., "Thrust Losses in Hypersonic Engines Part 1: Methodology", *Journal of Propulsion and Power*, Vol. 13, No. 2, March-April 1997.

[11] Riggins, D. W., "Thrust Losses in Hypersonic Engines Part 2: Applications", *Journal of Propulsion and Power*, Vol. 13, No. 2, March-April 1997.

[12] Riggins, D. W., "Evaluation of Performance Loss Methods for High-Speed Engine and Engine Components", *Journal of Propulsion and Power*, Vol. 13, No. 2, March-April 1997.

[13] Riggins, D. W., Taylor, T., and Homan, K., "The Detailed Auditing and Optimization of High Speed Vehicle Performance in Terms of Irreversibility and Heat", Summer Research Presentation at Air Force Research Laboratories, July 2004.

[14] Roth, B. A., "A Work Potential Perspective of Engine Component Performance", AIAA Paper 2001-3300, 2001.

[15] Roth, B. A., and Mavris, D. N., "Generalized Model for Vehicle Thermodynamic Loss Management", *Journal of Aircraft*, Vol. 40, No. 1, January-February 2003.

[16] Figliola, R. S, Tipton, R., and Li, H., "Exergy Approach to Decision-Based Design of Integrated Aircraft Thermal Systems", *Journal of Aircraft*, Vol. 40, No. 1, January-February 2003.

[17] Figliola, R. S., Stewart, J., Nomura, S., and Camberos, J. A., "An Exergy Based Methodology for Aircraft Systems Integration: Wing Aerodynamics Assessment", Summer Research Presentation at Air Force Research Laboratories, July 2004.

[18] Paulus Jr., D. M., and Gaggioli, R. A., "Rational Objective Functions for Vehicles", AIAA Paper No. 2000-4852.

[19] Bejan, A., "Architecture From Exergy-Based Global Optimizaiton: Tree-Shaped Flows and Energy Systems for Aircraft", AIAA Paper No. 2000-4855, 2000.

[20] Bejan, A., "Constructal Theory: Tree-Shaped Flows and Energy Systems for Aircraft", *Journal of Aircraft*, Vol. 40, No. 1, January-February 2003.

[21] Curran, E. T., and Murthy, S. N. B., *Scramjet Propulsion*, Progress in Astronautics and Aeronautics, Vol. 189, AIAA, Inc., Reston, VA, 2000.

[22] Curran, E. T., and Craig, R. R., "The Use of Stream Thrust Concepts for the Approximate Evaluation of Hypersonic Ramjet Engine Performance", Air Force Aero-Propulsion Laboratory, Tehcnical Report AFAPL-TR-73-38, July 1973.

[23] Czysz, P., and Murthy, S. N. B., "Energy Analysis of High-Speed Flight Systems", *High Speed Flight Propulsion Systems*, edited by S. N. B. Murthy and E. T. Curran, Progress in Astronautics and Aeronautics, Vol. 137, AIAA, Inc., Reston, VA, 1991.

[24] Gyftopoulos, E. P., and Beretta, G. P., *Thermodynamics: Foundations and Applications*, Macmillan Publishing Co., New York, 1991.

[25] Moran, M. J., *Availability Analysis: a Guide to Efficient Energy Use*, ASME Press, New York, New York, 1989.

[26] Rancruel, D., 2002, *Decomposition Strategy Based on Thermoeconomic Isolation Applied to the Optimal Synthesis/Design and Operation of an Advanced Figther Aircraft System*, Department of Mechanical Engineering, Virginia Polytechnic Institute and State University, M.S. Thesis.

[27] Rancruel, D. F., and von Spakovsky, M. R., "Use of a Unique Decomposition Strategy for the Optimal Synthesis/Design and Operation of an Advanced Fighter Aircraft System", 10th AIAA/ISSMO Multi-disciplinary Analysis and Optimization Conference, Albany, New York, 2004.

[28] Rancruel, D. F. and von Spakovsky, M. R., "Decomposition with Thermoeconomic Isolation Applied to the Optimal Synthesis/Design of an Advanced Fighter Aircraft System, *International Journal of Thermodynamics*, Vol. 6, No. 3, September 2003.

[29] Rancruel, D. F., and von Spakovsky, M. R., "A Decomposition Strategy Applied to the Optimal Synthesis/Design and Operation of an Advanced Fighter Aircraft System: A Comparison with and without Airframe Degrees of Freedom", International Mechanical Engineering Congress and Exposition, New York, New York, 2003.

[30] von Spakovsky, M. R., and Evans, R. B., "Engineering Functional Analysis (Part 1)", *Journal of Energy Resources Technology*, Vol. 115, No. 2, June 1993.

[31] Munoz, J. R., and von Spakovsky, M. R., "The Application of Decomposition to the Large Scale Synthesis/Design Optimization of Aircraft Energy Systems", *International Journal of Applied Thermodynamics*, Vol. 4, No. 2, June 2001.

[32] Munoz, J. R., and von Spakovsky, M. R., "A Decomposition Approach for the Large Scale Synthesis/Design Optimization of Highly Coupled, Highly Dynamic Energy Systems", *International Journal of Applied Thermodynamics,* Vol. 4, No.1, March 2001.

[33] Munoz, J. R., and von Spakovksy, M. R., "Decomposition in Energy System Synthesis/Designs Optimization for Stationary and Aerospace Applications", *AIAA Journal of Aircraft*, Vol. 39, No. 6, 2003.

[34] Mattingly, J. D., Heiser, W. H., and Daley, D. H., *Aircraft Engine Design*, AIAA, Inc., Washington, D.C., 1987.

[35] Raymer, D. P., *Aircraft Design: A Conceptual Approach*, 3rd Edition, AIAA, Inc., Reston, VA, 1999.

[36] Bowcutt, K., "Hypersonic Aircraft Optimization Including Aerodynamic, Propulsion, and Trim Effects", AIAA Paper No. 92-5055, 1992.

[37] Nelder, J. A., and Mead, R., "A Simplex Method for Function Minimization", *Computer Journal*, Vol. 7, January 1965.

[38] Bowcutt, K., "Multidisciplinary Optimization of Airbreathing Hypersonic Vehicles", *Journal of Propulsion and Power*, Vol. 17, No. 6, November-December 2001.

[39] Gentry, A. E., Smyth, D. N., and Oliver, W. R., "The Mark IV Supersonic-Hypersonic Arbitrary-Body Program", AFFDL-TR-73-159, Vols. 1, 2, and 3, November 1973.

[40] Reddecliff, J. M., and Weber, J. W., "Development and Demonstration of a Hydrocarbon Scramjet Propulsion System", AIAA Paper No. 98-1613, 1998.

[41] O'Neil, M. K., and Lewis, M. J., "Design Tradeoffs on Scramjet Engine Integrated Hypersonic Waverider Vehicles", *Journal of Aircraft*, Vol. 30, No. 6, November-December 1993.

[42] Takashima, N., and Lewis, M. J., "Optimization of Waverider-Based Hypersonic Cruise Vehicles with Off-Design Considerations", *Journal of Aircraft*, Vol. 36, No. 1, January-February 1999.

[43] Shapiro, A. H., *The Dynamics and Thermodynamics of Compressible Fluid Flow*, *Volume 1*, The Ronald Press Company, New York, 1953.

[44] Baker, M. L., Munson, M. J., Duchow, E., Hoppus, G. W., and Alston, K. Y., "System Level Optimization in the Integrated Hypersonic Aeromechanics Tool (IHAT)", AIAA Paper No. 2004-618, 2004.

[45] Roth, B. A., 2000, *A Theoretical Treatment of Technical Risk Management in Modern Propulsion System Design*, Department of Aerospace Engineering, Georgia Institute of Technology, Ph.D. Dissertation.

[46] Ravichandran, M., and Murthy, S. N. B., "Generalized One-Dimensional Available Energy Analysis of Scram Combustor", AIAA Paper 96-3138, 1996.

[47] Brilliant, H. M., "Analysis of Scramjet Engines Using Exergy Methods", AIAA Paper 95-2767, 1995.

[48] John, J. E. A., *Gas Dynamics*, 2nd Edition, Prentice Hall, Upper Saddle River, NJ, 1984.

[49] Lehrach, R.P.C., "Thrust/Drag Accounting for Aerospace Plane Vehicles", AIAA Paper No. 87-1966, 1987.

[50] Numbers, K., "Hypersonic Propulsion System Force Accounting", AIAA Paper No. 91-0228, 1991.

[51] Perkins Jr., S. C., and Dillenius, M. F. E., "Estimation of Additive Forces and Moments for Supersonic Inlets", AIAA Paper No. 91-0712, 1991.

[52] Sullins, G. A., and Billig, F. S., "Force Accounting for Airframe Integrated Engines", AIAA Paper No. 87-1965, 1987.

[53] Macheret, S. O., Shneider, M. N., and Miles, R. B., "Scramjet Inlet Control by Off-Body Energy Addition: a Virtual Cowl", AIAA 2003-32, 2003.

[54] Huber, P. W., Schexnayder Jr., C. J., and McClinton, C. R., "Criteria for Self-Ignition of Supersonic Hydrogen-Air Mixtures", NASA Technical Paper 1457, 1979.

[55] Jachimowski, C. J., "An Analytical Study of the Hydrogen-Air Reaction Mechanism with Application to Scramjet Combustion", NASA Technical Paper 2791, 1988.

[56] Riggins, D. W., and McClinton, C. R., "Analysis of Losses in Supersonic Mixing and Reacting Flows", AIAA Paper No. 91-2266, 1991.

[57] Riggins, D. W., McClinton, C. R., Rogers, R. C., and Bittner, R. D., "A Comparative Study of Scramjet Injection Strategies for High Mach Number Flows", AIAA Paper No. 92-3287, 1992.

[58] Riggins, D. W., Private Communication, July 2003 - July 2004.

[59] Small, W. J., Weidner, J. P., and Johnston, P. J., "Scramjet Nozzle Design and Analysis as Applied to a Highly Integrated Hypersonic Research Airplane", NASA Technical Note D-8334, November 1976.

[60] Stalker, R. J., and Morgan, R. G., "Supersonic Hydrogen Combustion with a Short Thrust Nozzle", *Combustion and Flame,* Vol. 57, Issue 1, July 1984.

[61] Pulsonetti, M. V., Erdos, J., and Early, K., "An Engineering Model for Analysis of Scramjet Combustor Performance with Finite Rate Chemistry", AIAA Paper No. 88-3258, 1998.

[62] Brewer, K. M., 2005, *Exergy Methods for Mission-Level Analysis and Optimization of Generic Hypersonic Vehicle Concepts*, Department of Mechanical Engineering, Virginia Polytechnic Institute and State University, M.S. Thesis.

[63] Chavez, F. R., and Schmidt, D. K., "Generic Hypersonic Vehicle Performance Model", Interim Task Report, NASA-CR-192953, April 1993.

[64] Pytel, A., and Kiusalaas, J., *Engineering Mechanics: Statics and Dynamics*, HaperCollins College Publishers, New York, 1994.

[65] Bejan, A., *Entropy Generation Minimization: The Method of Thermodynamic Optimization of Finite-Sized Systems and Finite-Time Processes*, CRC Press, Inc., Boca Raton, FL, 1996.

[66] Jernell, L. S., "Comparison of Two-Dimensional Shock-Expansion Theory with Experimental Aerodynamic Data for Delta-Planform Wings at High Supersonic Speeds"NASA Technical Note D-7583, June 1974.

[67] Wood, R. M., and Miller, D. S., "Impact of Airfoil Profile on the Supersonic Aerodynamics of Delta Wings", *Journal of Aircraft*, Vol. 23, No. 9, September 1986.

[68] Moorhouse, D. J., Private Communication, June 2003-August 2004

[69] Leyland, G. B., 2002, *Multi-Objective Optimisation Applied to Industrial Energy Problems*, Department of Mechanical Engineering, University of Auckland, M.S. Thesis.

[70] Periannan, V., 2005, *Investigation of the Effects of Different Objective Functions/Figures of Merit on the Analysis and Optimization of High Performance Aircraft System Synthesis/Design*, Department of Mechanical Engineering, Virginia Polytechnic Institute and State University, M.S. Thesis.

Vita

Kyle Charles Markell was born in Palmerton, Pennsylvania on July 12, 1979. He attended high school at Lehighton Area High School about 20 miles north of Allentown, PA. After his glorious high school days, he ventured on to State College, PA in June of 1997 where he attended The Pennsylvania State University (GO LIONS!!). Four and a half years and multiple miserable football seasons later, he graduated with a Bachelor of Science degree in Mechanical Engineering. He began his graduate studies at Virginia Tech University in January of 2003 where he quickly realized that Blacksburg wasn't as warm in the winter as he anticipated. While at Virginia Tech he had the opportunity to work at the Air Force Research Laboratory at Wright Patterson Air Force Base in Dayton, OH for two summers. Upon completion of his Master of Science in Mechanical Engineering he will be working in the Mechanical, Electrical and Reactor Activity, Surface Ship Power Plant Section at Bechtel Bettis, Inc. in Pittsburgh, PA.